Università degli studi di Padova

FACOLTÀ DI SCIENZE MATEMATICHE, FISICHE E NATURALI
Corso di Laurea Specialistica in Fisica

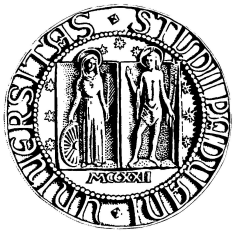

Z^0Z^0 production cross section measurement in the four lepton decay channel at CDF experiment

Relatore:
Dott. Donatella Lucchesi

Correlatore:
Dott. Simone Pagan Griso

Laureando:
Matteo Bauce
584711-SF

Anno Accademico 2008 - 2009

Yesterday is history,
Tomorrow is a mystery,
but Today is a gift:
that is why it is called the Present.

Abstract

This thesis describes the measurement of Z^0Z^0 production cross section in $p\bar{p}$ collisions at the CDF (Compact Detector at Fermilab) experiment at Tevatron. The determination of this quantity is important to test Standard Model predictions of Electro-Weak couplings. Moreover the Z^0Z^0 reconstruction is an important step for the Higgs boson searches in the high mass region. The cross section measurement has been done in the four massive lepton decay channel that has a small branching ratio but it is characterized by a very low background contribution. The search for $Z^0Z^0 \to lll'l'$ (l=e, μ) has been performed using 4.8 fb^{-1} of data collected by CDF using lepton triggers. The number of expected signal events is 4.68 $\pm$ 0.78 while the background contributes with 0.041 $\pm$ 0.033 events. We observe 5 events, that corresponds to a significance of 5.70 σ. This is the first observation of a Z^0Z^0 signal at CDF. With these events we measure a cross section of $1.56^{+0.80}_{-0.63}$(stat.) $\pm$ 0.25(syst.) pb, in agreement with Standard Model value 1.4 $\pm$ 0.1 pb at Next to Leading Order.

Contents

Introduction

The physical processes involving two gauge bosons are strictly connected with important observables of the electroweak theory and the measurements of their properties are a fundamental check of Standard Model predictions. Diboson physics is also an important starting point for the search of new physics beyond the Standard Model, like anomalous Trilinear Gauge Couplings and the search for the Higgs boson in the high mass region where it is expected to decay to ZZ with a significant branching fraction. The analysis presented in this thesis describes the measurement of the production cross section of ZZ diboson in $p\bar{p}$ collision at $\sqrt{s}$= 1.96 TeV at CDF experiment, using 4.8 fb^{-1} of data. The ZZ production cross section has been measured in e^+e^- collision at LEP collider and by CDF and $D\emptyset$ experiments in $p\bar{p}$ collisions. CDF did not have a signal with 5σ significance. This analysis focuses on the $ZZ \to lll'l'$ decay channel. The branching ratio for this decay channel is low (less than 1%) but is characterized by a very small background that allows a measurement with a good significance regardless the small statistics. The analysis is based on lepton identification, on which CDF has reached a good level: new lepton reconstruction techniques have been introduced in this analysis to improve the previous result and increase the overall acceptance. With the analysis techniques used we were able to isolate a Z^0Z^0 sample with more than 5σ significance.

The result has been approved by the CDF Collaboration providing the

first CDF observation of Z^0Z^0 production

and it is now public as a CDF result[1].

In Chapter 1 is reported a brief overview of the theory of particle interactions and properties, theoretical basis for the analysis described in this work. In Chapter 2 there is a summary of the actual knowledge on boson and diboson physics, the most relevant results obtained by the previous experiments and future perspective on this domain. Chapter 3 describes the Tevatron accelerator at the Fermi National Accelerator Laboratory and the CDF detector used for this measurement. In Chapter 4 are described the techniques used to reconstruct different physical *objects*, with a particular attention in the last part of the chapter, to the lepton reconstruction, essential component of this work. Chapter 5 describes the analysis techniques developed in this work to select the signal sample used to measure the final cross section. In Chapter 6 there is a detailed description of the method used to estimated the background contribution. In Chapter 7 are shown the results obtained and the statistical procedure used to reach it. With this analysis we obtained a ZZ production cross section measurement with a significance of 5.7 σ and all the kinematical checks bear out the results reached.

Chapter 1

The Standard Model

Contents

The Standard Model (SM) of particles physics is a gauge field theory which incorporates both quantum mechanics and Einstein's theory of special relativity in the attempt to describe the fundamental particles and their interactions. The Standard Model describes three of the four known fundamental forces of nature: strong interactions, electromagnetic interactions and weak interactions. The fourth force, the gravity, is far weaker[1] and is not expected to contribute significantly to the physical processes which are of current interest in high energy particle physics.
The Standard Model is described by the gauge group

$$SU(3)_C \times SU(2)_L \times U(1)_Y \tag{1.1}$$

and is invariant under local gauge transformation. The C is a reminder that $SU(3)$ represents the symmetry group of the *coloured* strong interactions of quantum chromodynamics (QCD). The L indicates that the $SU(2)$ group contains left-handed weak isospin doublets and the Y is a reminder that the $U(1)$ group contains the right-handed weak hypercharge singlets. Together, the $SU(2)_L \times U(1)_Y$ groups govern the unified electroweak force.
There are two main classification of particles within the SM: the spin-$\frac{1}{2}$ *fermions* that are the constituents of normal matter and the integer spin *bosons* which are also the mediators of the strong and electroweak forces. Particles in SM are produced massless; the most accredited theory to give them mass is based on the interaction with the so-called Higgs field which is a result of a spontaneously broken symmetry arising in the $SU(2)_L \times U(1)_Y$ electroweak sector. The predicted Higgs boson resulting from this broken symmetry is the only particle in the SM which has yet to be experimentally verified. This chapter describes the fundamental particles and their interactions and a short overview of the Higgs mechanism.

[1] Roughly 40 orders of magnitude smaller than the strong nuclear force.

1.1 Fundamental Particles

1.1.1 Fermions

Fermions are spin-$\frac{1}{2}$ fundamental particles that appear as two different types: quarks and leptons. Quarks are the constituents of familiar composite particles such as the proton and neutron, but they can combine to form other hadrons which are bound state of 2 or 3 quarks called mesons and baryons respectively. Quarks interact via both strong and electroweak forces. Leptons, such as the electron, on the other hand have only electroweak interactions.

Quarks

There are six types of quarks plus their anti-quarks: up, down, charm, strange, top and bottom. Quarks have fractional electric charge (Q) and a quantum property called *colour charge* similar to the electric charge of electromagnetism, but in three flavours r, g and b. The charges (Q) and the masses of the quarks are listed in Table 1.1 along with their *quark*-ness quantum number.

	Flavour	Charge (Q)	Quantum Numbers	Mass (GeV)
1st generation	u	$+2/3$	U=+1	(1.5 - 3.3) $\times 10^{-3}$
	d	-1/3	D=-1	(3.5 - 6.0) $\times 10^{-3}$
2nd generation	c	$+2/3$	C=+1	$1.27^{+0.07}_{-0.11}$
	s	-1/3	S=-1	$104^{+26}_{-34} \times 10^{-3}$
3rd generation	t	$+2/3$	T=+1	171.2 $\pm$ 2.1
	b	-1/3	B=-1	$4.2^{+0.17}_{-0.07}$

Table 1.1: Charge, *quark*-ness and mass [2] of the quarks.

Quarks are subject to both strong interactions as well as electroweak interactions which are discussed in section 1.2 and 1.3 respectively.

Leptons

There are six types of leptons (plus their anti-particles) in the SM. These are the electron, muon, tau (e, μ, τ) and their respective neutrinos (ν_e, ν_μ, ν_τ). They are classified by their charge and lepton quantum numbers (L_e, L_μ and L_τ) as shown in Table 1.2.

Leptons are subject to the electroweak force. They are colourless and thus do not participate in strong interactions.
Although the neutrino masses are listed in Table 1.2 only with an upper limit, there is now strong evidence from neutrino mixing measurements that they are in fact non-zero [3]. Also, it is worth to note that the τ lepton is the only lepton with enough mass to decay hadronically, and it does it with a branching fraction of 65% [2].

1.1.2 Bosons - Force Mediators

SM interactions are mediated by spin-1 bosons. The gluons (g) is the mass-less mediator of the strong force. The photon (γ), $W^\pm$ and Z are the force carriers of the electroweak interactions.

Flavour	Charge (Q)	Lepton Numbers	Mass (GeV)
e	-1	$L_e = 1$	0.511 $\times 10^{-3}$
ν_e	0	$L_e = 1$	$< 225 \times 10^{-9}$
μ	-1	$L_\mu = 1$	105.7 $\times 10^{-3}$
ν_μ	0	$L_\mu = 1$	$< 0.19 \times 10^{-3}$
τ	-1	$L_\tau = 1$	1.777
ν_τ	0	$L_\tau = 1$	$< 18.2 \times 10^{-3}$

Table 1.2: Charge, lepton number and mass [2] for the leptons.

The photon is mass-less while the $W^\pm$ and Z are massive particles. The gauge bosons and their properties are summarized in Table 1.3. The role of force carriers in particle interactions is described in Sections 1.2 and 1.3. Since this thesis focuses on the study of dibosons production, more details about the gauge massive bosons will be given in Chapter 2.

	Interactions	Charge	Mass [GeV/c^2]	Width [GeV/c^2]
g	strong	0	0	
γ	electromagnetic	0	0	
Z	weak	0	91.1876 $\pm$ 0.0021	2.4952 $\pm$ 0.0023
$W^\pm$	weak	± 1	80.398 $\pm$ 0.025	2.141 $\pm$ 0.041

Table 1.3: Summary of the force carriers and their masses [2]

1.2 Quantum Chromodynamics

Quantum chromodynamics (QCD) is the theory of the strong interactions between quarks and gluons. Quarks carry a single colour charge while a gluon is bicoloured and is the mediator of color flow. In $SU(3)$ the three colours give nine total colour states for the gluon: an octet and a colour singlet. However, the singlet is colourless and so in nature there are only 8 possible coloured gluons. Quarks only exist in colourless bound states with integer charge. For instance the proton is the combination of three quarks uud perhaps having the colours rgb (among other possibilities) respectively. The color sum give a colorless bound state with a net charge of $+1$. Quark-antiquark combinations are possible, for example, the pion π^+ which is a $u\overline{d}$ bound state whose quarks have the color combination possibilities $r\overline{r}$ or $b\overline{b}$.
The feature of the strong force is that the coupling becomes increasingly large with separation distance. This indicates that coloured partons will be confined in objects which are as a whole colorless. The coupling constant of QCD (α_s) is a running function of the momentum transferred in the interaction, q^μ, which is given by the equation

$$\alpha_s(q^2) = \frac{12\pi}{(33 - 2n_f)\log(q^2/\Lambda^2)}. \tag{1.2}$$

Here $\Lambda \sim 0.1$ GeV indicates the upper energy limit at which SM should be considered valid (as approximation of more extended theories) and n_f is the number of quark flavours whose mass is

greater than the q^2 of interest [4]. At very large q^2 (corresponding to very short approach distances) α_s becomes increasingly small. This phenomena is known as asymptotic freedom. This property allows, for high-q^2 interaction, perturbative expansion of QCD processes which remain finite.
Gluons couple to quarks and other gluons via the qqg,ggg and $gggg$ vertices shown in Figure 1.1. Colour, charge and quark-ness are always conserved in strong interactions.

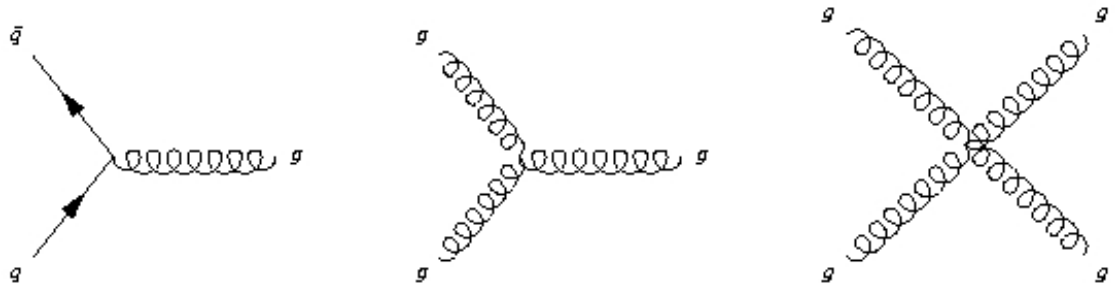

Figure 1.1: The primary vertices of QCD.

A more detailed description of QCD theory can be found in [5; 6]

1.3 Electroweak interactions

The electroweak interaction of quarks and leptons is described by the $SU(2)_L \times U(1)_Y$ gauge group. Weak isospin (T_L) and hypercharge (Y) are the respective generators of symmetry transformations. They satisfy the equation

$$Q = T_3 + \frac{1}{2}Y \tag{1.3}$$

where T_3 is the projection of the third component of the weak isospin vector.
The electroweak Lagrangian is given by

$$\mathcal{L} = -\frac{1}{4}W^{\mu\nu}W_{\mu\nu} - B^{\mu\nu}B_{\mu\nu} + \overline{\psi}i\gamma^{\mu}D_{\mu}\psi \tag{1.4}$$

where the covariant derivative is given by

$$D_{\mu} = \partial_{\mu} + igW_{\mu}T + \frac{1}{2}ig'B_{\mu}Y. \tag{1.5}$$

T is the weak isospin operator, g and g' are two different electroweak coupling constants and $B_{\mu\nu}$, similar to the electromagnetic field tensor, is given by

$$B_{\mu\nu} = \partial_{\mu}B_{\nu} - \partial_{\nu}B_{\mu} \tag{1.6}$$

where B_{ν} is the massless gauge field representing the singlet of $U(1)_Y$. W_{μ} are the gauge fields of $SU(2)$ and $W_{\mu\nu}$ the field tensor which is defined as

$$W_{\mu\nu} = \partial_{\mu}W_{\nu} - \partial_{\nu}W_{\mu} - gW_{\mu} \times W_{\nu} \tag{1.7}$$

The electroweak gauge fields W_μ^1, W_μ^2, W_μ^2 and B_μ used to write the electroweak lagrangian have basically a theoretical meaning. Instead, in particle physics we can express $\mathcal{L}$ as function of four physical fields: A_μ, Z_μ, W_μ^+ and W_μ^-. A_μ is the (neutral) electromagnetic field, Z_μ is the field corresponding to electroweak neutral current while $W_\mu^\pm$ correspond to the electroweak charged currents. By requiring the electromagnetic and weak forces to be unified and to describe the gauge bosons observed experimentally it is required that there be two neutral and two charged bosons. Thus the electromagnetic field A and neutral current Z must be some linear combination of the unified electroweak fields. This can be written in terms of the electroweak mixing angle θ_W as

$$\begin{pmatrix} Z \\ A \end{pmatrix} = \begin{pmatrix} \cos\theta_W & -\sin\theta_W \\ \sin\theta_W & \cos\theta_W \end{pmatrix} \cdot \begin{pmatrix} W^3 \\ B \end{pmatrix} \tag{1.8}$$

from which can be shown that the parameters g and g' have the relation $g' = g\tan\theta_W$ and are also related to the charge of the electron e by the relation $e = g\sin\theta_W = g'\cos\theta_W$. The remaining two components of the W_μ are then related to the observables W^+ and W^-. The real fields are then given by

$$W^\pm = \frac{1}{\sqrt{2}}(W_\mu^1 \mp iW_\mu^2) \tag{1.9}$$

$$Z_\mu = \frac{-g'B_\mu + gW_\mu^3}{\sqrt{g^2+g'^2}} \tag{1.10}$$

$$A_\mu = \frac{gB_\mu + g'W_\mu^3}{\sqrt{g^2+g'^2}}. \tag{1.11}$$

The term in the electroweak Lagrangian given in Eq. 1.4 responsible for the interaction of quarks and leptons with the gauge bosons is $\overline{\psi}i\gamma^\mu D_\mu\psi$ which can be rewritten as

$$eJ_{EM}^\mu A_\mu + \frac{g}{\sqrt{2}}(J_L^{+\mu}W_L^+ + J_L^{-\mu}W_L^-) + \frac{gg'}{e}J_Z^\mu Z_\mu \tag{1.12}$$

where

$$J_L^{\pm\mu} = \sqrt{2}\overline{\psi}\gamma^\mu T_L^\pm\psi \tag{1.13}$$

$$J_Z^\mu = \overline{\psi}\gamma^\mu(T_{3L} - \sin^2\theta_W Q)\psi \tag{1.14}$$

$$J_{EM}^\mu = \overline{\psi}\gamma^\mu Q\psi \tag{1.15}$$

which are the charged and neutral current interaction terms describing the interaction of the gauge bosons with the fermion ψ fields.
Singlet state ψ_R do not survive operations by T and T_{3L}. Since neutrinos do not carry charge it can be seen that there are no right-handed neutrino state ν_R.
Electroweak interactions involve both leptons and quarks and the relevant quantum numbers for the allowed fermion states are shown in Table 1.4.

In electroweak interactions the leptons numbers L_e, L_μ and L_τ are always conserved. Electroweak interactions among the leptons only occur within a single family and there is no inter-generational mixing. This is not the case for quarks in charged current interactions. Apparently the quark mass

Family			T	T_3	Y	Q
$\begin{pmatrix}\nu_e\\ e\end{pmatrix}_L$	$\begin{pmatrix}\nu_\mu\\ \mu\end{pmatrix}_L$	$\begin{pmatrix}\nu_\tau\\ \tau\end{pmatrix}_L$	1/2	+ 1/2	- 1	0
			1/2	- 1/2	- 1	- 1
e_R	μ_R	τ_R	0	0	- 2	- 1
$\begin{pmatrix}u\\ d\end{pmatrix}_L$	$\begin{pmatrix}c\\ s\end{pmatrix}_L$	$\begin{pmatrix}t\\ b\end{pmatrix}_L$	1/2	+ 1/2	+ 1/3	+ 2/3
			1/2	- 1/2	+ 1/3	- 1/3
u_R	c_R	t_R	0	0	+ 4/3	+ 2/3
d_R	s_R	b_R	0	0	- 2/3	- 1/3

Table 1.4: Weak isospin, hypercharge and electric charge for the quarks and leptons.

eigenstates are not exactly the same as the electroweak eigenstates. The quark eigenstates of electroweak charged current interactions are given by

$$\begin{pmatrix}u\\ d'\end{pmatrix}, \begin{pmatrix}c\\ s'\end{pmatrix}, \begin{pmatrix}t\\ b'\end{pmatrix} \tag{1.16}$$

where the mixing is described by the unitary Cabibbo-Kobayashi-Maskawa (CKM) matrix

$$\begin{pmatrix}d'\\ s'\\ b'\end{pmatrix} = \begin{pmatrix}V_{ud} & V_{us} & V_{ub}\\ V_{cd} & V_{cs} & V_{cb}\\ V_{td} & V_{ts} & V_{tb}\end{pmatrix} \cdot \begin{pmatrix}d\\ s\\ b\end{pmatrix} \tag{1.17}$$

Here the different V_{ij} are constants to consider in calculation of Feymann vertices connecting the quark i with the quark j and are fundamental in electroweak processes amplitude and cross section calculation. Although there are 9 elements in the CKM matrix, imposing unitarity, they found that CKM matrix is function of only 4 free parameters, which can be expressed as 3 angles and one CP (*charge-parity*) violating phase. This corresponds to the Cabibbo-Kobayashi-Maskawa form

$$V = \begin{pmatrix}c_1 & -s_1c_3 & -s_1s_3\\ s_1c_2 & c_1c_2c_3 - s_2s_3e^{i\delta} & c_1c_2s_3 + s_2c_3e^{i\delta}\\ s_1s_2 & c_1s_2c_3 + c_2s_3e^{i\delta} & c_1s_2s_3 + c_2c_3e^{i\delta}\end{pmatrix} \tag{1.18}$$

where s and c refer to $\sin$ and $\cos$ and their subscript the angle θ_i. δ in then the CP violating phase. Thus there are four parameters which are θ_1, θ_2, θ_3 and δ. CP violation, though very small, is now well established with CPT (charge, parity and time operations) believed to be the preserved underlying symmetry.
In a similar way it is possible to parametrize the CKM matrix in terms of λ, A, ρ and η according to the Wolfenstein parametrization, that maintain the unitarity to $\mathcal{O}(\lambda^4)$

$$V = \begin{pmatrix}1 - \lambda^2/2 & \lambda & A\lambda^3(\rho - i\eta)\\ -\lambda & 1 - \lambda^2/2 & A\lambda^2\\ A\lambda^3(1 - \rho - i\eta) & -A\lambda^2 & 1\end{pmatrix} + \mathcal{O}(\lambda^4) \tag{1.19}$$

This unified theory of the electromagnetic and weak interactions describes physical reality rather well at high energies where Q^2 is much greater than the mass of the partons involved. However, it has one major shortcoming in that it describes only mass-less particles. The Higgs mechanism, described in Section 1.4, is the most accredited mechanism by which particles in the SM acquire mass.

1.4 Symmetry Breaking and Higgs Mechanism

In 1964 Peter W.Higgs published a very short paper on "Broken Symmetries and the Masses of Gauge Bosons" [7] describing a mechanism by which gauge bosons can acquire mass. The Higgs mechanism has been fully incorporated into the Standard Model and it is thought to be responsible for the gauge boson and fermion masses. This mechanism gives rise to particle masses, at the price of introducing a new spin-0 scalar particle, called the Higgs boson.
It should be noted that other theories exist which attempt to explain spontaneous symmetry breaking and particle masses but are not considered in this brief overview.
In order to give mass to the gauge boson , a scalar field Φ and potential term $V(\Phi) = \mu^2|\Phi|^2 + \lambda|\Phi|^4$ is introduced in the electroweak Lagrangian given in Eq. 1.4 as

$$\mathscr{L}_\Phi = |D_\mu \Phi|^2 - \mu^2|\Phi|^2 - \lambda|\Phi|^4. \tag{1.20}$$

If μ^2 is positive then the potential $V(\Phi)$ is symmetric about its minimum which is 0. However, in the case where $\mu^2 < 0$ the potential has a minimum at

$$|\Phi| = \sqrt{\frac{-\mu^2}{2\lambda}}$$

as can be seen in Figure 1.2.

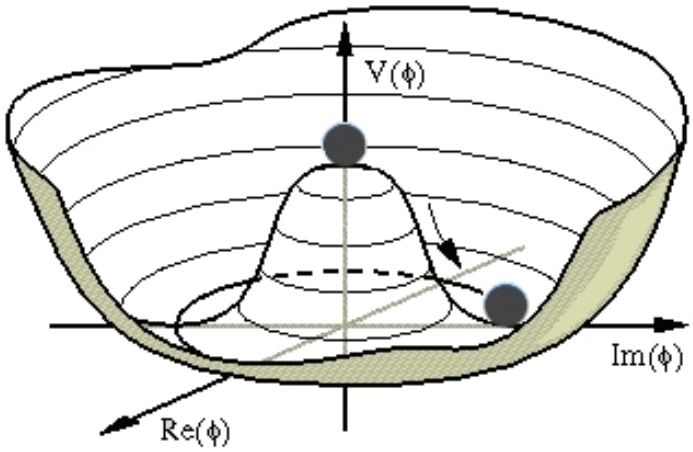

Figure 1.2: Higgs potential $V(\phi)$ for $\mu < 0$.

The ground state is said to have spontaneously picked a direction, which has given rise to a non-zero vacuum expectation value and a broken symmetry. The complex doublet Φ can be written in terms of the vacuum expectation value and two real fields with zero vacuum expectation value ξ and H as

$$\Phi(x) = exp\left(\frac{i\xi(x)\cdot\tau}{2\ v}\right)\begin{pmatrix}0\\(v+H(x))/\sqrt{2}\end{pmatrix} \tag{1.21}$$

where $v = \sqrt{-\mu^2/\lambda}$. Here, H will be the Higgs field and $\xi(x)$ are non-physical fields known as Goldstone bosons. Since the SM theory must be invariant under local gauge transformations, with

an appropriate gauge transformation is possible to cancel the dependence from the ξ fields. The gauge of choice is called the unitary gauge where

$$\Phi(x) = \frac{1}{\sqrt{2}} \begin{pmatrix} 0 \\ v + H(x) \end{pmatrix} \tag{1.22}$$

and the Lagrangian $\mathcal{L}_\Phi$ becomes

$$\mathscr{L}_\Phi = \frac{1}{2}(\partial H)^2 + \frac{1}{4}g^2 W^+W^-(v+H)^2 + \frac{1}{8}\left(\frac{gg'}{e}\right)^2 ZZ(v+H)^2 - V\left(\frac{1}{2}(v+H)^2\right). \tag{1.23}$$

What has happened here is that the goldstone bosons ξ have vanished and as a result, the gauge boson have acquired terms which can be identified as mass terms. For the W and Z bosons they can essentially be read off the Eq. 1.23 and are given by

$$M_W = \frac{1}{2}gv, \qquad M_Z = \frac{1}{2}\frac{gg'}{e}v. \tag{1.24}$$

The Higgs itself has an associated mass term coming from the potential term V

$$M_H = \sqrt{-2\mu^2}. \tag{1.25}$$

Recall that g and g' are related by the electroweak mixing angle θ_W. It follows that M_W and M_Z are related by

$$M_W = M_Z \cos\theta_W. \tag{1.26}$$

Experimentally one can measure both M_W and M_Z and given the relationship between g and g' show that $v = 246$ GeV [8]. Then the only undetermined parameter is μ which implies that the mass of the Higgs is undetermined.

Electroweak symmetry breaking and the Higgs mechanism have thus far provided a mechanism for gauge boson masses. It is still lacking a mechanism by which quarks and leptons acquire mass. Fermion masses are generated in the Higgs mechanism by what is called the Yukawa coupling. The Yukawa interaction term in the Lagrangian for a lepton is given by

$$\mathscr{L}_l = -G_l[\bar{l}_R(\Phi^\dagger l_L) + (\bar{l}_L\Phi)l_R] \tag{1.27}$$

for the singlet l_R and doublet l_L where G_l is a coupling constant. In the unitary gauge this becomes

$$\mathscr{L}_l = -\frac{1}{\sqrt{2}}G_l v\bar{l}l - \frac{1}{\sqrt{2}}G_l H\bar{l}l \tag{1.28}$$

from which the lepton mass can be read off as

$$M_l = \frac{1}{\sqrt{2}}G_l v.$$

The direct coupling of the leptons to the Higgs is evident in the $H\bar{l}l$ term in Eq. 1.28. Note although the Higgs mass is not known, its couplings to all particles are well defined and depend on the particle masses.

Similarly for the quarks, a Yukawa coupling can be added of the form

$$\mathscr{L}_q = -\sum_{i=1}^{3}\sum_{j=1}^{3}\left[\tilde{G}_{ij}\overline{u_{iR}}(\tilde{\Phi}^\dagger D_{jL}) + G_{ij}\overline{d_{iR}(\Phi^\dagger D_{jL})}\right] + \text{h.c.} \tag{1.29}$$

where u_i and d_i refer to the up and down-*type* quarks. Here G is related to the quark mass matrices by

$$M^u_{ij} = \frac{v}{2}\tilde{G}_{ij}, \qquad M^d_{ij} = \frac{v}{2}G_{ij}.$$

Chapter 2

Diboson physics

Contents

2.1 Z Boson

The interactions mediated by the Z boson were not noticed until about a half century ago, when observation of non-leptonic decay modes of strange mesons first hinted the need to complement the earlier $V - A$ theory with neutral intermediate boson. By 1967, however, it was a key unobserved piece of the near-modern electroweak theory. Thereafter, the Gargamelle experiment (1973) saw the evidence for it in neutrino-nucleon collision where lepton-less neutral current collisions accompained the charged current $\nu+$ nucleon $\rightarrow l^{-}+$ hadrons events predicted by the $V - A$ theory. With its direct observation at UA1 experiment in 1983 as a few resonant events in the dielectron mass spectrum, detailed studies of the Z's properties began.
The Z decays as shown in Table 2.1.

2.2 Z^0 properties

In the years after the discovery of Z boson, different experiments worked a lot to study its properties, especially its mass, width and branching ratios. In Sections 2.2.1 and 2.2.2 are described the main results obtained with the study of Z properties by the two main collider that studied it, LEP and SLAC.

Z Decay modes	Fraction $\mathbf{\Gamma_i/\Gamma}$
e^+e^-	(3.363 ± 0.004) %
$\mu^+\mu^-$	(3.366 ± 0.007) %
$\tau^+\tau^-$	(3.370 ± 0.008) %
invisible	(20.00 ± 0.06) %
hadrons	(69.91 ± 0.06) %
$(u\overline{u}+c\bar{c})/2$	(11.6 ± 0.6) %
$(d\overline{d}+s\overline{s}+b\bar{b})/3$	(15.6 ± 0.4) %
$c\bar{c}$	(12.03 ± 0.21) %
$b\bar{b}$	(15.12 ± 0.05) %
$b\bar{b}b\bar{b}$	(0.036 ± 0.013) %

Table 2.1: Main Z decay modes.

2.2.1 LEP

The properties of the Z boson and the underlying electroweak theory were verified at LEP with several measurements, among these the overall production cross-section, the forward-backward asymmetries of the leptons and quarks, and the polarization of τ leptons. The experimental analyses of the Z line-shape (see Fig. 2.1) of the decay branching ratios and the asymmetries were performed with very high precision. The fit of the data[1] gave as results

$$M_Z = 91187.5 \pm 2.1 MeV \tag{2.1}$$

$$\Gamma_Z = 2495.2 \pm 2.3 MeV \tag{2.2}$$

$$\sin^2\theta_{\text{eff}} = 0.23147 \pm 0.00016. \tag{2.3}$$

Thus, the electroweak sector of the Standard Model successfully passed the examination at the per-mille level, as highlighted by global analysis of the electroweak mixing parameter $\sin^2\theta_W$. Figure 2.2 shows the observables that were precisely measured at LEP: the result was very satisfying.

However, beyond this most stringent test of the electroweak theory itself, Z physics at LEP allowed important conclusions to be drawn on several other aspects of the Standard Model and potential physics beyond it. The first of these concerned the three families of leptons in the Standard Model. The width of the $Z \to ll$ depends on the number of lepton families. Comparing Λ_Z and $\Lambda_{Z\to ll}$ could be determined the number of light neutrinos. The ensuing difference determines the number of light[2] neutrino species to be:

$$N_\nu = 2.985 \pm 0.008\ . \tag{2.4}$$

Thus, LEP put the lid on the Standard Model with three families of matter particles.
Other succesfully results have been reached by LEP regarding b and t-physics. By analysing rate and angular asymmetries in Z decays to b-quark jets at LEP and complementing this with production rates at the lower energy collider PETRA, the isospin of the b-quark could be uniquely

[1] The fit is obtained combining also the measurement done in the same period by Stanford Linear Detector (SLD) at SLAC accelerator laboratory.

[2] We consider light neutrinos those with a mass of the order of eV, far smaller than other massive particles.

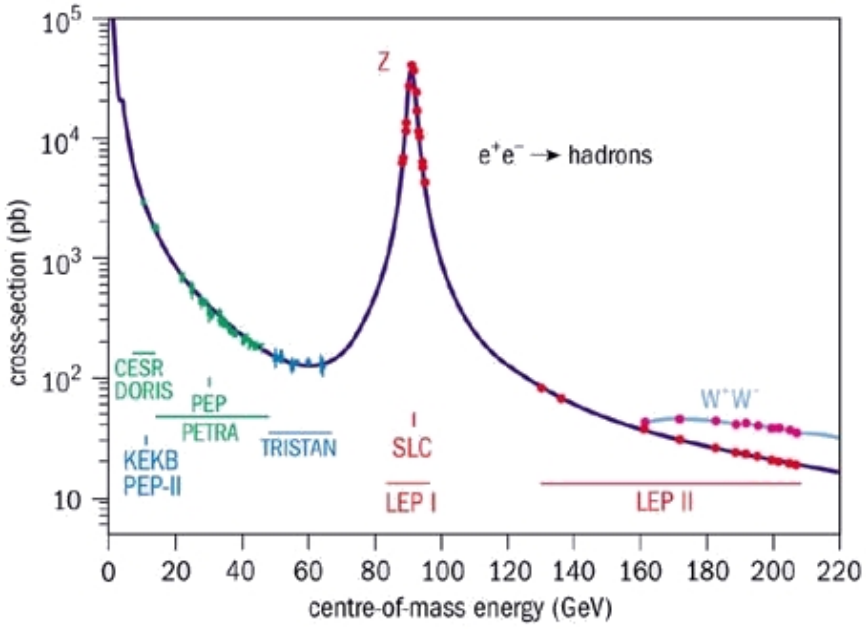

Figure 2.1: The e^+e^- annihilation cross-section to hadrons, from initial low energies in early colliders to the maximum energy at LEP.

determined. From Fig. 2.3 we can se that all measurements cross the point $[I_3^L, I_3^R]$ = [-1/2, 0], so an isospin partner to the b-quark with $[I_3^L, I_3^R] = [+1/2, 0]$ should exist, in other words, the top quark.

In addition to this, since virtual top quarks affect the masses and couplings of the electroweak gauge bosons, it was possible to give the first prediction of the top quark mass

$$m_t = 173^{+22}_{-24}\text{GeV} \tag{2.5}$$

before the top quark existance was established at the Tevatron collider and its mass confirmed by direct measurement. This was truly a triumph of high-precision experimentation at LEP coupled with theoretical high-precision calculations at the quantum level of the Standard Model.

2.2.2 SLAC

In the same period LEP started to study Z properties the SLAC (Stanford Linear Accelerator Collider) improved the pre-existing accelerator to produce 50 GeV $e^{\pm}$ beams for e^+e^- collisions. The Stanford Large Detector (SLD) was designed and built to study the Z properties especially in the heavy flavour decay channel. The main feature and difference of SLAC was the use of longitudinal polarized e beam. This permitted to study with high precision the angular asymmetries of polarized Z produced. SLD measured the parity-violating parameter A_b by analyzing the left-right (back-forward) asymmetry of b quarks in $e^+e^- \rightarrow Z \rightarrow b\bar{b}$ with different analysis techniques. Similaryly was studied the asymmetry parameter A_c from $Z \rightarrow c\bar{c}$ decay. From data collected from

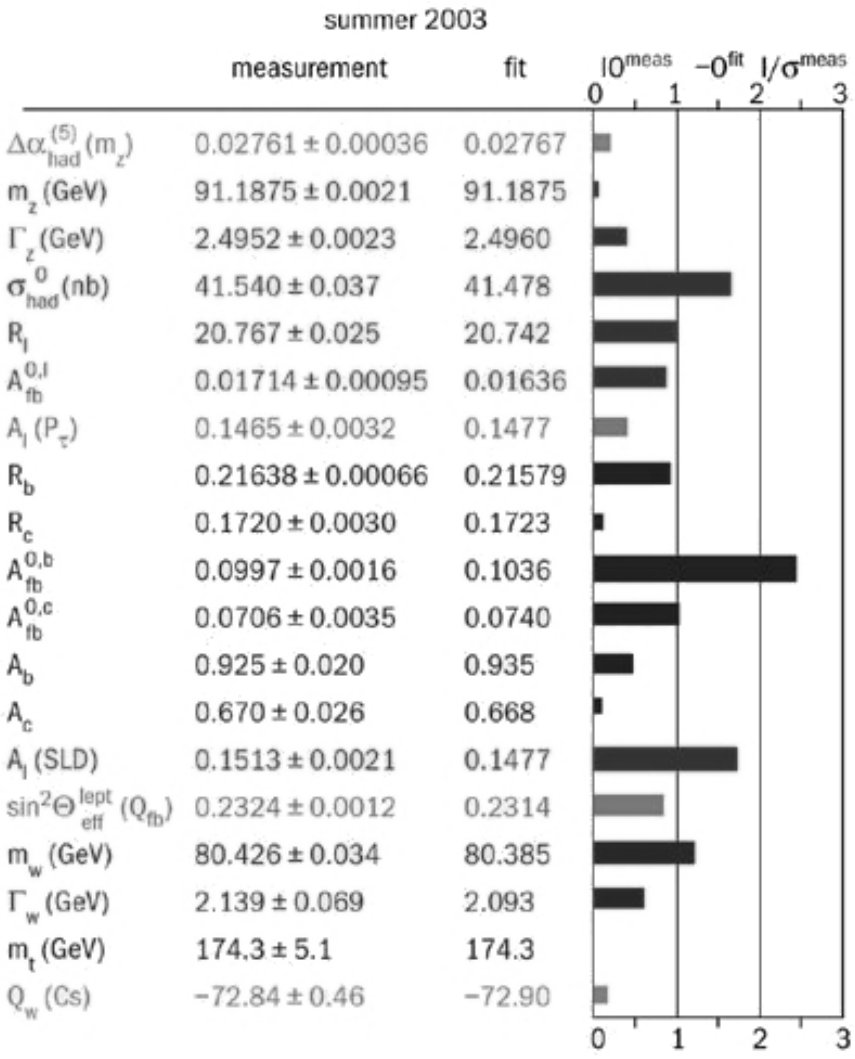

Figure 2.2: Precision observables of the electroweak part of the Standard Model, measured at LEP (elsewhere if indicated).

1993 to 1995, in a sample of 150000 Z the asymmetry measurement gave

$$Ab = 0.910 \pm 0.068(stat.) \pm 0.037(syst.) \tag{2.6}$$
$$Ac = 0.642 \pm 0.110(stat.) \pm 0.063(syst.)\ . \tag{2.7}$$

Combined with the results found at LEP those two experiments gave a precise measurement of the most important Z properties. These measurements were found to be in a really nice agreement with the SM prediction, testing not only the tree-level theory, but also its quantum corrections.

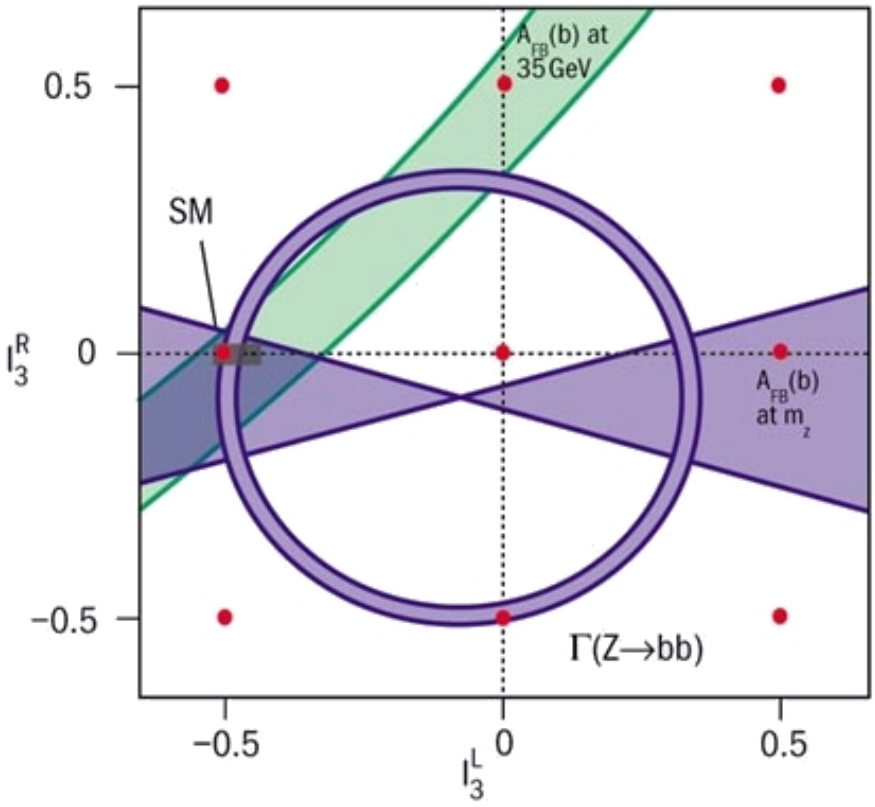

Figure 2.3: Determining the weak isospin of the bottom quark. The blue circle represents the partial Z decay width to $b\bar{b}$ pairs at LEP; blue wedges are the forward-backward asymmetry at LEP; and the green strip is the cross-section at PETRA.

2.3 Diboson Physics

After the discovery of the Z and W boson, with all their features, many physical studies have been done to measure the cross-sections of processes involving the production of two of such massive vector bosons. These kind of processes are less frequent than those involving just one vector boson and needed some more years to be studied.
Study dibosons production is very important to understand physics processes. The Higgs boson directly couples with a pair of vector bosons and resonances in their invariant mass can show the H. Trilinear Gauge boson Couplings (TGCs) are predicted by SM with relatively high precision and deviation can be ascribed to new phenomena. For further details about TGCs and *anomaous*-TGCs, see [9]. In the following we propose a short review of the foundamental analysis done during the past years at different colliders (leptonic and hadronic) involving diboson cross-sections.
The dibosons production has been studied both in electron-positron colliders (LEP,SLAC) and in hadronic collider (Tevatron,$p\bar{p}$ collisions). In the two different environment dibosons are produced through different processes that will be discussed in the following two sections. First measurements of diboson cross-sections have been done at LEP collider; since LEP was an e^+e^- collider , the only boson pairs that could have been produced were ZZ and W^+W^- while at Tevatron, several

measurements have been done in $p\bar{p}$ collisions of ZZ, W^+W^- and $ZW^\pm$ production cross section.

2.3.1 LEP

At LEP collider the ZZ diboson events were produced by e^+e^- collisions by mean of the processes illustrated by Feynman diagrams in Figure 2.4

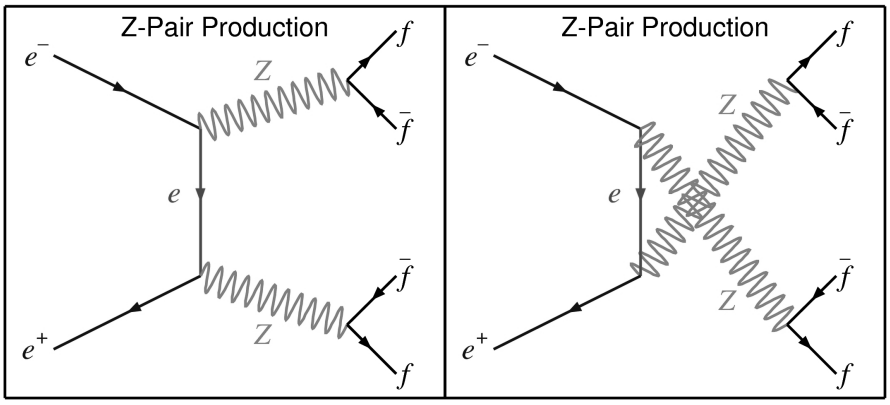

Figure 2.4: Tree level Feynman diagrams for ZZ production at the LEP collider.

The first evidence of the **ZZ** production was studied during 1997 by the DELPHI experiment [10], when LEP was operating at a center of mass energy of $\sqrt{s} = 182.6$ GeV, corresponding to the threshold for this channel. In the following years the analysis was extended with the growth of the center-of-mass energy, from $\sqrt{s} = 182.6$ GeV to $\sqrt{s} \simeq 207$ GeV, collecting totally 665.3 pb^{-1}of data. The choice of the DELPHI experiment was to select fermion pairs in a narrow range around the Z mass value, from 81 GeV to 101 GeV, for both fermion pairs reconstructed and then to scale the calculated cross section with the ratio of the theoretical total cross section and the one in the four fermion choosen window.
All the results obtained in the different final states studied, $q\bar{q}q\bar{q}$, $l^+l^-q\bar{q}$, $\nu\bar{\nu}q\bar{q}$, $\nu\bar{\nu}l^+l^-$ and $l^+l^-l^+l^-$ have been combined to obtain the final cross sections at the different energies, listed in Table 2.2 and shown in Figure 2.5: all the results are in perfect agreement with the SM prediction.

Similar analyses have been done by the other LEP experiments, ALEPH, L3 and OPAL but we will not discuss them further here.

2.3.2 Tevatron

At the Tevatron, the production of two Z bosons is much less frequent than single Z processes and it is dominated by qq annihilation and scattering, as shown in Figure 2.6. The inclusive Standard Model cross section is predicted to be 1.4 $\pm$ 0.1 pb. Most of the events produced decay to four or two jets and are hidden by the higher-rate QCD and single-Z background processes. Only very recently the two Tevatron collaborations have become sensitive to the very rare four-leptons ZZ decays.

$\sqrt{s}$ [GeV]	$\sigma(ZZ)$ [pb]	SM prediction [pb]
183	$0.40^{+0.21}_{-0.16} \pm 0.02$	0.25
189	$0.53^{+0.12}_{-0.11} \pm 0.02$	0.65
192	$0.70^{+0.37}_{-0.31} \pm 0.02$	0.78
196	$1.08^{+0.25}_{-0.22} \pm 0.02$	0.90
200	$0.77^{+0.21}_{-0.18} \pm 0.02$	0.99
202	$0.90^{+0.33}_{-0.29} \pm 0.02$	1.00
205	$1.05^{+0.23}_{-0.20} \pm 0.02$	1.05
207	$0.97^{+0.16}_{-0.15} \pm 0.02$	1.07

Table 2.2: Cross section obtained by DELPHI measurements. The first errors are statistical while the seconds are systematics.

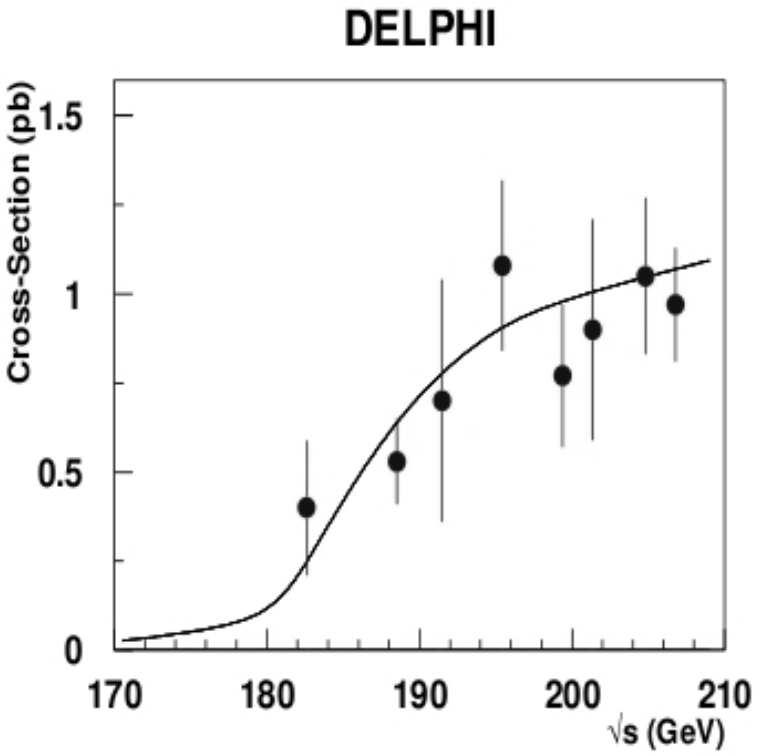

Figure 2.5: Combined cross-sections measured from data collected in 1997-2000. The errors shown are sums in quadrature of the statistical and systematic errors.

Recent analysis at CDF and $D\emptyset$, showed important results on diboson physics and obtained relevant constraints about new physics. At Tevatron $\mathbf{WW}$ production cross section at next-to-leading order (NLO) is expected to be 12.4 ± 0.8 pb. The first observation of that has been reported by $D\emptyset$, that found 25 candidates, of which 8.1 $\pm$ 1.0 was expected to be background, in approximately 250 pb^{-1}of data; this correspond to a measured cross section $\sigma(WW) = 13.8^{+4.3}_{-3.8}(stat.)^{+1.2}_{-0.9}(syst.) \pm 0.9(lum)$

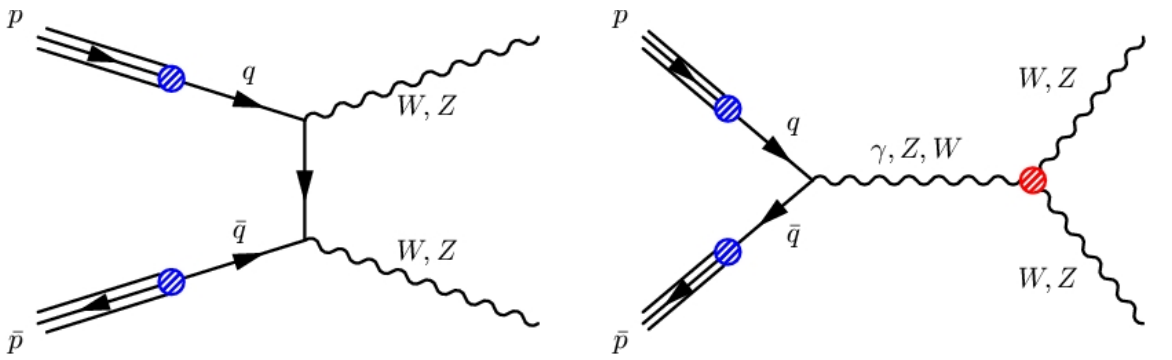

Figure 2.6: Tree-level t-channel(a) and s-channel(b) Feynman diagram for ZZ diboson production at the Tevatron.

pb with 5.2 σ of significance [11], consistent with SM prediction. CDF most recent analysis, on approximately 3.6 fb^{-1} of data, based on a likelihood ratio method calculated a cross section $\sigma(WW) = 12.1 \pm 0.9(stat.)^{+1.6}_{-1.4}(syst-)$ pb [12], again consistent with SM predictions.

WZ production cross section at NLO at Tevatron is expected to be 3.7 $\pm$ 0.3 pb. It was first observed by CDF collaboration with a data sample of approximately 1.1 fb^{-1} in the $WZ \rightarrow l\nu l'l'$ channel (l=e or μ)[13]. More recent measurements have been done both by CDF and $D\emptyset$ in the $WZ \rightarrow l\nu l'l'$channel: CDF measured in approximately 1.9 fb^{-1}a cross section of $\sigma(WZ) = 4.3^{+1.3}_{-1.0}(stat.) \pm 0.4(syst.)$ pb while $D\emptyset$ measured in approximately 1 fb^{-1} a cross section of $\sigma(WZ) = 2.7^{+1.7}_{-1.3}(stat + syst)$ pb [14]. CDF also reported the evidence of WW and WZ with W/Z decaying to jet-jet $WW/WZ \rightarrow l\nu jj$[3]. The branching ratio for this process is higher than the leptonic decay channel but it has not been measured before at hadron colliders because of the large background due to $W + jets$ events. The analysis in this particular channel, using 2.7 fb^{-1}of data give a cross section of $\sigma(WW/WZ) = 17.7 \pm 3.9$ pb with a significance of 5.4 σ.

ZZ The decay channels in which there is the best sensitivity at Tevatron are $ZZ \rightarrow llll$ and $ZZ \rightarrow ll\nu\nu$. The former, considered in the analysis presented in this thesis, has a very low background but also a small branching ratio, while the latter has a greater branching ratio but a higher background due mainly to $Z + jets$ and WW events. In the $ll\nu\nu$ channel, using about 1.9 fb^{-1}CDF found 276 candidates of which 14 $\pm$ 2 are expected to be ZZ signal [15], while $D\emptyset$ made his analysis using approximately 2.7 fb^{-1}and founding 28 (15) $ee\nu\nu(\mu\mu\nu\nu)$ candidates with an expected background of 15.6 $\pm$ 0.4 (10.9 $\pm$ 0.3) events[16]. Both these analyses have been combined by both the experiments with the parallel analysis in the $llll$ channel, CDF using 1.9 fb^{-1}and $D\emptyset$ using 1.7 fb^{-1} . The final result for the CDF analysis is a cross section of $\sigma(ZZ) = 1.4^{+0.7}_{-0.6}(stat + syst)$pb [15] with a significance of 4.4 σ while $D\emptyset$ found a cross section of $\sigma(ZZ) = 1.60 \pm 0.63(stat)^{+0.16}_{-0.17}(syst)$ pb [17]with a total significance of 5.7 σ; both measurements are perfectly consistent with the SM prediction.

[3] It is not possible with actual jets resolution to distinguish between a W jet pair and a Z jet pair so the analysis has been done combining the two processes.

2.3.3 LHC perspective in Diboson Physics

The study of mutiple gauge-boson production at the LHC provides a direct test of the non-Abelian structure of the standard model (SM) at energy scales never reached before and is a starting point for the observation of physics beyond the standard model.The cross sections of diboson production at the LHC (pp collisions at $\sqrt{s} = 14$ TeV) is nearly 10 times or more higher than at Tevatron so in the near future, the LHC could be the primary source of diboson production and new physics effects might become evident with high statistics. The diboson production is also an important and irreducible background to the search of the new physics therefore a detailed understanding of diboson production is needed in the first phase of LHC data-taking before any new discovery can be claimed. At the moment some preliminary studies have been made from both CMS and ATLAS (the two multi-purpose experiments at the LHC), using Monte Carlo samples of several processes involving dibosons.
ATLAS studied the possibility to measure the production cross section of WW in the dilepton decay channel $W^+W^- \rightarrow l^+\nu l^-\overline{\nu}(l = e, \mu)$. The main background contributions to this channel are from Z+jets, W+jets and Drell-Yan processes with large $\not{E}_T$. In Table 2.3[18] are listed the signal and background yield in $1\mathrm{fb}^{-1}$. The $e\mu$ channel has excellent detection sensitivity for the signal

	ee	$\mu\mu$	$e\mu$
N_S	36.7	37.6	284.4
N_B	188.6	112.1	59.4
S_L	2.59	3.38	25.3
$N_S/\sqrt{N_B}$	2.67	3.55	36.9

Table 2.3: Expected WW signal and background yield for an integrated luminosity of 1 fb^{-1}To calculate the expected significance of signal observation is used $S_L = \sqrt{2lnQ}$, where $Q = (1 + N_S/N_B)^{N_S+N_B}e^{-N_S}$.

because the rejection of background from DY can be well controlled.
CMS has studied instead the possibility to observe and measure the cross section of WZ [19] in the three lepton decay channel. In this case the background is due to ZZ events both in the four lepton decay, with one lepton missing, and in the $llb\bar{b}$ decay with the third lepton from b decay. In 1 fb^{-1} a yield of 97 signal for 22 background events is expected and are necessary just 150 pb^{-1} of data to observe a signal with more than 5 σ significance.
In the ZZ production at LHC the main contribution comes from t-channel $q\bar{q}$ scattering, while s-channel is strongly suppressed (see Fig. 2.6). CMS studied the performance of the detector for the $ZZ \rightarrow eeee$. In 1 fb^{-1} the signal expected is 3.6 events and a background of 0.28 events with a total systematic uncertainty on the cross section determination of $\sim 13\%$. ATLAS studied the $ZZ \rightarrow lll'l'$ channel ($l = e$ or μ)[20] with an analysis strategy similar to the one of this thesis; A yield of 13 signal events with negligible background is expected in the first 1 fb^{-1}.
LHC expectations on the anomalous trilinear gauge couplings are to reduce by a factor 10∼100 the limits on the TGC's parameters with 30 fb^{-1} of Data.
The four lepton final state is an important channel also for the search for the Higgs boson, in the decay channel $H \rightarrow ZZ \rightarrow lll'l'$. This channel is very clear for the search in the range 120 $< m_H <$ 180 GeV, with one Z off-shell but it is considered the *golden channel* for the search of the Higgs boson with a mass greater than 180 GeV, where both Z's would be on-shell. For the high

mass of the Higgs boson in this range, not only leptons but also Z's will have a large transverse momentum, improving the rejection of the background. According to the mass of the Higgs boson and to its production cross section and branching ratios a year or more of data collecting will be necessary to have a good significance for this signal observation. Then, if found, both ATLAS and CMS expect to measure the Higgs mass with a precision of $\sim$ 1 % or better and the different BR's with $\sim$ 20 %.
All these studies have been done assuming the LHC working at $\sqrt{s} = 14$ TeV and a luminosity of $\sim 10^{34}\ cm^{-2}s^{-1}$; if LHC would work at lower collision energy and lower luminosity it would take a longer time to achieve the results discussed above.

Chapter 3

The Tevatron Collider and CDF experiment

Contents

The Tevatron in Batavia, Illinois, USA is the first large-scale superconducting syncrotron in the world. Originally named the *Energy Doubler* since as a proton-synchrotron it was reaching twice the energy of the original Fermilab facility (the "Main Ring"), it began operation in 1983 in fixed target mode and in 1985 as a proton-antiproton collider.
Since 1985 various periods of collider or fixed target operations or shut down for upgrading the machine alternate with each other. The on-going (2009) collider operation period is named Run II. The present $p\bar{p}$ energy ($\sqrt{s}$) in centre of mass frame is *1.96 TeV*.
At the moment another high energy hadron collider (the *Large Hadron Collider*) is ready to start at CERN laboratory, colliding proton beams that, according to the project expectation, should reach a $\sqrt{s} = 14\ TeV$ and an instantaneous luminosity of $10^{33} - 10^{34}\ cm^{-2}s^{-1}$.
Along the Tevatron ring there are two apartment building-sized collider detectors, CDF and $D\emptyset$,

that have undergone extensive upgrades during the 6 years long (1996 to 2001) preparations for Run II. Both experiments host over 600 physicist from all over the world.
A schematic layout of the Fermilab accelerator complex is shown in figure 3.1.
In section 3.1 this complex (accelerator feeding the Tevatron, and Tevatron Collider) will be briefly described.

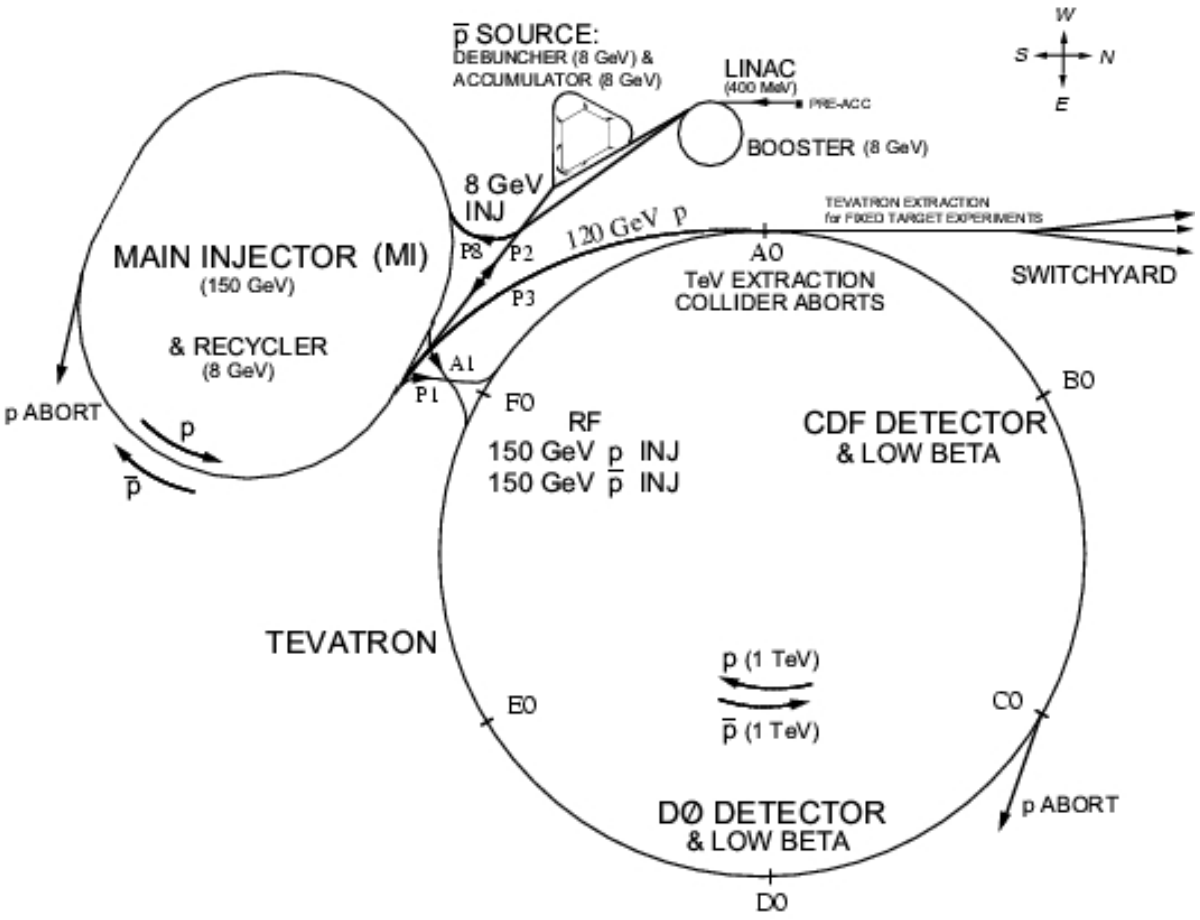

Figure 3.1: The accelerator complex of the Fermi National Accelerator Laboratory.

3.1 Acceleration Chain

3.1.1 Cockroft-Walton electrostatic Preaccelerator

Acceleration begins with a *Cockroft-Walton electrostatic Preaccelerator*. Here H^- ions are accelerated from a ion source to 750 KeV.

3.1.2 Linac

Ion bunches at 750 KeV are fed into the *Linear Accelerator (Linac)*. The Linac is approximately 140 m long and comprises two sections; in the first one five accelerating cavities with a drift tube

design fed by a single RF generator accelerate ions to approximatively 166 MeV. The second one, comprising 7 RF cavities fed by a more modern set of Klystron amplifiers, ramps ions by additional 400 MeV[1]. At the Linac exit the ion beam strikes a thin carbon target and turns into a proton beam by electron stripping.

3.1.3 Booster

Stripped protons enter the *Booster*, a 8-GeV syncrotron whose diameter is about 150 m. To maintain a constant circular orbit the dipole magnetic field in the Booster increases from 0.74 Tesla to 7 Tesla during acceleration.
Both Linac and Booster provide pulses up to $5 \cdot 10^{12}$ protons at a rate of about 5 Hz for antiproton production every 1.5 seconds, or $6 \cdot 10^{10}$ protons per bunch in series of 5 to 7 bunches, repeated 9 times per second (in average).

3.1.4 Main Injector

From the Booster the proton beam is fed into the Main Injector whose role is either to accelerate protons as needed for injection in the Tevatron and to deliver beam to the antiproton production target.
The original Tevatron injector was the Main Ring, built to provide primarily 400 GeV protons to fixed target experiments. The Main Ring limited aperture was a limit to the whole accelerator performances. The *Main Injector* was designed to solve this problem and located in separated tunnel for an easier operation of the complex.
The Main Injector is a synchrotron with a circumference of about 3 km. It is able to accelerate protons of 8 GeV energy up to 150 GeV. It operates at 120 GeV for antiproton production, while 150 GeV protons are delivered to the Tevatron.
The Main Injector is also used to give beam to number of fixed target experiments, noticeably on secondary neutrino beams.

3.1.5 Debouncher and Recycler: Antiproton production and storage

A pulse of $5 \cdot 10^{12}$ protons at 120 GeV is extracted every ~ 2.2 seconds from the Main Injector and directed to the antiproton station, a rotating 7 cm-thick target made of nickel alloys containing chromium, iron and other metals. The resulting particles spray contains some antiprotons with a broad momentum and wide-spread spatial distribution.
A cylindrical lithium lens (760 T/m) focuses the particles produced around the forward direction. Negative particles in 35 $mrad$ cone about the forward direction are selected by using a 1.5 T pulsed dipole magnet and injected in the *Debouncher Storage Ring*. Typically, $\sim$21 antiproton per 10^6 protons on target are collected.
In the Debouncher ring, a rounded triangular-shaped syncrotron with mean radius of 90 meters

[1] The 750 final energy is the result of a Linac upgrade, that took place in 1993 and increased the boost in the second Linac sector from 200 MeV to 400 MeV. This effort allowed to double the number of protons per bunch and to increase by about 50% the production rate of antiprotons.

stochastic cooling and bunch phase rotation[2] reduce by about 10 times the momentum spread in the bunches.
After each beam pulse the Debouncher is emptied. The antiproton bunches (with an energy of 8 $\pm$ 0.018 GeV) are transferred with a 60%-70% efficiency to the Antiproton Accumulator, a 75 m mean radius storage ring of larger acceptance housed in the same tunnel as the Debouncher. In the accumulator multiple beam pulses are stacked and $\overline{p}$ are further cooled to increase the antiproton phase space density.
For the time being problems in antiproton collection, cooling and stacking are among the main causes limiting the final Tevatron luminosity since a very small fraction of the proton incident on target produces antiprotons and only a part of these can be stored.
A further improvement of the antiproton source is the Recycler, a post-accumulator storage ring of constant 8 GeV energy, located in the Main Injector enclosure and composed of permanent magnets. Because of its larger acceptance it can store an antiproton current twice as large as the Accumulator.

When a new store is ready for collider operation, previously used antiprotons are transferred to the Recycler while protons are thrown away. Then new antiprotons are transferred from either Accumulator or the Recycler to the Main Injector in order to increase their energy up to 150 GeV. Antiprotons are finally transferred to the *Tevatron*, where an opposite proton beam of the same energy was previously stored.

3.2 The Tevatron

The Tevatron is a $1 - km$ radius synchrotron that comprises about 1000 superconducting magnets including 772 dipoles. Each dipole is approximately 6 m in length and 4 tons in weight. The superconducting coils are made up of niobium-titanium wires embedded in copper. A 4400 A current in the dipoles provides a 4.2 T magnetic field. All superconducting materials are kept at 4 K temperature.
As written in section 3.1.4 the Tevatron receives protons and antiprotons from the Main Injector at 150 GeV. At injection 36 bunches composed typically of 300×10^9 p are transferred at 150 GeV with a timing separation of 360 ns from each other.
Both protons and antiprotons orbit are in the same vacuum pipe. Electrostatic separators reduce to a negligible amount the unwanted interactions, by keeping the beams away from each at all points in the orbit helix [3].
Protons and antiprotons are accelerated to 980 GeV. A tour of the Tevatron takes about 21 μs. About one minute is needed to reach the final beam energy.
High-power focusing quadrupole magnets minimise the beam section at the interaction regions to maximise the collision rate.
The resulting transverse beam distributions may be approximated by 2D Gaussian functions, with $\sigma_T \approx 30\ \mu m$. The typical longitudinal dimension of a bunch is 60-70 cm. The event source is

[2] Stochastic technique is a way of narrowing the particle distribution in transverse and longitudinal momentum around the average value. There is not any accompanying beam-loss. This goal is achieved by applying iteratively a mechanism which recognises deviation from spatial orbit of a 8-GeV antiproton in upstream sensors and makes appropriate correction downstream.
[3] Intrabeam distance is typically 5 times the sum of the beam widths (in a Gaussian approximation).

roughly distributed longitudinally as a Gaussian with $\sigma_z = 28\ cm$[4].
Tevatron bunches are organised in three trains; within a train the inter-bunche time is 396 ns while inter-train time is 2.6 μs. The intra-train empty sectors are needed for the fast *kicker magnets* to abort the beam into a dump before the arrival of the next train in case of emergency.
In Figures 3.2 and 3.3 are respectively shown the integrated and peak luminosity of Tevatron through different runs.
The record peak luminosity reached by the Tevatron is $\sim 3.65 \cdot 10^{32}\ cm^{-2}s^{-1}$ corresponding to about 5 interactions per bunch-crossing.

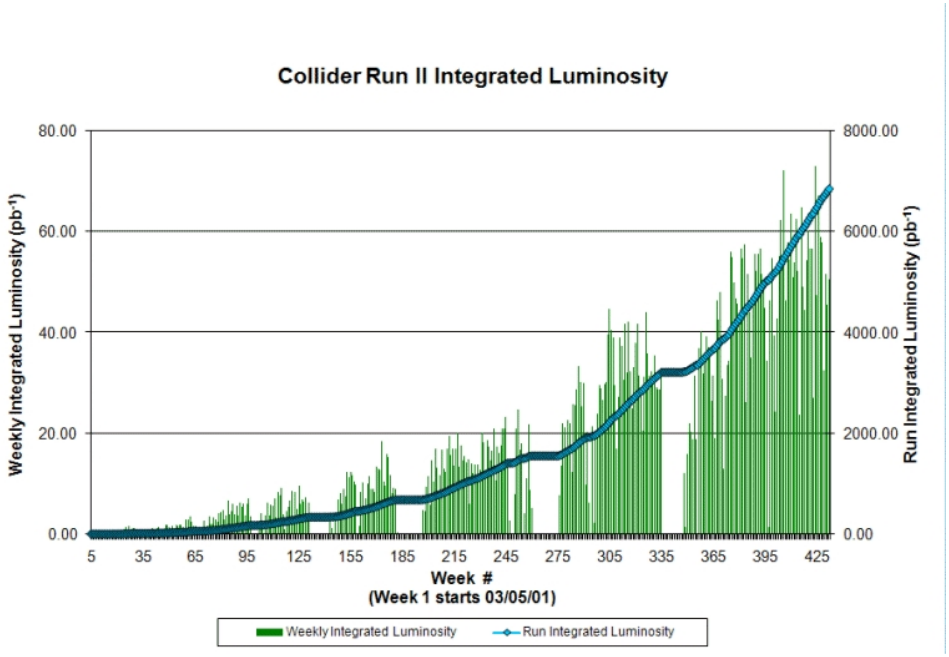

Figure 3.2: Run 2 Integrated luminosity as a function of time (up to June 2009).

3.3 The CDF experiment and detector

The Collider Detector at Fermilab (CDF) was designed to study $p\bar{p}$ collision at the Tevatron. Commissioned in 1987 it was upgraded in 2001 in order to be adapted to the higher collision rate coming from the increased instantaneous luminosity delivered by the accelerator.
The CDF coordinate system is a right handed coordinate system defined such that the z axis lay along the beam line, with the positive direction in the direction of the proton beam at the nominal (z_0) collision point. The positive y direction is defined to point vertically upward. This leaves the x direction pointing outward (roughly northwest) where unit vectors satisfy $\hat{z} = \hat{x} \times \hat{y}$.

It is useful to describe CDF detector geometry also using a cylindrical (r, ϕ, z) coordinate-system, where r is the radial distance from the beam line and ϕ is the polar angle in the plane perpendicular to the beam line. The origin is the geometric centre of the detector.

[4] The about 28 cm length of the interaction region is determined by the overlap of the two approximately longitudinally Gaussian bunches.

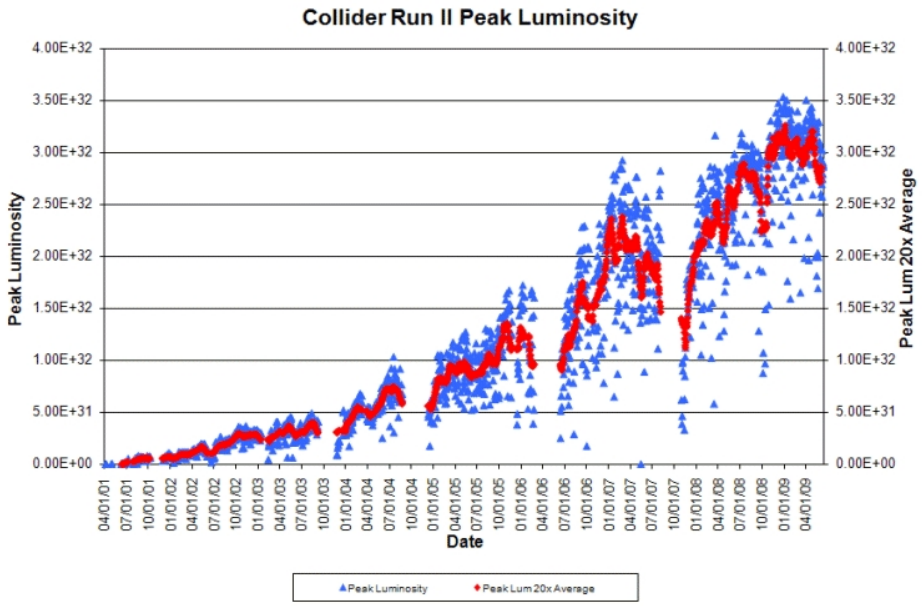

Figure 3.3: Run 2 Peak luminosity in the stores and its average, as a function of time (up to June 2009).

It is often convenient to use a polar variable invariant under boost along $\overline{z}$.
This variable is the *rapidity* defined as

$$y = \frac{1}{2}\ln\left(\frac{E + p \cdot cos\theta}{E - p \cdot cos\theta}\right) \tag{3.1}$$

where E, p, θ are respectively the energy, momentum and polar angle of the considered particle. At high energies and away from very fordward angles $y \approx \eta = -ln[tan(\theta/2)]$ called *pseudo-rapidity* [5].

3.3.1 Overview

The Run II Detector (Fig. 3.4 & 3.5) is composed of several components, each optimised for a specific task.
Starting from the interaction point and following the path of an outgoing particle within acceptance there are:

1. a tracking system enclosed by a superconducting solenoid (1.5 m in radius and 4.8 m in length), which generates 1.4 T magnetic field parallel to the beam axis. The magnetic field is uniform in the tracking region.

2. finely segmented calorimeters.

[5] In CDF literature are usually distinguished η_{det}, which is relative to the geometrical centre of the detector, and η, which is measured with respect to the interaction point z_0 where particles originated. Usually the former symbol is used for describing the detector geometry while the latter for outgoing particles. For simplicity the same symbol will be used in both cases.

3. planar muon drift chambers backed by scintillation counters.

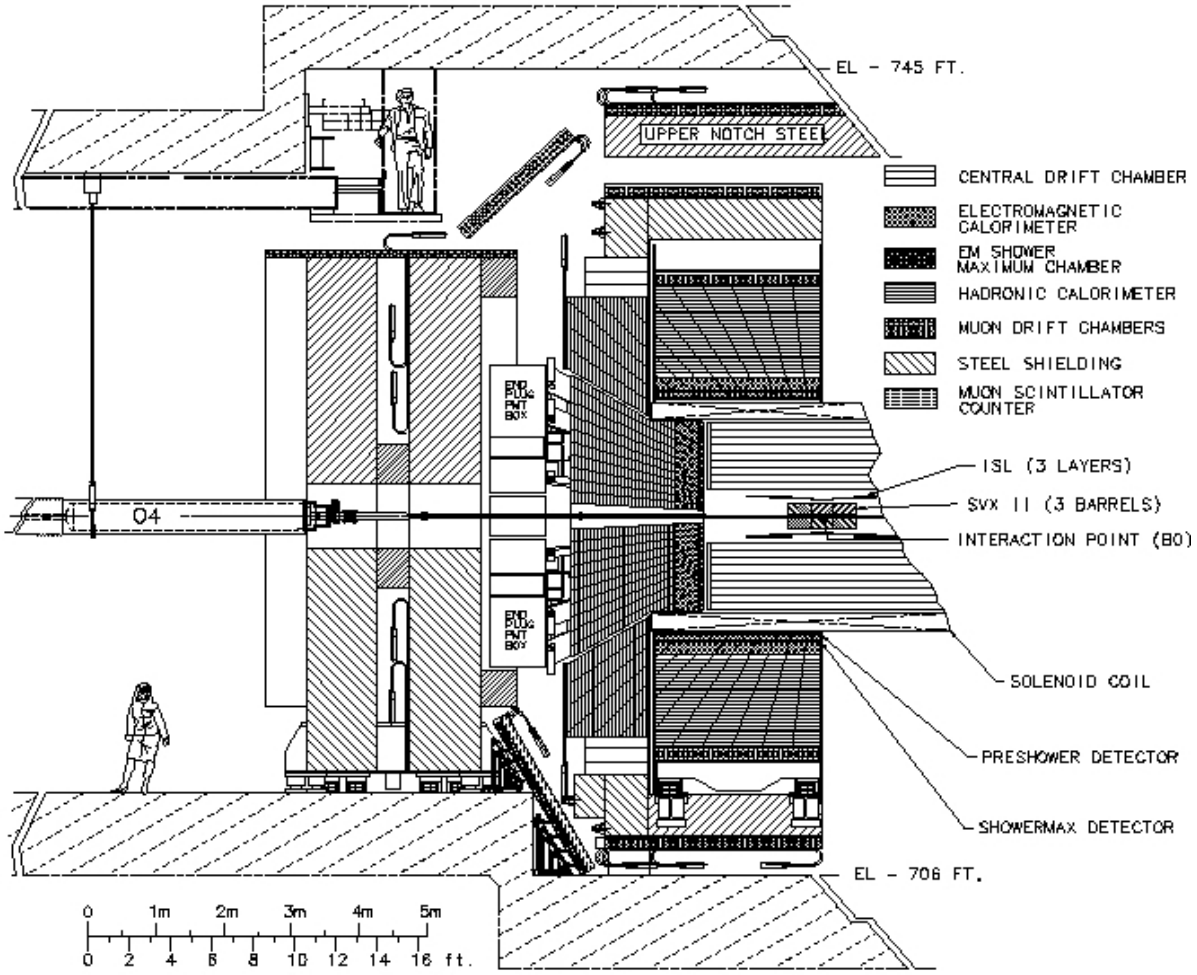

Figure 3.4: Elevation view of the CDF II detector.

In the next sections these sub-systems will be discussed.
Some of the components (the time-of-flight detector, the Cerenkov Luminosity Counters, the small angle spectrometers on beam pipe, etc.) of the full CDF II detectors have been neglected since are not used in this thesis.
A detailed description of the upgraded detector can be found in [21]

3.4 Tracking System

Charged particle within the tracking system acceptance encounter an inner silicon tracking system and outer gas drift-chamber as shown in Figure 3.6.

Within the solenoid field they follow helical trajectories which are measured by the system in order to estimate their momentum.

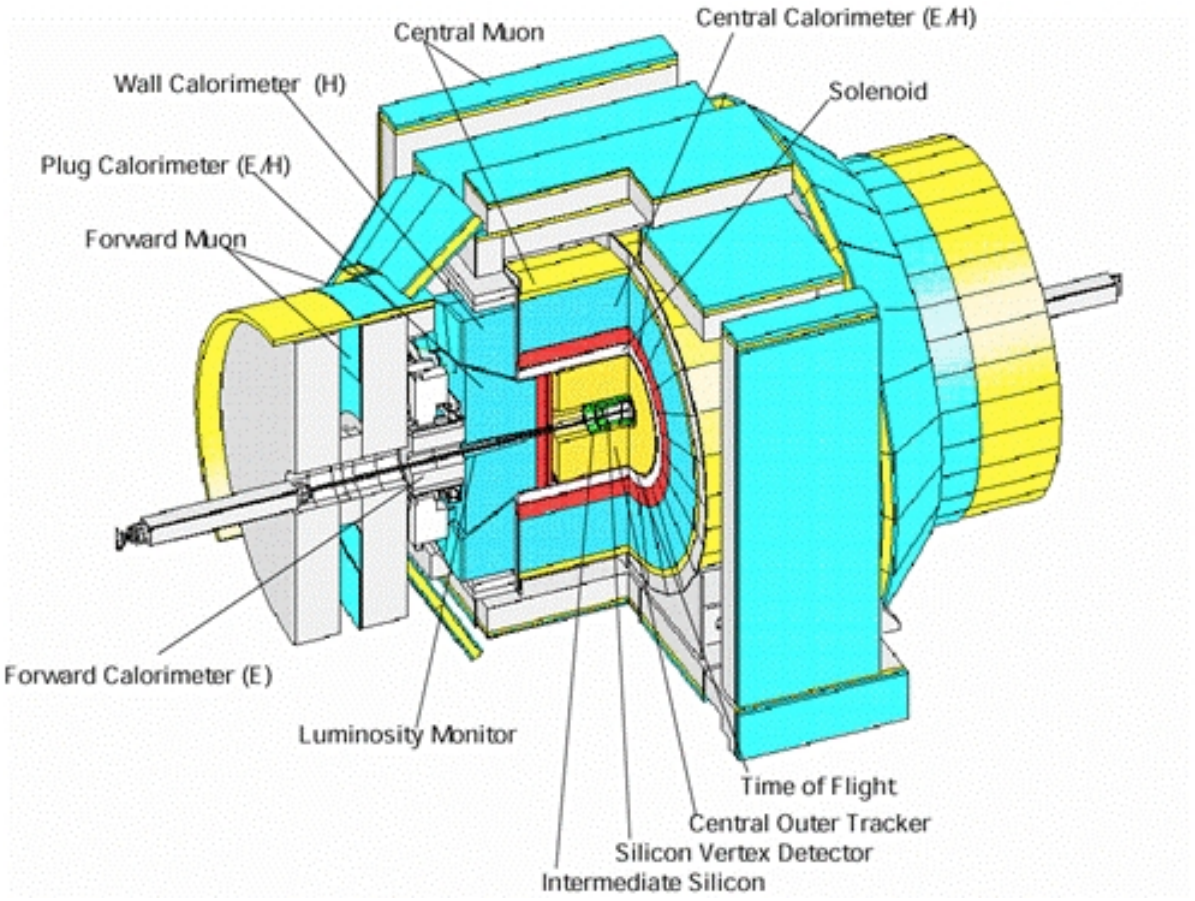

Figure 3.5: Isometric view of the CDF II detector.

3.4.1 Inner Tracker

The Inner Tracker is composed of eight layers (seven at $\theta = 90^\circ$) of silicon sensors arranged in approximately cylindrical sub-systems coaxial with the beam-pipe: Layer 00 (L00), the Silicon Vertex Detector (SVX II), and the Intermediate Silicon Layers (ISL). Figure 3.7 zooms on the Inner Tracker structure.

All silicon microstrip sensors have a space resolution of $\sim 12\ \mu m$ in the direction transverse to the beam. They also provide z-measurements with reduced accuracy.

L00

L00 is 90 cm long, radiation hardened single side micro strip detector, and it is mounted directly on the beam pipe. It is at radial distance of 1.35 to 1.62 cm from the beam axis. L00 purpose is to improve the track impact parameter (the measured distance of minimum approach to the beam axis) resolution ($\sim 25/30\ \mu m$) and compensate for the multiple scattering degradation for particles that travel across bulkhead.

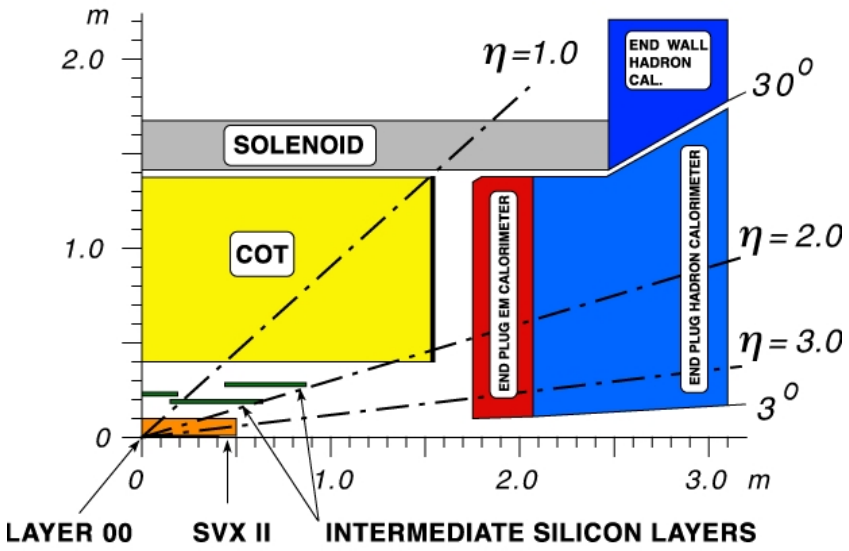

Figure 3.6: Longitudinal view of the Tracking System of the CDF II detector.

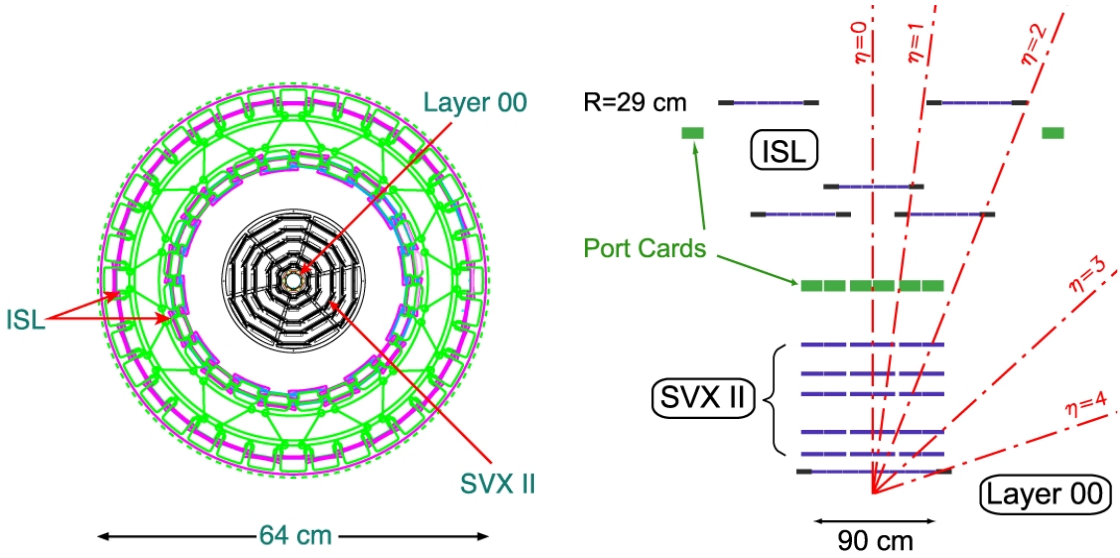

(a) x/y plane (b) detail

Figure 3.7: (a) Sketch of the silicon detector in a x/y projection. (b) Cutaway transverse to the beam of the three inner tracker sub-systems.

SVX II

SVX II, shown in fig 3.8, extends radially from 2.5 cm to 10.7 cm.

It is segmented into three 29 cm barrels along the z axis: this allows for a $|\eta| < 2.0$ coverage. Each barrel carries 5 layers of double-sided microstrip wafers. Four silicon wafers are mounted on light support structures called ladders. Twelve concentric ladders make a layer.

The double-sided imprint of the wafers allow for 3D position measurements: one side of the wafer has strips along the beam axis, the other one has either 90° or 1.2° stereo strips.

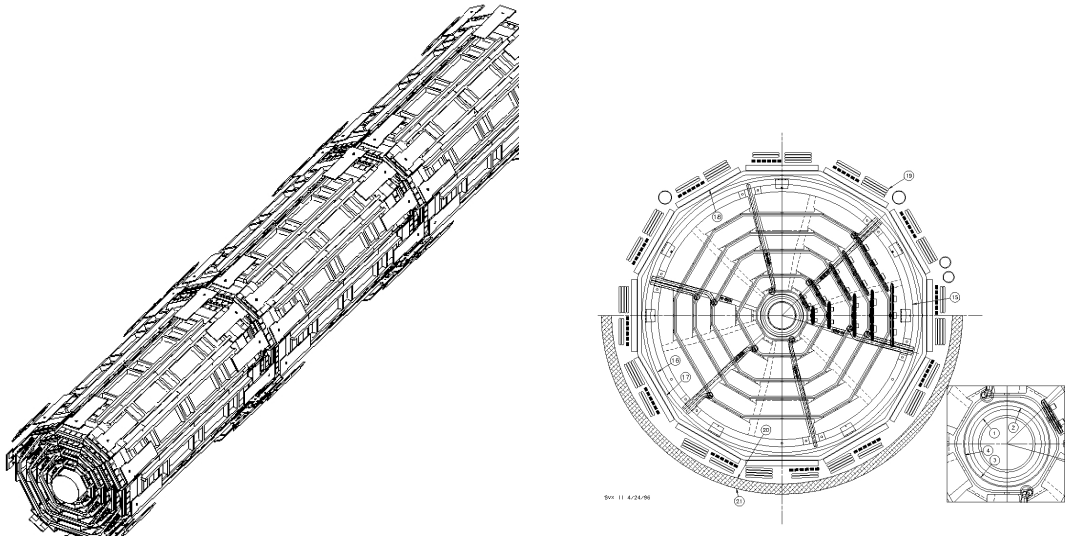

(a) Isometric (b) End-view

Figure 3.8: Isometric (a) and end-view (b) of the CDF Silicon Vertex Detector.

This sub-detector provides also some dE/dx information and has a 12 μm resolution in the direction transverse to the beam on the single hit.

ISL

The main ISL purpose is to compensate for the incomplete coverage of other sub-detectors in the region $|\eta| > 1$ by providing precision tracking at $1 < |\eta| < 2$. It consist of 5 layers of double sided silicon wafers (same wafers as for SVX II). Four layers are at $1 < |\eta| < 2$ (at radii of 20 and 28 cm, as shown in Fig. 3.7), one layer is at $|\eta| < 1$.
The combined resolution of the CDF inner trackers for high momentum tracks is ~ 40 μm in impact parameter and ~ 70 μm along z direction.

3.4.2 Central Outer Tracker

The COT (Central Outer Tracker) is an open-cell wire drift chamber filled with a gas mixture of Argon, Ethane and CF_4 in proportion 50%, 35% and 15%; it has a cylindrical shape and is radially right outside the ISL. Its internal and external radii are 43 cm and 137 cm respectively. The COT provides full tracking in the central region ($|\eta| < 1$), even if its maximum geometrical acceptance reaches up to $|\eta| < 2$ (see Fig. 3.6), where tracking performances are reduced.
The COT is a The COT is composed of 4 axial and 4 stereo[6] superlayers of azimuthal cells. Each cell has alternated sense and field shaping wires (Fig. 3.9). Within the cell width, the trajectory of a particle is sampled 12 times (by sense wires spaced 0.583 apart). Figures 3.9 show a portion of the COT endplate.

[6] Stereo superlayers are tilted at $\pm 2^\circ$ width respect to the z direction. Axial layers provide tracking information in $r - \phi$ plane, stereo layers are also sensitive to the z direction.

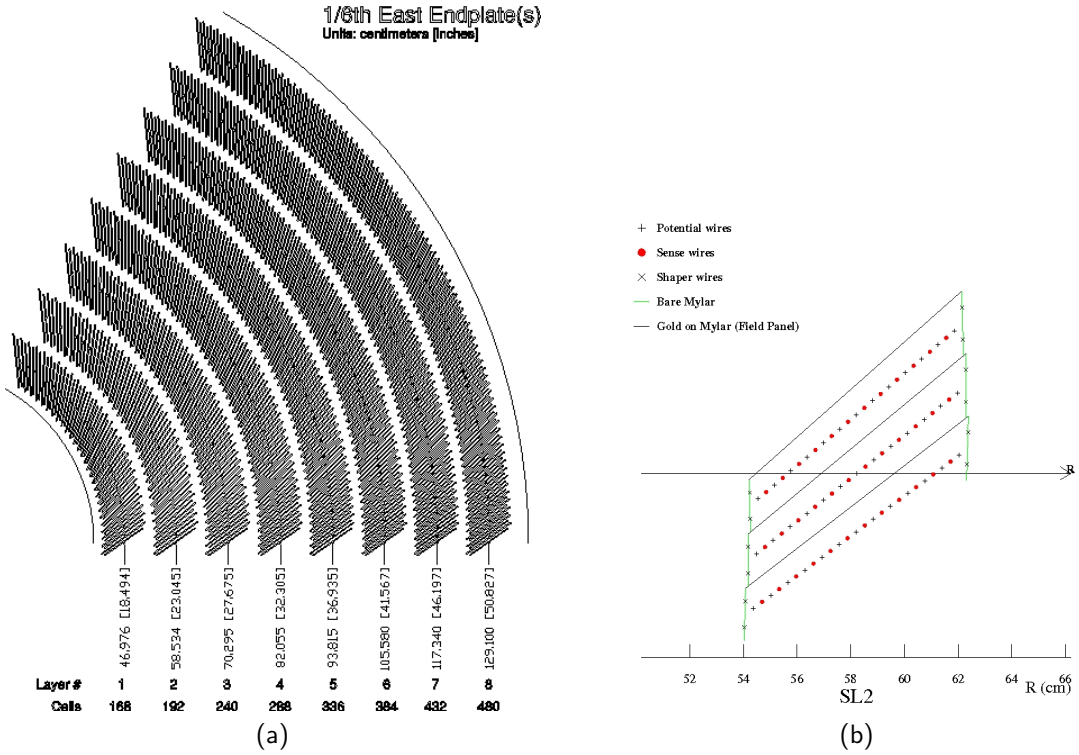

Figure 3.9: Slots housing the wire holding fixtures of one quadrant of a COT endplate (a). Drift and field wires in three cells (b). The horizontal arrow shows the radial direction.

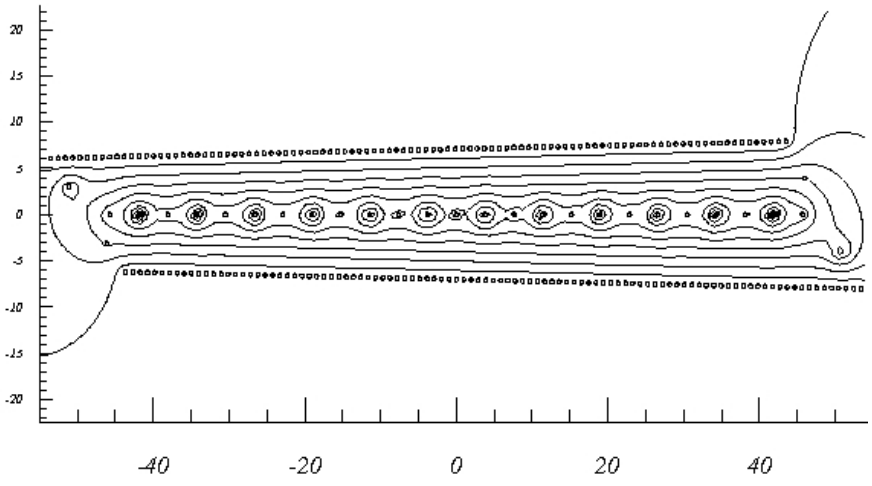

Figure 3.10: Equipotential lines in a COT cell.

Inside the solenoid magnetic field, the drifting electrons experience a Lorentz force which rotates their path. The cells are tilted by 35° with respect to the radial direction in order to make the

electrons drifting perpendicularly to the radius for optimal momentum resolution[7].
The single hit position is measured with an uncertainty of $\sim 140\ \mu m$ which translates into an overall transverse resolution

$$\sigma(P_T)/P_T = 0.15\% P_T[GeV/c] \tag{3.2}$$

P_T being the transverse momentum of the particle.

3.5 Calorimeters

The CDF calorimeter measures the particle energy by absorbing their energy and providing a signal proportional to it. CDF uses scintillators sampling calorimeters divided into an inner electromagnetic and an outer hadronic compartment. Both calorimeters are segmented into projective towers. Each tower consists of alternating layers of passive absorber material (Pb in the electromagnetic and Fe in the hadronic compartment) and plastic scintillator for shower sampling. The light from the scintillator plates is read out through wavelength-shifting bars or plates and (WLS) light guides by photo-multiplier tubes (PMT)(see figure 3.11).

High energy electrons and photons generate an electromagnetic shower which is mostly absorbed in the front calorimeter compartment[8]. For charged particles heavier than the electron, radiative energy losses are negligible to a first approximation.
Hadrons interact with the detector matter mostly through inelastic collisions with nuclei of the absorbing medium. Particles produced in the nuclear interactions can loose their energy by ionisation and secondary nuclear interactions. Mixed electromagnetic and hadron showers that originate are absorbed in the entire (em+had) calorimeter.
CDF calorimeters provide full azimuthal coverage and up to 3.6 in $|\eta|$. It includes the Central Electromagnetic Calorimeter (CEM) and the Central Hadronic Calorimeter (CHA) in the $|\eta| < 0.9$ region, the Endwall Hadronic Calorimeter (WHA) in $0.9 < |\eta| < 1.3$ and the electromagnetic and hadronic plug calorimeters (PEM,PHA) in $1.1 < |\eta| < 3.6$ (see figures 3.5-3.6).

3.5.1 Central Calorimeter

The central calorimeters, CEM, CHA and WHA are composed of two parts joining at the geometrical centre of CDF[9]. Central calorimeters are azimuthally divided into 24 wedges covering $\sim 15^\circ$ in ϕ each. Each wedge is divided into projective towers of size $\delta\eta = 0.1$.
The CEM calorimeter is made of 31 alternate layers of 0.5 cm plastic scintillator and 0.32 cm thick lead absorbers: the total amount of material is $18 \cdot X_0$ (X_0 is the electron radiation length). The CEM energy resolution is:

$$\sigma_{E_t}/E_T = 13.5\%/\sqrt{E_T[GeV]} \oplus 2\% \tag{3.3}$$

E_T being the energy of an electron or a photon hitting the calorimeter perpendicularly to its front. CEM also includes two additional specialised detector: the Central Electron Strip Chambers (CES) and the Central Preshower (CPR). CES is a combined strip/wire gas proportional chamber embedded

[7] For best momentum resolution, the optimal correlation between drift time and hit distance from wire is for electrons drifting in the direction transverse to the radius.
[8] A shower is a cascade of particle. In the case of photons and electrons the showers are composed mainly of electrons, positrons and photons.
[9] In this zone, $\eta = 0$, there is an instrumented area (*crack*).

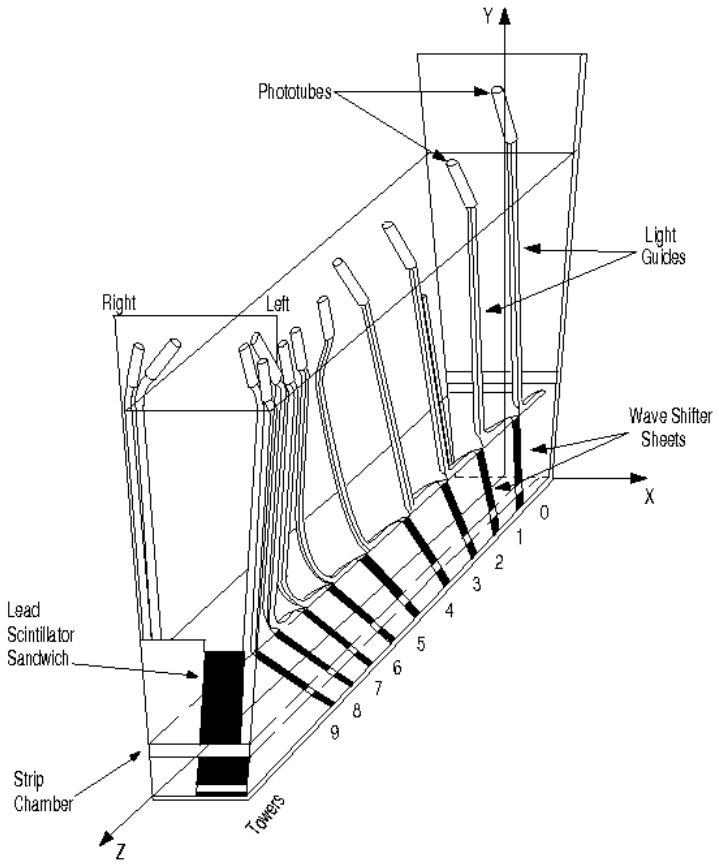

Figure 3.11: Light-shifter plates connected to light guides and to photomultipliers of the front electromagnetic sector of a central calorimeter wedge.

in CEM at about $6 \cdot X_0$ since there is expected the maximum longitudinal development of the electromagnetic shower. The CES purpose is to measure the position and the shape of electromagnetic showers in both transverse plane and longitudinal direction. CES resolution is about 1 cm in z and 1 mm in $r - \phi$. CPR is a set of scintillator tiles located in front of the calorimeter wedges which help distinguishing electrons from charged hadrons by gauging their probability of showering in the detector material prior to entering the calorimeter.

The CHA calorimeter, located behind CEM, is composed of 32 alternate layers of 1 cm plastic scintillators and 2.5 cm thick steel. The WHA calorimeter employs the same technology as CHA except for the smaller number of layers (15) and the larger thickness of the radiator medium (5 cm per layer). The total calorimeter thickness is $\sim 4.7\ \lambda_0$ (λ_0 is the absorption length) for both CHA and WHA.
Resolutions of CHA and WHA for perpendicular particle entrance are:

$$\sigma_{E_t}/E_T = 50\%/\sqrt{E_T[GeV]} \oplus 3\% \tag{3.4}$$

$$\sigma_{E_t}/E_T = 75\%/\sqrt{E_T[GeV]} \oplus 4\% \tag{3.5}$$

3.5.2 Plug Calorimeters

The PEM calorimeters (Fig. 3.12) have the same structure as the CEM: same tower segmentation in η, but finer in ϕ (a ϕ coverage of 7.5°) for $|\eta| < 2.11$, 22 layers of 4.5 mm thick lead alternate with 22 layers of 4 mm thick scintillator.
The PEM transverse energy resolution is:

$$\sigma_{E_T}/E_T = 16\%/\sqrt{E_T[GeV]} \oplus 1\% \tag{3.6}$$

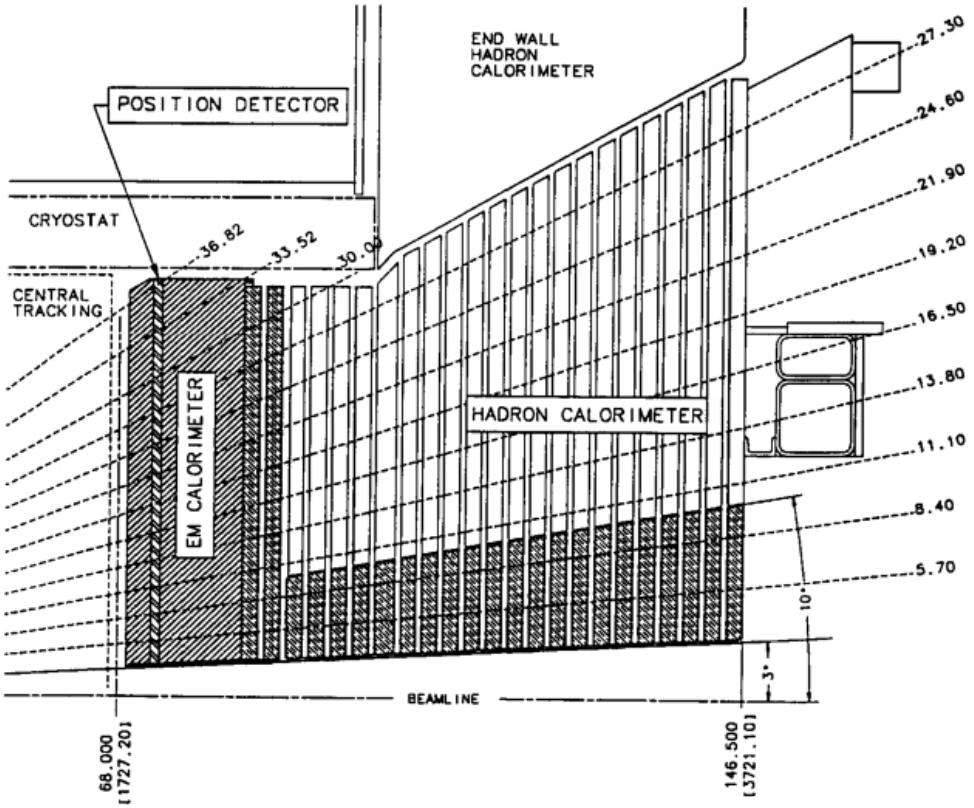

Figure 3.12: Longitudinal view of Plug Calorimeters.

As for CEM, PEM is equipped with a shower maximum detector (PES). More details can be found in [22]. PHA, located behind PEM, has the same tower segmentation. The technology is the same as for CHA, with 23 layers of 2cm thick steel absorber alternating with 6 mm thick scintillator. The total amount of material corresponds to $\sim$ 4.7 λ_0. PHA resolution is:

$$\sigma_{E_t}/E_T = 80\%/\sqrt{E_T[GeV]} \oplus 5\% \tag{3.7}$$

3.6 Muon Detectors

Muons interact electromagnetically but, since they have a higher mass than electrons, when they cross electromagnetical calorimeter they do not shower in it. At the typical energies they are

produced in $p\bar{p}$ collision they interact in calorimeters as minimum ionising particles (MIP) so the lose just a minimal fraction of their energy crossing it. For this reason systems dedicated to detect muons are located in the outermost shell of the detector. Muon momenta are measured in the tracker.
Four independent systems are used to detect muons in the $|\eta| < 1.5$ region: the Central Muon Detector (CMU), the Central Muon Upgrade Detectors (CMP), the Central Muon Extension (CMX) and the Intermediate Muon detector (IMU). The $\eta - \phi$ coverage of the Run II muon detectors is shown in figure 3.13.

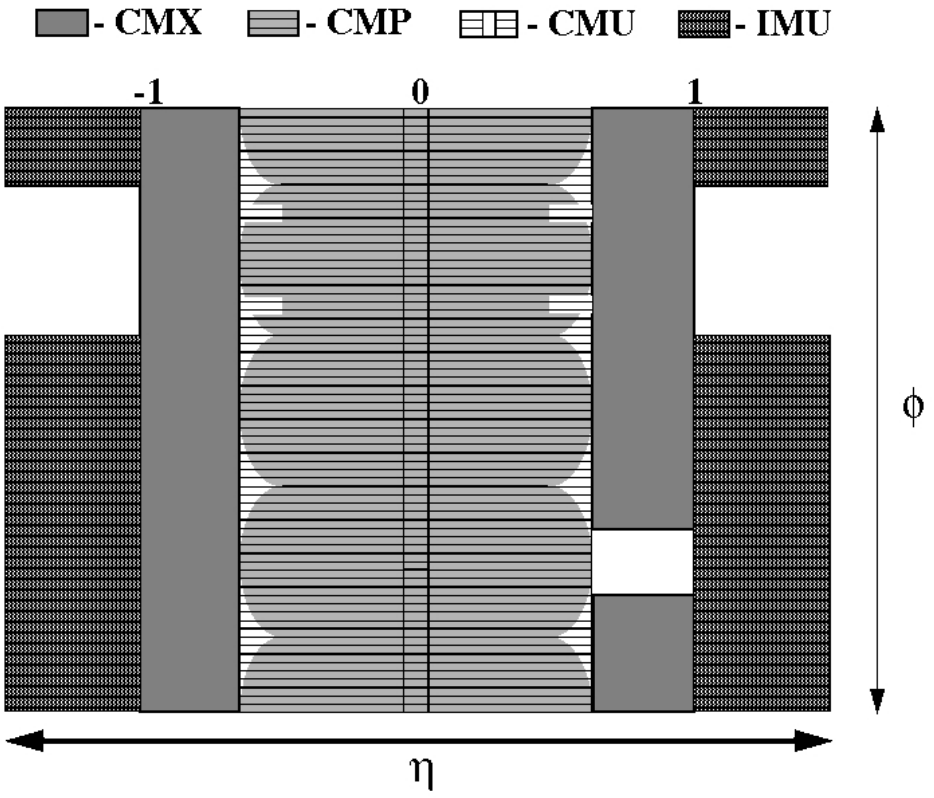

Figure 3.13: Coverage of muon detectors in the (η,ϕ) space.

Muon detectors share common features. They consist of stack of rectangular drift chamber modules[10] composed of single-wire cells. Stacks are four layers deep with laterally displaced cells from layer to layer to compensate for cell inefficiencies. The difference in drift-electrons arrival-times between neighbour cells provides a typical resolution of $250\ \mu m$ for the hit position in the transverse plane. Charge division at the wire ends measures the z coordinate with a $1.2\ mm$ resolution.
Chambers are coupled with scintillator counters in order to suppress backgrounds due to secondary interactions in the detector and cosmic rays.
A muon candidate is reconstructed when a short track segment (*stub*) in the muon chambers corresponds to the extrapolation of a COT track.

[10] Chambers are filled with a mixture of Argon and ethane (50% each).

The CMU detector is behind CHA at a radius of 347 cm from the beam axis and covers the $|\eta| < 0.6$ region. CMU consist of 144 modules with 16 cells each. The CMP detector is arranged to enclose the $|\eta| < 0.6$ region in an approximately central box (figure 3.13). Scintillator layers (CSP) on the outermost side of the CMP chambers allow identifying bunch crossing. CMU/CMP system is called CMUP. It detects muon with a minimum energy of $\sim$ 3 GeV.
The CMX detector extends the muon identification in $0.6 < |\eta| < 1$ region and is composed from different section of chambers. Two main *arches* were placed, since Run I, in both sides of the detector and cover the ϕ region $-45^\circ < \phi < 75^\circ$ and $105^\circ < \phi < 225^\circ$. The top *gap* in the west side ($\eta < 0$) of the detector[11], for $75^\circ < \phi < 105^\circ$, has been covered from Run II with a muon chamber system called *KeyStone*. As for CMP, cells of the two *arches* and of the *KeyStone* are sandwiched to scintillators (CSX). The bottom 90° gap of CMX penetrates the nominal floor of the collision hall but was filled in Run II with a slightly different muon chambers system[12], called *MiniSkirt*, for $-90^\circ < \phi < -45^\circ$ and $225^\circ < \phi < 270^\circ$. There is one layer of scintillator, MSX, installed in the inner side of the *MiniSkirt*, read by photomultiplier at both ends.
The fordward region of muon system is the IMU detector, composed by the BMU muon chamber for $1 < |\eta| < 1.5$ and $-45^\circ < \phi < 225^\circ$ and the associated scintillator counters sub-systems called BSU(Barrel Scintillator Upgrade) and TSU(Toroid Scintillator Upgrade).

3.7 Trigger system

At Tevatron Run II the interaction rate is of the order of MHz, which is much higher than any possible event recording rate (order of 100 Hz).
However, $p\overline{p}$ interactions are mostly inelastic, elastic and diffractive with no significant momentum transfer. More interesting events have cross-sections from 10^3 to 10^{12} times smaller than inclusive $p\overline{p}$ cross section [13].
The identification of the interesting events is accomplished by dedicated fast online electronics, called the Trigger System, which evaluates the information from the detector in real time. The trigger system (see figure 3.14) is a three-tier system, where each level of electronics performs a slower but more accurate event reconstruction and filter with increasing trigger level according to a set of predefined conditions.

Level 1 The level 1 (L1) is a synchronous pipeline system where up to 42 subsequent events can be stored for $\sim$5.5 μs while the hardware is taking a decision. If no acceptance decision is made up to that time the event is lost[14]. L1 decision are made in average in about 4 μs: no dead time is expected from this level. L1 rejects $\sim$ 97% of the events and typical output rate is $\sim$50 kHz.
The L1 decision is generated by:

- XFT (extremely fast tracker), which reconstructs approximate tracks ($P_T \geq 1.5GeV$) in

[11] The same coverage was not possible in the east side ($\eta > 0$) because of the presence of cryogenic utilities servicing the solenoid.
[12] The design and chamber geometry for this section is similar but different from the upper part of the detector. The geometry is a plane of chambers arranged in a pin-wheel shape - a flattened cone.
[13] For example $\sigma_{p\overline{p}\to t\overline{t}} \approx 7\ pb$.
[14] In order to be as fast as needed by the no dead-time condition L1 is completely built on a set of custom boards.

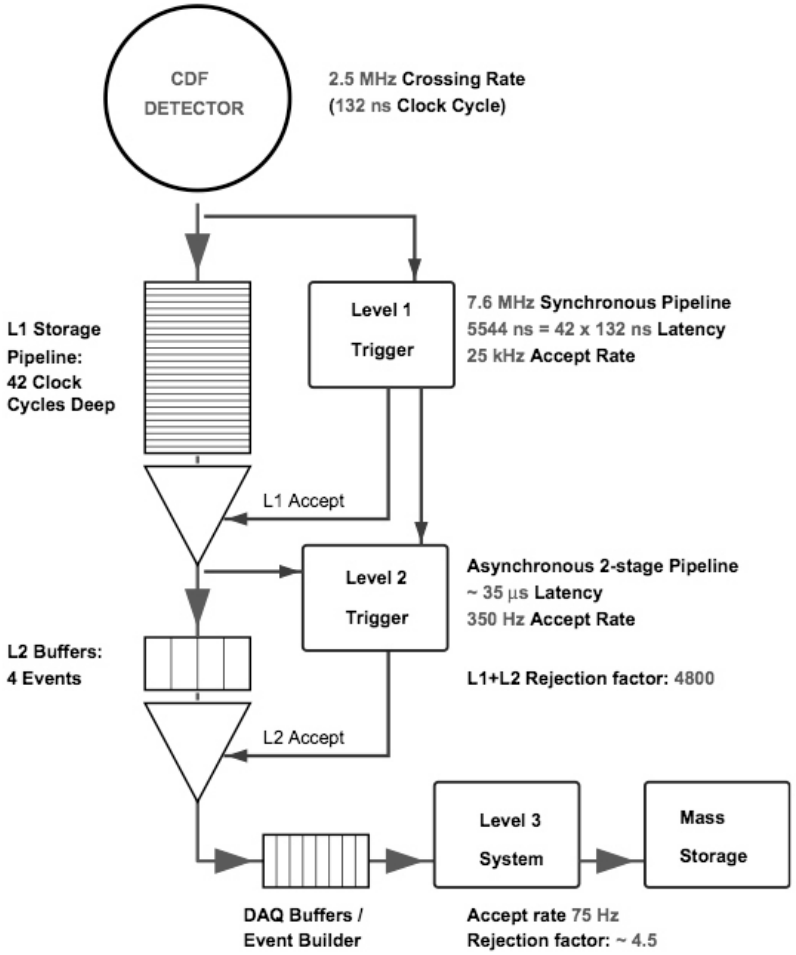

Figure 3.14: CDF trigger block diagram.

the transverse plane by exploiting information from COT superlayers[15]. These tracks can be propagated to the calorimeter and to the muon chambers to contribute to higher trigger levels.

- the calorimeter trigger, which indicates large energy releases in the electromagnetic or hadronic cells (these can be seed for electrons or jets identification).
- the muon trigger, which matches XFT tracks to stubs in the muon chambers.

Level 2 Events accepted at level 1 (L1) are sent to 4 asynchronous buffers at level 2 (L2). Buffers are used to store events until a decision is made. Because of the limited size of the buffers deadtime may occur. L2 purposes are:

- to add the energy deposited in the towers in small regions around L1 seeds, as an approximate measure of an electron or jet energy.

[15] It searches the 4 axial SL for track segments, then the Linker Board tries to link together at least three of them.

- to use calorimeter and CES to improve separation of $e^{\pm}$ from γ.
- to reconstruct a full COT track and associate it to an outer muon stub in order to improve muon signature.
- to indicate tracks with a large impact parameter by means of Silicon Vertex Trigger (SVT) on which to trigger on secondary vertexes from decay of long-lived heavy flavour hadrons.

L2 acceptance rate is ∼300 Hz (rejection factor ∼150). The block diagram of L1 and L2 with the involved subdetectors is schematized in Fig. 3.15.

Level 3 Level 3 (L3) is a software trigger. L3 addresses event objects delivered by L2 to the Event Builder (EVB), which reconstructs the entire event with the same accuracy as in the offline analysis. The final decision to accept an event is made on the basis of a list of observables indicating candidate events of physical interest (top production events, W/Z events, Drell-Yan events, etc.).
Accepted events exit L3 at a rate of up to 100 Hz and are permanently stored on tapes.

To collect as many data as possible was introduced the use of *prescaled* trigger. A trigger path is said to be prescaled by a factor N if it is configured to accept only one event each N events that pass the three trigger levels. Prescaling trigger is useful in CDF data taking because it is *dynamically* implemented. During a data capture the luminosity decreases as time passes, and consequently decreases the rate at which events pass a given trigger path. To improve at best the data-taking the prescale factor (N) of a trigger decreases proportionally to the rate of triggered events, so as the number of recorded events is constant. Using this *dynamic prescaling* (DPS) the acquiring time is exploited at most.

3.8 Single Lepton triggers

The data used in the $ZZ \to lll'l'$ search has been collected using one high E_T electron trigger and three high p_T muon triggers, that feed the CDF standard BHEL and BHMU datasets, respectively. It is required that all Data events fire one of the following *trigger paths*

- ELECTRON_CENTRAL18
- MUON_CMX18
- MUON_CMUP18
- MUON_CMP18_PHIGAP

that consist of different set of requirements at each trigger level (see Sec. 3.7). In the following are described the different request for the triggers used.

- ELECTRON_CENTRAL_18
  - L1 - A central electron cluster with $E_T > 8$ GeV/c^2, $E_{HAD}/E_{EM} < 0.125$, and an associated $p_T > 8.34$ GeV/c XFT[16] track.
  - L2 - A central electron cluster with $E_T > 16$ GeV/c^2, $E_{HAD}/E_{EM} < 0.125$, and an associated $p_T > 8$ GeV/c XFT track.

[16] A COT tracking hardware for the trigger.

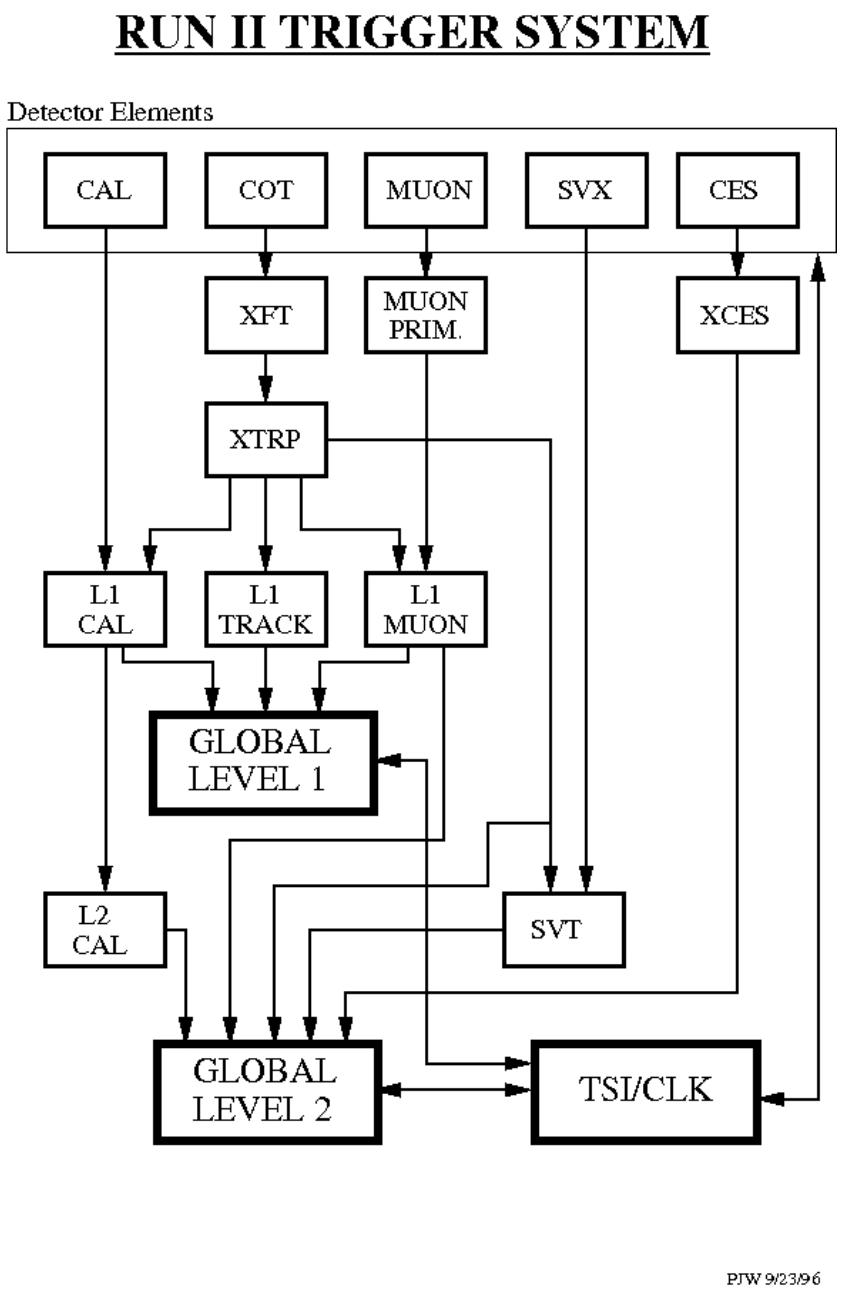

Figure 3.15: Block diagram of level 1 and level 2 triggers. The involved subdetectors are dedicated.

  - L3 - A central electron cluster with $E_T > 18$ GeV/c^2, $E_{HAD}/E_{EM} < 0.125$, $L_{SHR} < 0.4$, and an associated $p_T > 9$ GeV/c L3 track that extrapolates to the CES within 8 cm in z of the cluster position.The E_T calculation uses the track angle.

- MUON_CMUP18
  - L1 - An XFT track with $p_T > 4$ GeV/c associated with both a CMU and a CMP stub.

  - L2 - An XFT track with $p_T > 14.77$/c GeV associated with both a CMU and a CMP stub.
  - L3 - A minimum ionising track with $p_T > 18$ GeV/c associated with both a CMU and CMP stub, with $|\Delta X_{CMU}| < 20$ cm, $|\Delta X_{CMP}| < 10$ cm.

- MUON_CMX18
  - L1 - An XFT track with $p_T > 8.34$ GeV/c associated with a CMX stub and CSX scintillator information.
  - L2 - An XFT track with $p_T > 14.77$ GeV/c associated with a CMX stub.
  - L3 - A minimum ionising track with $p_T > 18$ GeV/c associated with a CMX stub with $|\Delta X_{CMX}| < 10$ cm.

- MUON_CMP18_PHIGAP
  - L1 - An XFT track with $p_T > 4$ GeV/c associated with a CMP stub but NOT a CMU stub.
  - L2 - An XFT track with $p_T > 14.77$/c GeV associated with a CMP stub but NOT a CMU stub.
  - L3 - A minimum ionising track with $p_T > 18$ GeV/c associated with a CMP stub but NOT a CMU stub, with $|\Delta X_{CMP}| < 10$ cm.

From Period 9 (Sept. 2006), alternate paths with various combinations of prescales and luminosity-enables were introduced to control the muon trigger rates at high instantaneous luminosity. In this analysis we use the trigger paths that provide the largest integrated luminosity for a given run range.

Chapter 4

Physical Object Reconstruction

Contents

All the data collected from the CDF detector are at the origin simply electronic signal recorder from the hardware components of the detector. A hard but fundamental effort is necessary to convert them in physical information. In the following sections are described the techniques combined to reconstruct physical objects in the detector.

4.1 Tracks Reconstruction

The ability to detect and reconstruct charged particle trajectories is essential for particle identification and momentum reconstruction. Precise, high efficient tracking plays a central role for particle identification and separation.
At CDF the following five parameters are used to describe the helix trajectory of a charged particle in the magnetic field $\overrightarrow{B}$ (see Figure 4.1):

- C: the half-curvature (C $= 1/2r$, where r is the helix radius) of the trajectory, it has the same sign of the particle charge and it is related to the transverse momentum of the track:

$$p_T = \frac{B \cdot q}{2|C|} \tag{4.1}$$

being q the charge of the particle and B the magnetic field.

- d_0: the impact parameter, i.e. the distance of the closest approach in the transverse plane between the helix and the beam line (z-axis), defined as:

$$|d_0| = \sqrt{x_0^2 + y_0^2} - r \tag{4.2}$$

where x_0 and y_0 are the coordinate of the track, in the transverse plane, in the point of closest approach to the beam line. With the *impact parameter significance*, defined as $|d_0/\sigma_{d_0}|$, is possible to estimate if the particle comes from primary vertex,$d_0 \approx 0$, or from a secondary one.

- λ: the helix pitch, i.e. the cotangent of the polar angle between the track and the z-axis (cotθ_0). The longitudinal component of the momentum is given by:

$$p_z = p_T \cdot cot\ \theta_0\ . \tag{4.3}$$

- z_0: the position of the track vertex in z, defined as the interception between the track and the z axis in the transverse plane.

- ϕ_0: the azimuthal angle of the track at its vertex.

The Helix is completely described by these five parameters, in fact every point along the trajectory satisfy the following equation [23]:

$$x = r \sin\phi - (r - d_0)\sin\phi, \tag{4.4}$$
$$y = r \cos\phi - (r - d_0)\cos\phi, \tag{4.5}$$
$$z = z_0 + s\lambda. \tag{4.6}$$

where s is the length projected along the track, and $\phi = 2Cs\ +\ \phi_0$.

4.1.1 Tracking Algorithms

A track pattern recognition algorithm search among the several signals (*hits)*) in the tracking system those that can be associated with the same track. Then a track fitting algorithm use those hits to reconstruct a track with its parameters. The experiment exploits several tracking algorithms (reference), each optimised for the information available in different detector region. In the following paragraphs we describe the main features of the four tracking algorithms most used: the Outside-In algorithm (OI), the Silicon-Stand-Alone (SiSA) algorithm and the Inside-Out (IO) algorithm.

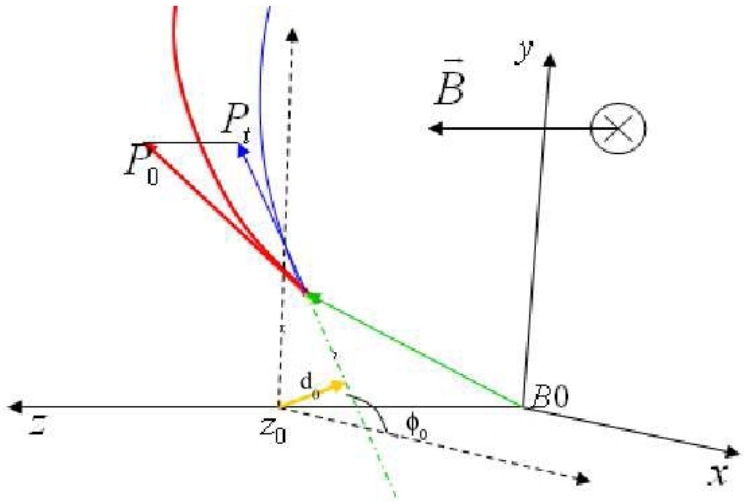

Figure 4.1: CDF track parameters and coordinate system.

Outside-In Algorithm

The Outside-In is the most used CDF tracking algorithms and it is based on COT hits. Track pattern recognition starts in the COT outer layers, where the hit density is smaller, and proceeds through four steps: first each superlayer is searched for groups of three aligned hits and they are fit to a straight line with the least squares method. Then the tracks are reconstructed using information of the *axial* superlayers that are linked by two different algorithms (*segment linking* and *histogram linking* algorithms [24]). During the third step, the information of the stereo layers are added and the algorithm searches for the vertex of the track. As final step a global refit of the track is performed taking into account corrections for the non-uniformity of the magnetic field and for the modelling of electron drift.
At second stage of reconstruction, the track found in the COT is propagated into the silicon system. A road around a track is defined using the errors on the COT track parameters and silicon hits are added if they lie inside this predefined road. When a hit is added, the track parameters are recalculated and the search is performed again. The impact parameter resolution of COT+SVX tracks is found to be $\sigma_{d_0} \simeq 20\ \mu m$.

Silicon-Stand-Alone Algorithm

The hits in silicon subdetectors not used by OI tracking are available to the Silicon-Stand-Alone algorithm [24] to search for tracks in the region $|\eta| < 2$ with few residual capability up to $|\eta| \simeq 2.8$. The SiSA algorithm starts from a collection of at least four hits in the SVXII detector in the $r - \phi$ plane and fits the C, d_0 and λ parameters to obtain a projection of the helix on the transverse plane. Then the algorithm creates a 3-D seed track adding small angle hits and the primary vertex information. At this point the 90° stereo hits are added and a global refit is performed.
SiSA tracks reconstructed only with SVXII have a poor resolution for high p_T tracks so hits are searched in $L00$ and ISL with the SVXII track as seed. The track is refit if other layers can be added. However, the performances on momentum and impact parameter resolution are limited and indeed SiSA tracks are not used for secondary vertexing.

Inside-Out Algorithm

The third tracking algorithm, the Inside-Out [25], tries to recover efficiency and p_T resolution in the region $1.2 < |\eta| < 1.8$ where the COT coverage is limited. Practically SiSA tracks are used as seed which are extrapolated to the COT inner cylinder. Matching hits in the COT are added, track is refitted and all duplicates are removed.

4.2 Primary Vertex Identification

The primary vertex is the position of the interaction point of a given event. The algorithm uses tracks information (`PrimVtx`): a seed vertex is calculated as the average z position of all tracks passing predefined quality requirements and is provided as input. Then all tracks with $|z_0 - z_{vtx}| < 1\ cm$, $|d_0| < 1\ cm$ and $|d_0/\sigma_{d_0}| < 3$ are selected and ordered in decreasing p_T. They are fitted to a new vertex and the tracks with $\chi^2 > 10$ are removed. The procedure is iterated until all accepted track have $\chi^2 < 10$. A quality index is assigned to the primary vertex depending on parameters like the number of final tracks. Precise determination of the primary vertex is important to individuate displaced secondary vertices and to properly correct jets energy.

4.3 Electron Identification

The CDF EM clustering algorithm [26] works in a simple but efficient way. The physical space corresponding to the calorimeter towers is mapped in an $\eta - \phi$ plane, the algorithm creates two lists of the calorimeter towers ordered by decreasing energy revealed on them: the *usable list* (working towers with energy > 100 MeV) and the *seed list* (towers with energy > 2 GeV). It then takes the first seed tower and create an $\eta - \phi$ cluster by adding the neighboring towers to form a 2×2 or 3×3 $\eta - \phi$ area.
As final step the $\eta - \phi$ centroid of the cluster is calculated and the used towers are removed from the lists. The algorithm selects the next seed tower and iterate the process until all the seed towers have been used.
Usually 3×3 clustering is used in the CEM region while 2×2 clusters are used in the PEM region, this reduces the probability to overlap the clusters of two different electrons. A cluster is not allowed to cross the boundary between different subdetectors. Several corrections are applied to reconstruct the initial energy of the EM object. The clusters are corrected for lateral leakage, location inside the physical tower, on-line calibration and response curve drawn by test beam data. Also the energy measured in the shower max (PES) and pre-shower (PPR) detectors is added to the final reconstructed energy. PES is also used to compare the shower profile of electrons or photons and it is used to measure the spatial position of the EM shower centroid.
Beyond the raw EM energy measurement, the calorimeter information can be further exploited for a better particle identification. The E_{Had}/E_{EM} ratio is used to identify electrons, in fact studies performed with candidate $Z^0 \to e^+e^-$ events [27] show that electrons detected in the central or in the plug region have a little deposit in the hadronic part of the calorimeter (see Fig. 4.2) and cutting $E_{Had}/E_{EM} < 0.12$ clean the $e^{\pm}$ signal.

The *IsoRel* (or isolation) is another quantity derived from calorimeters. It is defined as:

$$\textit{IsoRel} \equiv E_T^{iso}/E_T^{cluster},$$

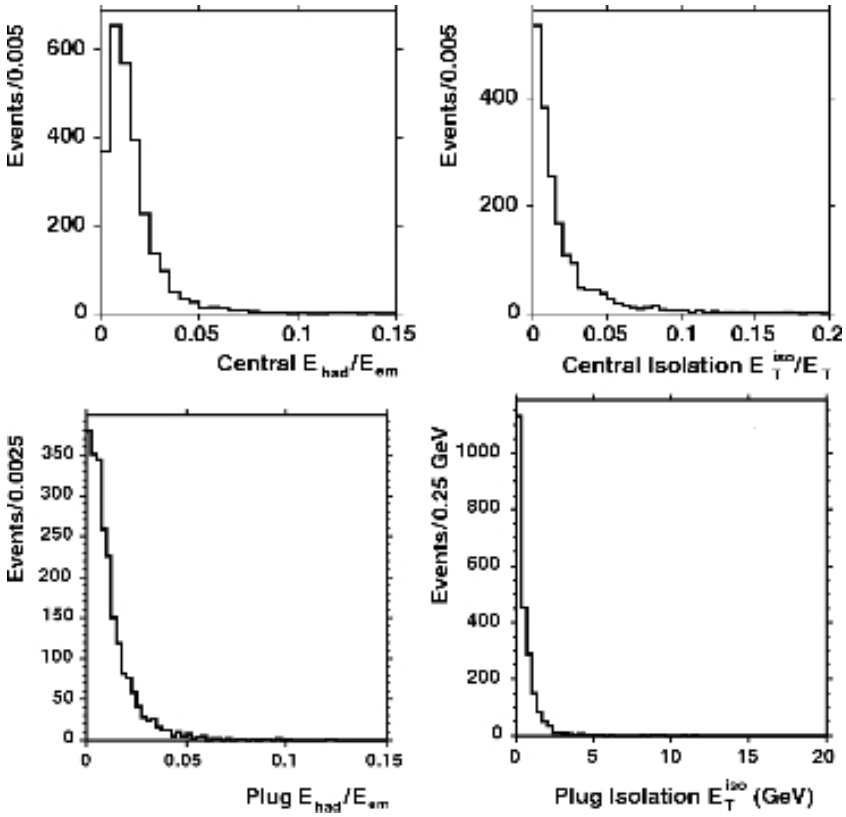

Figure 4.2: E_{Had}/E_{EM} (left) and isolation (right) distribution of central (top) and plug (bottom) calorimeter electron selection from unbiased, second legs of $Z^0 \rightarrow e^+e^-$ candidate events in Data [27].

where $E_T^{iso} = E_T^{0.4} - E_T^{cluster}$ and $E_T^{0.4}$ is the energy collected by the calorimeter within a radius $\Delta R = 0.4$ from the centroid of the EM cluster. Isolation is used in analyses involving a $W^{\pm}$ or Z^0 boson with a cut $IsoRel < 0.1$, in fact the kinematic region allowed to leptons coming from the bosons decay is usually far from jets or other particles (see Fig. 4.2).
After the electromagnetic cluster reconstruction a track is searched to be associated to it to obtain the complete electron reconstruction. Then additional cuts are used for a better electron identification, like the $E^{cluster}/p^{track}$ ratio. The E/p distribution is peaked to 1 but it has large radiative tails because the electron can radiate bremsstrahlung collinear photons in the passage through the tracking volume. The EM energy measure is not much influenced by this[1], but the momentum measure decreases.

4.4 Muon Identification

While electrons and hadrons lose all of their energy and stop in the calorimeter section of the detector muons at CDF behave like *minimum ionising particles* (m.i.p.) and, since the leave just a very small amount of energy along their path, are the only particles that reach the outer part of the

[1] The photon generally deposits energy in the same EM cluster.

detector, where muon chambers are located. An algorithm fit the hits produced by the muon to a track segment which is called *stub*. The complete identification of a muon is composed by three pieces: a charged-particle track reconstructed by the tracking algorithm that points to a detected stub in a muon chamber plus the request of a m.i.p. in the calorimeters. To gain acceptance for the region not covered by chambers, some *stubless* muon categories have been defined based simply on the charged tracks and the m.i.p. request in the calorimeter, the so-called *CMIO* muons[2].

4.5 Neutrinos Identification

Momentum conservation is the only way to reveal the presence of neutrinos since they do not interact inside the detector components. Although it is impossible to know the exact momentum of the colliding partons, the transverse component, p_T, is approximately zero in the detector frame. All the detected transverse energies are vectorially summed, and if the sum is greater than zero, we assume that a candidate neutrino is revealed. The missing transverse energy $\not\!\!E_T$ gives a measure of the neutrino transverse momentum,

$$\vec{\not\!\!E}_T \equiv -\sum_i \vec{E}_T^i \tag{4.7}$$

where $\vec{E}_T^i$ is a vector with magnitude equal to the transverse energy collected by the $i-th$ calorimeter tower and pointing from the interaction vertex to the centre of the tower. The sum involves all the towers with total energy above 0.1 GeV in the region $|\eta| < 3.6$. At offline level, the algorithm corrects for the position of the reconstructed event vertex and for any reconstructed muon (their energy is calculated using track information).
The $\not\!\!E_T$used to identify neutrino has to be corrected for several effects. The largest correction is due to muons which are minimum ionising particles and do not leave much energy in the calorimeter causing an apparent missing energy as most of their energy is carried away as they leave the detector. The $\not\!\!E_T$ is corrected for muons identified according to section 4.7.2 by adding back their track momentum measurement and subtracting any small amount of energy which they may have deposited in the calorimeters. High-P_T tracks, supposed to be leptons that fall in an uninstrumented part of the detector, are treated the same as muons in this calculation since they enter a crack in the calorimeter and did not release their energy in it. The $\not\!\!E_T$ is also modified to account for the corrections to raw jet energies discussed in section 4.6. The $\not\!\!E_T$ used at the analysis level is then

$$-\vec{\not\!\!E}_T = \sum_i \vec{E}_T^i + \sum_\mu \vec{P}_T^\mu - \sum_\mu \vec{E}_T^\mu(Em + Had) + \sum_j \vec{E}_T^j(jet\ correction) \tag{4.8}$$

where the E_T have been corrected for the actual interaction z_0 point since the transverse components are calculated according to $\sin\theta$ and vertex away from $z = 0$ would give a different θ.
Beyond the neutrinos created in weak interactions there are also several sources of false $\not\!\!E_T$ which are often difficult to control. These sources include the mismeasurement of jet and lepton energies as well as when a lepton or a photon enters a crack in the detector where it would not be possible to reconstruct its energy with any reasonable accuracy.

[2] In such muon identification criteria there is more probability to have different object mis-identified as muons.

4.6 Jet Identification

QCD tells us that the parton composing the (anti)proton can be treated perturbatively as free particle if they are stuck by an external probe[3] with sufficient high energy (*hard scattering*). However partons resulting from the interaction can not exist as free particles because at longer distances (i.e. lower energies) the *strong potential* can not be treated perturbatively and partons must form colorless hadrons. This process is called *hadronization* or *showering* and produces a collimated cluster of stable particles named *jet*. A jet approximately retains the total momentum and direction of the initial parton (see Fig. 4.3).

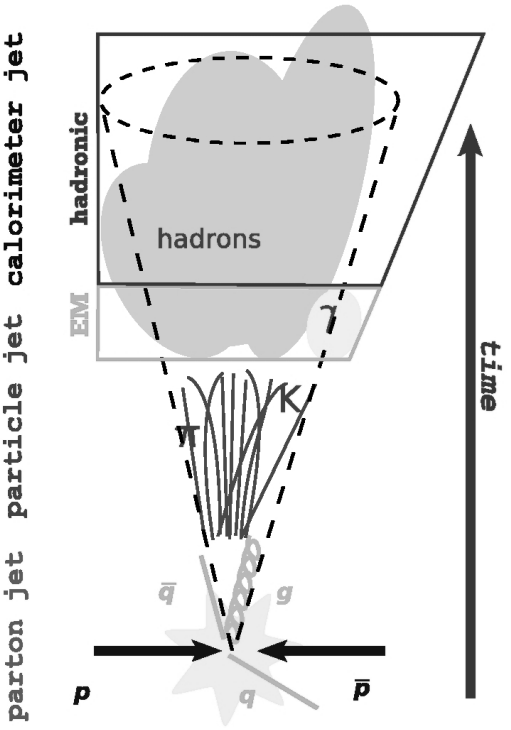

Figure 4.3: A parton originated from a hard scattering hadronizes and gives origin to a collimated spray of particles, a jet.

From the experimental point of view a jet is defined as a large energy deposit in a localised area of the detector (see Fig. 4.4). The challenge of a physics analysis is to recover from the detector information the initial energy, momentum and , possibly, the kind of parton produced in the original interaction. A "jet algorithm" is a tool to reconstruct such information and it must satisfy at best the following requirements [28]:

- *Infrared safety*: the presence of soft radiation between two jets may cause a merging of the two jets. This should not occur to avoid an uncorrected parton attribution.

[3] I.e. a lepton or a parton from another hadron.

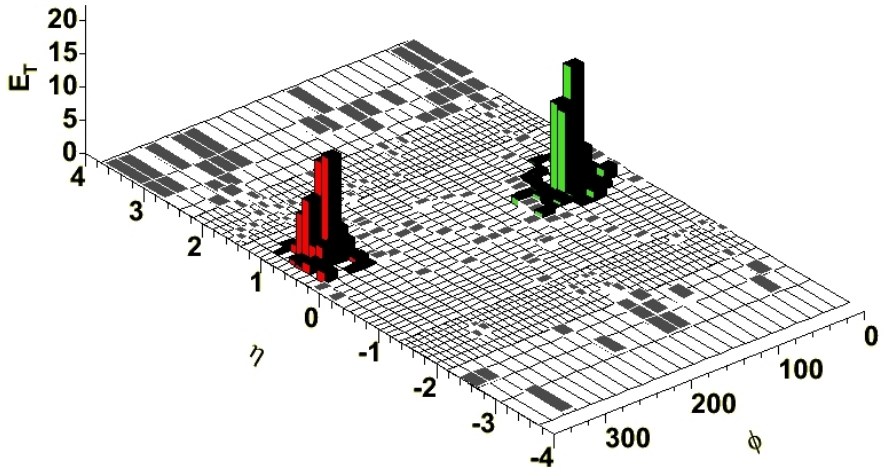

Figure 4.4: Calorimeter deposit in the $\eta - \phi$ plane as represented in the CDF event display. EM deposits are green while HAD deposits are RED.

- *Collinear safety*: the jet reconstruction should be independent from any collinear radiation in the event, i.e. different energy distribution of particles inside calorimetric towers.
- *Invariance under boost*: the same jets should be found independently from boosts in longitudinal direction.
- *Boundary stability*: kinematic variables should be independent from the details of the final state.
- *Order independence*: the same reconstructed quantities should appear looking at parton, particle and detector levels.
- *Straightforward implementation*: algorithm should be easy to implement in perturbative calculations.

Beyond this theoretical aspects a jet algorithm should be experimentally efficient with a high reconstruction efficiency, good resolution and stable at different luminosity.
Even though this analysis consider the fully leptonic decay of Z^0 boson the knowledge of jets reconstruction is relevant since the main background studied is due to the presence of jets misreconstructed as leptons.
In this analysis a jet is defined as a calorimeter cluster of size $\Delta R < 0.4$ which has a total corrected transverse energy of $E_T > 15$ GeV and that is within a pseudo-rapidity of $|\eta| < 2.5$. Identified electrons will always satisfy the jet requirements and for this reason an object is not counted as a jet if it is within $\Delta R < 0.4$ of an already identified electron.

4.6.1 CDF Cone Algorithm

CDF uses several algorithms, none of them really satisfying all the above requirements. The most common one is JETCLU[29], an iterative fixed cone jet reconstruction algorithm based only on calorimetric information.
The algorithm begins by creating a list of seed towers from all the calorimeter towers with transverse energy above the threshold of 1 GeV. Starting with the highest-E_T seed tower, a precluster is formed by combining together all adjacent seed towers within a cone of given radius R [4]. This procedure is repeated, starting with the next unused seed tower, until the list is exhausted. The E_T-weighted centroid is then formed from the towers in the precluster and a new cone of radius R is formed around this centroid. All towers with energy above the lower threshold of 100 MeV within this new cone are added to the cluster. Then, a new centroid is calculated from the set of towers within the cluster and a new cone drawn. This process is iterated until the centroid of the energy deposition within the cone is aligned with geometric axis of the cone (*stable solution*).
Since each tower may belong to only one jet, in case of jet overlap two clusters are merged if the total energy of the overlapping towers is greater than 75% of the energy of the smaller cluster. If the shared energy is below this cut, the shared towers are assigned to the cluster that is closer in $\eta - \phi$ space. This process is iterated again until the list of clusters remains fixed.
Massless four-vector momenta are assigned to the towers in the clusters for EM and HAD components with a magnitude equal to the energy deposited in the tower and the direction defined by a unit vector pointing from the event vertex to the centre of the calorimeter tower at depth that corresponds to the shower maximum. A cluster four-vector is then defined summing over the towers in the cluster:

$$E = \sum_{i=1}^{N} (E_i^{EM} + E_i^{HAD}) \tag{4.9}$$

$$p_x = \sum_{i=1}^{N} (E_i^{EM} \sin\theta_i^{EM} \cos\phi_i^{EM} + E_i^{HAD} \sin\theta_i^{HAD} \cos\phi_i^{HAD}) \tag{4.10}$$

$$p_y = \sum_{i=1}^{N} (E_i^{EM} \sin\theta_i^{EM} \sin\phi_i^{EM} + E_i^{HAD} \sin\theta_i^{HAD} \sin\phi_i^{HAD}) \tag{4.11}$$

$$p_z = \sum_{i=1}^{N} (E_i^{EM} \cos\theta_i^{EM} + E_i^{HAD} \cos\theta_i^{HAD}) \tag{4.12}$$

where the index i runs over the towers in the cluster. Other variables are added to the final jet-object used in the analysis: E_T, η and ϕ (calculated from the jet vertex with an energy weighted average over the calorimeter towers associated with the cluster) or other useful information like the number of tracks reconstructed inside the jet cone, the vertex quality or the energy deposited in the HAD or EM calorimeter.

4.6.2 Jet Correction

The ultimate goal of the jet reconstruction algorithm is the best determination of the energy of the outgoing partons coming from the hard interaction. Clearly many factors produce a mismatch

[4] CDF reconstructs jets using radii 0.4, 0.7 and 1.0.

between the raw energy produced by the experimental algorithm and the one of the partons before the hadronization.
CDF developed a set of jet energy correction depending of η, E_T^{raw} and R of the jet reconstructed by JETCLU algorithm. The corrections are divided into five levels[5] ("L-levels") so that can be applied in a standard way to different analysis [30]: η-dependent response of the calorimeter ($L1$), effect of multiple interactions ($L4$), absolute energy scale ($L5$), underlying event ($L6$) and out-of-cone ($L7$) corrections. The correction $L1$ and $L5$ are multiplicative factors (f_{L1} andf_{L5}) on the raw E_T of the jet, the others are additive constants (A_{L4},A_{L6} and A_{L7}). The general equation to apply all corrections is:

$$E_T^{corr}(\eta, E_T^{raw}, R) = (E_T^{raw} f_{L1} - A_{L4}) f_{L5} - A_{L6} + A_{L7}. \quad (4.13)$$

A more detailed description of the different level algorithm can be found in [31] and will not be discussed here.

4.7 High-P_T Object Identification

Two lepton flavours (e and μ) are considered in this analysis. Electron and muons are categorised by how they are reconstructed in the CDF II detector. There are 11 non-overlapping categories in total. These have been defined by the CDF diboson working group that search for WW, WZ and ZZ production. The categories are listed here and they will be described later in sections 4.7.1, 4.7.2 and 4.7.3.

TCE Tight Central Electron: $|\eta| < 1.1$.

LCE Loose Central Electron

PHX Fordward electron which relies on silicon tracking: $1.2 < |\eta| < 2.0$.

CMUP Central Muon which has hits in both the CMU and CMP muon detectors: $|\eta| < 0.6$.

CMP Central Muon which has hits in CMP but NOT in CMU muon detector: $|\eta| < 0.6$.

CMX Muon which has hits in the CMX detector in the main arches: $0.65 < |\eta| < 1.0$.

MsKs New CMX categories of muons with hits in the MiniSkirt or KeyStone part of the detector(see Sec. 3.6).

BMU Fordward Muon with a silicon tracks and hits in IMU: $1.1 < |\eta| < 1.2$.

CMIOCES Muon which does not satisfy the hit requirements of CMUP or CMX but is fully fiducial to the central calorimeter.

CMIOPES Similar to CMIOCES but in the fordward region.

CrkTrk High-P_T track which pointed to a crack in the detector. It is assumed to be either an electron or a muon.

[5] The actual naming skips $L2$, because it is absorbed in $L1$, and $L3$, as it was introduced as a temporary MC calibration in Run II.

To ensure the uniqueness of each lepton category we require that the extrapolation of the muon or electron track hits the surface of the corresponding muon detector or calorimeter sector. Moreover we explicitly veto that a stubless muon has already been identified as a stubbed one. This requirement is usually called *fiduciality*.

4.7.1 Electron Identification

As described in Section 4.3 $e^{\pm}$ are reconstructed starting from an electromagnetic calorimeter cluster and a charged track associated. Then cuts are applied to improve electron reconstruction in the different part of the detector. In this analysis electrons are identified in both the central ($|\eta| < 1.1$) and forward ($1.1 < |\eta| < 2.0$) regions. Tables 4.1, 4.2 and 4.3 give the specific quantitative values for the parameters used to select Tight Central Electrons (TCE), Loose Central Electron (LCE) and forward (PHX) electrons. The two Central Electron categories are differentiated by some removed cuts for LCE respect to TCE. PHX electrons are named after the PHOENIX algorithm was used to identify forward electrons by matching plug EM calorimeter information to SVX hits. A trigger path, MET_PEM, is also associated with this electron category, based on a combined request of plug calorimeter energy tower and a large $\not\!\!E_T$. The meanings of identification variables are give below.

Central Electrons (TCE)	
Region	Central ($\|\eta\| < 1.1$)
Fiducial	Track fiducial to CES
Track P_T	$\geq$ 10 or $\geq$ 5 if $E_T < 20$ (GeV)
Track $\|z_0\|$	$\leq$ 60 cm
# Axial SL	≥ 3 with ≥ 5 hits
# Stereo SL	≥ 2 with ≥ 5 hits
Conversion Flag	$\neq 1$
Isolation/E_T	≤ 0.1
E_{HAD}/E_{EM}	$< 0.055 + 0.00045 \cdot E$
L_{shr}	≤ 0.2
E/P	$< 2.5 + 0.015 \cdot E_t$
CES ΔX	-3 $\leq$ q·$\Delta X \leq$ 1.5
CES ΔZ	$<$ 3 cm

Table 4.1: Tight Central (TCE) electron identification requirements.

- Region: A flag indicating if the track is fiducial to the central or plug calorimeters. This flag comes from the FidEle routine in CDF offline software.
- Fiducial: In the case of TCE and LCE the track must be fiducial to the CES.
- Track p_T: The transverse component of the momentum which is measured explicitly using the track curvature.
- Track z_0: The longitudinal (z) position of the track where it intersects the beamline

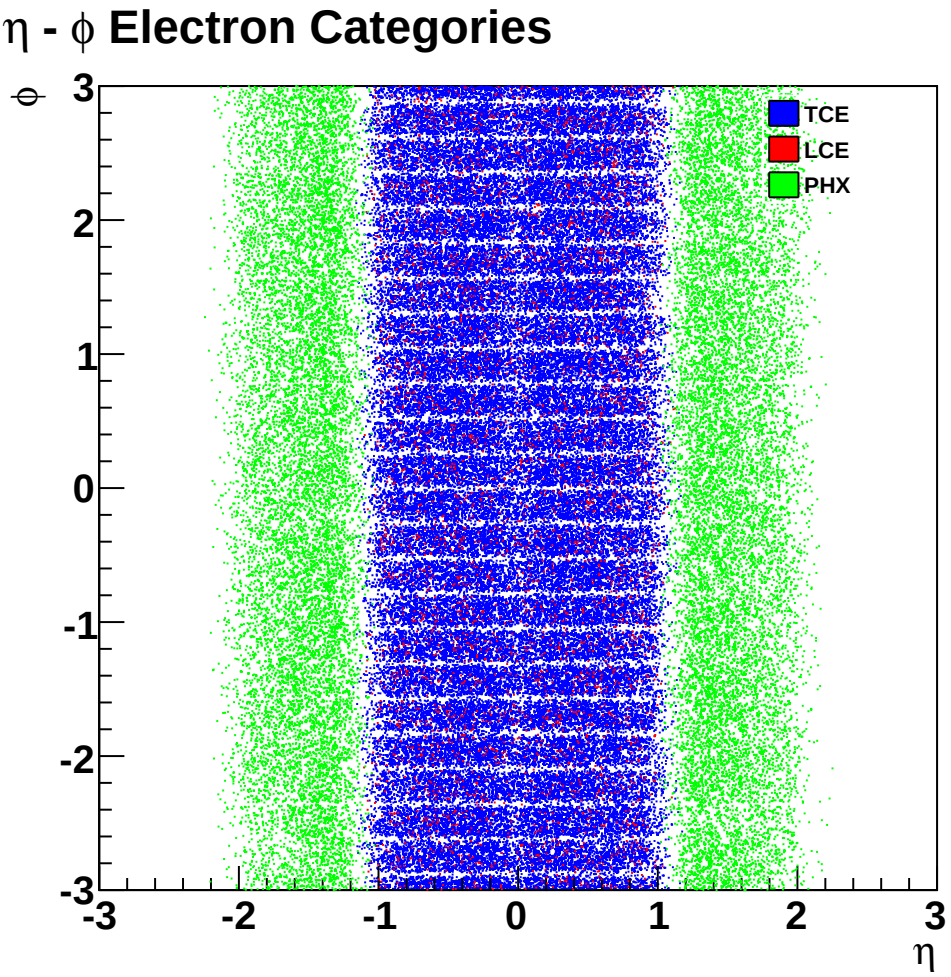

Figure 4.5: Distribution of different electron types in $\eta - \phi$ plane.

- Axial and Stereo SL: The number of axial and stereo superlayers in the COT which have at least 5 hits associated with this track.
- Conversion flag: A routine is implemented to identify electrons which may have come from photon conversion. These electron candidates have their conversion flag set to one and rejected.
- Isolation $/E_T$: The energy deposited in the calorimeter in a cone of radius $\Delta R \leq 0.4$ around the electron cluster excluding the energy of the electron cluster divided by the E_T (p_T) of the electron candidate.
- E_{HAD}/E_{EM}: The ratio of energy which is deposited in the hadronic (CHA or WHA) portion of the calorimeter to the energy deposited in the electromagnetic (CEM or PEM) portion of the calorimeter.

LCE	
Region	Central ($\|\eta\| < 1.1$)
Fiducial	Track fiducial to CES
Track P_T	$\geq$ 10 or $\geq$ 5 if $E_T < 20$ (GeV)
Track $\|z_0\|$	$\leq$ 60 cm
# Axial SL	≥ 3 with ≥ 5 hits
# Stereo SL	≥ 2 with ≥ 5 hits
Conversion Flag	$\neq 1$
Isolation/E_T	≤ 0.1
E_{HAD}/E_{EM}	$< 0.055 + 0.00045 \cdot E$

Table 4.2: Loose Central (LCE) electron identification requirements.

Forward Electrons (PHX)	
Region	Plug ($1.1 < \|\eta\| < 2.0$)
E_{HAD}/E_{EM}	< 0.05
PEM 3×3 Fit	true
χ^2_{PES}	$\leq$ 10
PES 5×9 U	$\geq$ 0.65
PES 5×9 V	$\geq$ 0.65
Isolation/E_T	$\leq$ 0.1
ΔR(PES,PEM)	$\leq$ 0.3
Track matched	true
# of Silicon hits	$\geq$ 3
Track $\|z_0\|$	$\leq$ 60 cm

Table 4.3: Forward (PHX) electron identification requirements.

- L_{shr}: A variable that compares the lateral shower profile in towers next to the seed tower to an expected profile given by

$$L_{shr} = 0.14 \, \frac{\sum_i (M_i - P_i)}{\sqrt{(0.14\sqrt{E_{EM}})^2 + \sum_i (\Delta P_i)^2}} \tag{4.14}$$

  where i denotes the adjacent towers, M_i the measured energy, and P_i the predicted energy in the ith tower.

- E/P: The ratio of the energy measured in the calorimeter to the momentum calculated from the measurement of the track curvature.

- CES ΔX: The difference in the $r - \phi$ plane between the best CES match and the COT beam-constrained track extrapolation to the CES.

- CEM ΔZ: The longitudinal difference between the best CES match and the COT track extrapolation to the CES.

- η_{PES}: The pseudo-rapidity as measured by the best matched PES cluster.
- PEM 3×3 Fit: A χ^2 fit to the electron test beam data of 9 PEM towers.
- χ^2_{PES}: A χ^2 fit to the electron test beam data for shower-maximum profile.
- PES 5×9 U/V: The ratio of the central 5 tower energy to the total 9 tower energy.
- ΔR (PES,PEM): The difference in the $r-\phi$ plane between the best PES match and the PEM measurement.
- Track Matched: PHX electrons must have a track that is matched to the PEM cluster and event vertex.
- # of Silicon hits: The number of the hits in the silicon detector associated with a specific track. The maximum number of hits is 8 (for L00, SVX and ISL combined).

4.7.2 Muon Identification

This analysis considers seven categories of muons: CMUP, CMP-*only*, CMX, CMX-MsKs, BMU, CMIOCES and CMIOPES. These types are essentially defined by the detectors which they pass through. The detectors have different components, geometry, location, and hence different detector efficiencies and resolution. Because of this the efficiencies are determined separately for each category, and these will be discussed in Section 4.7.4.
Some real muons may fall under the categorisation of CrkTrk which is discussed in section 4.7.3.
All muons must satisfy the base requirements listed in Table 4.4.

Base Muon Selection	
P_T	$>$ 10 GeV
E_{EM}	$<$2 + max(0,(p - 100)·0.0115)
E_{HAD}	$<$6 + max(0,(p - 100)·0.028)
Isolation/P_T	$\leq$ 0.1
# Axial SL	≥ 3 with ≥ 5 hits
# Stereo SL	≥ 2 with ≥ 5 hits
Track $\lvert z_0\rvert$	$<$ 60 cm
Track $\lvert d_0\rvert$	$<$ 0.2 cm ($<$ 0.02 cm with silicon)
χ^2/dof	$<$ 4.0 ($<$ 3.0 if Run $>$ 186598)

Table 4.4: Base identification requirements for all muon categories. NOTE: The # Axial SL and # Stereo SL are released for BMU muons.

Muons are further categorised by the fiduciality of the high-P_T track to the muon detectors (CMU and CMP in the case of CMUP and CMP-*only* muon, CMX in the case of a CMX or MsKs muon and IMU in the case of BMU muon). CMUP muons are required to have a stub in both CMU and CMP muon chambers while CMP-*only* muons are required to have a stub only in the CMP muon chambers and not in the CMU; using the CMP-*only* category we can gain acceptance on muons reduction by covering the ϕ gaps in the CMU muon chambers. CMU and CMP cover together a

pseudo-rapidity range $|\eta_{det}| < 0.68$. CMX and CMX-MsKs muons are required to have a stub in the CMX muon chambers system, the former has a fiduciality to the two main *arches* of the muon chambers, the latter has a fiduciality to two smaller part of the detector, the *Mini-skirt* and the *Key-stone*. The whole CMX muon detector has a pseudo-rapidity range coverage $0.65 < \eta_{det} < 1$. BMU muons are required to have a fiduciality to the IMU forward muon detector, sourrounding the plug calorimeter, for a coverage of $1 < \eta_{det} < 1.5$.
Trigger paths are associated with CMUP, CMP-*only* and CMX muons while BMU is not, at the moment, a triggerable category[6]. In cases where the track does not point to a reconstructed stub or is not fiducial to these muon detectors it is still possible to identify muon using a high-P_T track pointing to calorimeter energy deposit consistent with that of a minimum ionising particle, but without the additional muon stub information. As expected, the probability of another object faking such muons is larger than for the CMUP, CMX and BMU categories (see section 4.8). In these cases the track must be fiducial to the central (for the CMIOCES category) or forward (for the CMIOPES category) calorimeters.

CMUP Muon	
CMU Fid	$x_{fid} < 0$, $z_{fid} < 0$ cm
CMP Fid	$x_{fid} < 0$, $z_{fid} < 0$ cm
ΔX_{CMU}	$<$ 7 cm
ΔX_{CMP}	$<$ max(6.0,150.0/P_T) cm

Table 4.5: CMUP muons identification requirements.

CMP Muon	
CMP Fid	$x_{fid} < 0$, $z_{fid} < 0$ cm
CMU Fid	*false*
ΔX_{CMP}	$<$ max(6.0,150.0/P_T) cm
ϕ-gaps	ϕ (mod 15°) < 2 or ϕ (mod 15°) > 13
	No Bluebeam for run $\leq$ 154449
Good trigger	run $\geq$ 229764

Table 4.6: CMP-*only* muons identification requirements.

Additional requirements for the seven categorisation of muons are given in Tables 4.5 - 4.10 and described in the following.

- CM(U|P|X) x_{fid}, z_{fid}: The extrapolation of the track to the relevant muon detector is required to be fiducial to the detector and in the case of CMX must also not be within 3 cm in z_{fid} of the edge of the detector[7].

[6] The only trigger paths running currently associated with the IMU sector asks also for the presence of jets in the event, to reduce the high fake rate, or are designed to trigger on the hadronic τ decays.
[7] These coordinates refer to the face of the specific muon detector and not the CDF II coordinate system.

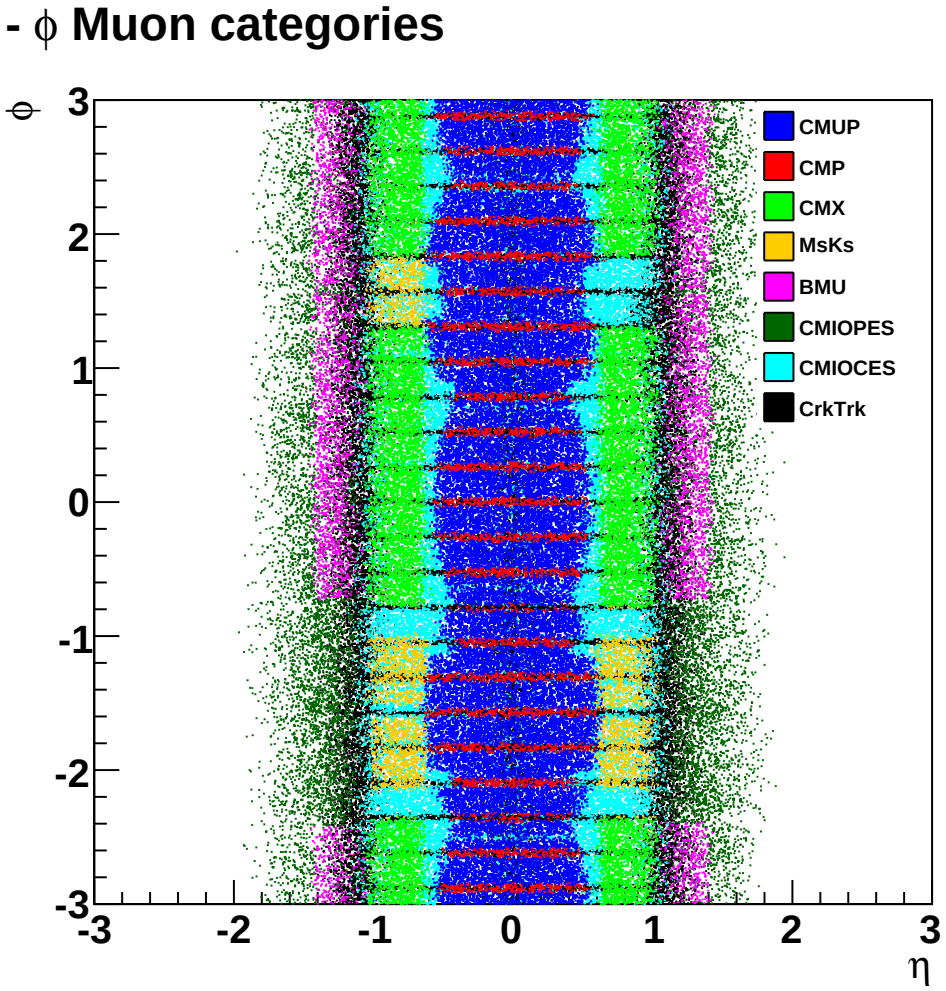

Figure 4.6: Distribution of different muon types in $\eta - \phi$ plane.

CMX & MsKs Muon	
CMX Fid	$x_{fid} < 0$, $z_{fid} < -3$ cm
ΔX_{CMX}	$<$ max(6,125/P_T) cm
ρ_{COT}	$>$ 140 cm

Table 4.7: CMX arches and Miniskirt-Keystone muons identification requirements.

- $\Delta X_{CM(U|P|X)}$: The distance between the actual stub in a given muon detector and the track position extrapolated to that detector.
- ρ_{COT}: The radius at which the track cross the front side of the COT. With this request we ensure that these muons exited the COT from its side surface and can pass CMX trigger track requirements.

BMU	
Fiduciality	PES Fiducial
	IMU Fiducial
$E_{HAD} + E_{EM}$	$>$ 0.1 GeV
COT Hit Fraction	$>$ 0.6
Curvature significance	$>$ 12
# of Silicon hits	$\geq$ 3
# of Stub hits	$\geq$ 2
z_{BMU}	$471.6 \leq z_{BMU} \leq 766.6$
	$-433.0 \leq z_{BMU} \leq -764.7$

Table 4.8: BMU muons identification requirements.

CMIOCES Muon	
Uniqueness	Not a CMUP/CMP
	CMX/MsKs
$E_{EM} + E_{Had}$	$>$ 0.1 GeV
# Stereo SL	$\geq$ 3 with $\geq$ 5 hits
Fiducial	Track fiducial to CES
χ^2/dof	$<$ 3.0

Table 4.9: CMIOCES muons identification requirements.

CMIOPES Muon	
Uniqueness	Not a BMU
$E_{EM} + E_{Had}$	$>$ 0.1 GeV
# Stereo SL	$\geq$ 3 with $\geq$ 5 hits
Fiducial	Track fiducial to PES
COT hit fraction	$>$0.6
Curvature significance	$>$12.0

Table 4.10: CMIOPES muons identification requirements.

- z_{BMU}: The z position of the track at the BMU radius (r_{BMU} = 391 cm) corrected for the track's z_0 position according to the following

$$z_{BMU} = z_0 + r_{BMU} \cdot (1 - e^{-2\cdot\eta})/2e^{-2\cdot\eta}.$$

  It is required to the track to point to the IMU muon chambers.

- # of Stub hits: The number of hits in the fiducial muon chamber associated with a specific track.

- d_0: The distance of closest approach of the fitted track to the beamline.

- χ^2: The chi-squared compares the fitted track to the hit information in the tracking detectors.
- Curvature significance: The measured track curvature divided by the curvature error.

4.7.3 Tracks Identification of unknown lepton flavour

In order to recover some of the acceptance lost due to uninstrumented regions or gaps in the calorimeter, high-P_T tracks which enter such *cracks* are counted in this analysis in a separate category (CrkTrk). These CrkTrk objects are predominantly electrons and muons that were otherwise lost. The definition of CrkTrk requires a well measured track which specifically points to a crack in the calorimeter as well as little calorimeter or track activity near the primary track. The identification requirements for CrkTrk leptons are given in Table 4.11. In this case the Isolation requirement is based both on other muons present and on electromagnetic cluster in the closest calorimeter towers. In addition are used more strict selection on Stereo reconstruction of the track and on the χ^2/dof of the track fit. Obviously are considered as CrkTrk only tracks that have not passed any other lepton identification selection.

	CrkTrk
Isolation/P_T	$\leq$ 0.1 using CDF Muon or $\leq$ 0.1 using nearest EM cluster, ΔR <0.05
# Axial SL	$\geq$ 3 with $\geq$ 5 hits
# Stereo SL	$\geq$ 3 with $\geq$ 5 hits
Track $\lvert z_0 \rvert$	$<$ 60 cm
Track $\lvert d_0 \rvert$	$<$ 0.2 cm ($<$ 0.02 cm with silicon)
χ^2/dof	$<$ 3.0
Uniqueness	Not a CMUP/CMP/CMX/MsKs/BMU
In Crack	Not CES or PES fiducial
Conversion	$\neq$1

Table 4.11: CrkTrk identification requirements.

To reduce the CrkTrk fake rate (see Section 4.8) an additional isolation of the track is required, given by

$$\frac{\sum_{i\neq seed}^{N} P_T^i}{P_T^{seed}} < 0.1 \tag{4.15}$$

where N is the number of tracks within a cone of $\Delta R < 0.4$ around the candidate track. This requirement is very important because this category does not have reliable calorimeter information for additional lepton identification. Since these tracks are not expected to leave any large fraction of their energy in the calorimeter they are treated as muons for $\not\!\!E_T$ corrections discussed in Section 4.5.

4.7.4 Trigger Efficiencies

To evaluate trigger efficienciencies we use an approach based on the reconstructed objects in the event. Since we are using single-lepton triggers, we separately evaluate the probability for each

trigger to be fired by the corresponding offline-selected lepton. The lepton categories connected with a trigger used to collect data are called *triggerable* categories and are CMUP, CMP, CMX, CMX-MsKs and TCE. We finally evaluate the trigger efficiency for a given event as the probability that at least one of the reconstructed objects in the event has fired its associated trigger. For the efficiency measurement we require always leptons to have p_T (E_T) $>$ 20 GeV/c in order to be defined as *triggerable* objects, since trigger requirements usually apply a p_T (E_T) $>$ 18 GeV/c online cut to the XFT tracks. In this section we describe in details how muon and electron trigger efficiencies are calculated.
To calculate trigger efficiencies for muons we start selecting $Z \rightarrow \mu\mu$ candidate events in the 76 $< M_{\mu\mu} <$ 106 GeV/c^2 dimuon invariant mass range. Among these events we count those with one of the two muons that fired a reference trigger path (*tag* muon) and the other is fiducial to the detector we're measuring the trigger efficiency (*probe* muon). We then check wether the other muon has fired the trigger or not. We separate calculation for triggers that require *track-stub* match in the $r-\phi$ plane (*2D*) and those that require also a stereo matching, XFT *3D* matching requirement (available after trigger upgrade, described in [32]). Trigger efficiencies for 2D triggers are trivial and are calculated with the following formula (for CMUP 2D trigger paths, similar for others):

$$\epsilon_{CMUP-2D} = \frac{\#(CMUP-2D \ \& \ CMX-2D)}{\#CMX-2D} \tag{4.16}$$

where $\#CMUP-2D$ ($\#CMX-2D$) is the number of events where the corresponding trigger path has fired. The requests for a 3D trigger are the same as the corresponding 2D trigger with an additional requirement on the stereo track match; so, to calculate the efficiencies of 3D triggers we can use two different methods. The first is calculate the efficiency relative to the corresponding 2D trigger path, evaluating in this way just the efficiency of the 3D part of the requirements. The second method is analogous to the 2D method and evaluates directly the entire 3D efficiency.

$$\epsilon^*_{CMUP-3D}(I) = \frac{\#(CMX-2D \ \& \ CMUP-2D \ \& \ CMUP-3D)}{\#(CMX-2d \ \& \ CMUP-2D)} \tag{4.17}$$

$$\epsilon_{CMUP-3D}(I) = \epsilon_{CMUP-2d} \cdot \epsilon^*_{CMUP-3D}(I) \tag{4.18}$$

$$\epsilon_{CMUP-3D}(II) = \frac{\#(CMUP-3D \ \& \ CMX-3D)}{\#CMX-3D} \tag{4.19}$$

Similar formula are used to calculate CMX-2D (3D) efficiency. The two methods agree very well and we use the second one when available, since it gives a slightly more accurate estimation. To calculate the trigger efficiency we take into account the fraction of the active *livetimes* of the triggers, obtaining a corrective scale factor for each efficiency. Results are summarized as function of run period in Table 4.12; periods 14 to 23 (Oct. 2007- Mar. 2009) are together since the behaviour is homogeneous. In this table we notice a drop in CMUP-3D efficiency in period 18, which is due to a technical known problem.

Livetime corrections are also applied and listed in Table 4.12 to account for different prescales of the trigger paths. Trigger efficiencies and livetimes are then applied to MC simulations on a per-event basis, in order to model online triggering effects on the simulation samples.

The efficiency for the electron trigger `CENTRAL_ELECTRON_18` is separately calculated for the tracking trigger and for the calorimeter trigger. The tracking trigger efficiency is calculated using a backup trigger that have the same (or tighter) calorimeter requirements that `CENTRAL_ELECTRON_18`

Run Period	P0	P1	P2	P3	P4	P5	P6	P7	P8
Trigger ϵ									
CMUP 2-D	0.898	0.919	0.919	0.919	0.919	0.919	0.919	0.919	0.906
CMX ARCH 2-D	0.967	0.949	0.949	0.949	0.949	0.954	0.954	0.954	0.941
LiveTimes									
CMUP 2-D	1.000	1.000	1.000	1.000	1.000	1.000	1.000	1.000	1.000
CMX ARCH 2-D	1.000	1.000	1.000	1.000	1.000	1.000	1.000	1.000	1.000

Run Period	P9	P10	P11	P12	P13	P14	P15	P16	P17	P14-17
Trigger ϵ										
CMUP 2-D	0.910	0.920	0.911	0.915	0.918	0.908	0.921	0.906	0.921	0.917
CMUP 3-D (I)			0.858	0.839	0.835	0.881	0.882	0.860	0.875	0.875
CMUP 3-D (II)			0.863	0.838	0.838	0.888	0.885	0.852	0.878	0.876
CMX ARCH 2-D	0.948	0.978	0.970	0.936	0.935	0.915	0.950	0.947	0.940	0.942
CMX ARCH 3-D (I)	(0.927)	0.927	0.930	0.889	0.894	0.892	0.928	0.929	0.905	0.916
CMX ARCH 3-D (II)			0.931	0.894	0.880	0.895	0.928	0.926	0.912	0.916
CMX MS/KS 2-D	(0.849)	0.849	0.814	0.773	0.750	0.847	0.861	0.889	0.816	0.849
CMX MS/KS 3-D (I)		0.835	0.784	0.745	0.737	0.847	0.834	0.879	0.800	0.831
CMX MS/KS 3-D (II)			0.780	0.758	0.766	0.849	0.807	0.864	0.791	0.814
CMP PHI-GAP		(0.948)	0.948	0.891	0.924	0.889	0.764	0.774	0.845	0.803
LiveTimes	P9	P10	P11	P12	P13	P14	P15	P16	P17	P14-17
CMUP 2-D	1.000	1.000	0.959	0.933	0.936	0.945	0.939	0.924	0.923	0.930
CMUP 3-D	1.000	1.000	1.000	1.000	1.000	1.000	1.000	1.000	1.000	1.000
CMX 2-D	0.963	0.958	0.913	0.885	0.899	0.941	0.900	0.845	0.845	0.871
CMX 3-D	0.965	0.988	0.971	0.952	0.950	0.951	0.961	0.989	1.000	0.981
CMP PG	0.000	0.558	0.669	0.840	0.885	0.968	0.977	0.954	0.946	0.959

Run Period	P18	P19	P14-19	P20	P21	P22	P23	P14-23
Trigger ϵ								
CMUP 2-D	0.924	0.907	0.917	0.916	0.902	0.905	0.912	0.913
CMUP 3-D (I)	0.736	0.861	0.826	0.867	0.851	0.857	0.869	0.842
CMUP 3-D (II)	0.744	0.862	0.828	0.871	0.853	0.852	0.868	0.843
CMX ARCH 2-D	0.956	0.927	0.944	0.921	0.954	0.967	0.956	0.948
CMX ARCH 3-D (I)	0.922	0.901	0.916	0.898	0.919	0.937	0.899	0.916
CMX ARCH 3-D (II)	0.900	0.876	0.901	0.883	0.896	0.923	0.885	0.899
CMX MS/KS 2-D	0.813	0.785	0.828	0.802	0.826	0.774	0.863	0.822
CMX MS/KS 3-D (I)	0.792	0.768	0.810	0.783	0.813	0.752	0.811	0.801
CMX MS/KS 3-D (II	0.777	0.774	0.794	0.753	0.787	0.775	0.808	0.787
CMP PHI-GAP	0.758	0.693	0.769	0.794	0.802	0.797	0.838	0.787
LiveTimes	P18	P19	P14-19	P20	P21	P22	P23	P14-23
CMUP 2-D	0.851	0.803	0.876	0.830	0.776	0.800	0.813	0.837
CMUP 3-D	1.000	1.000	1.000	1.000	1.000	1.000	1.000	1.000
CMX 2-D	0.768	0.719	0.802	0.750	0.667	0.701	0.711	0.750
CMX 3-D	1.000	1.000	0.992	1.000	1.000	1.000	1.000	0.996
CMP PG	0.929	0.819	0.920	0.876	0.813	0.800	0.811	0.871

Table 4.12: Trigger efficiencies and livetimes of each trigger for each run periods.

but no tracking requirement: W_NOTRACK. With this trigger we select $W \rightarrow e\nu$ events and check that the electron is pointing to the central electron trigger. We can then evaluate the electron tracking trigger efficiency for the different trigger level (see Sec. 3.8) with the following formulas:

$$\epsilon(L1_{trk}) = \frac{N_W \ \& \ passed \ L1}{N_W} \tag{4.20}$$

$$\epsilon(L2_{trk}) = \frac{N_W \ \& \ passed \ L1 \ \& \ passed \ L2}{N_W \ \& \ passed \ L1} \tag{4.21}$$

$$\epsilon(L3_{trk}) = \frac{N_W \ \& \ passed \ L1 \ \& \ passed \ L2 \ \& \ passed \ L3}{N_W \ \& \ passed \ L1 \ \& \ passed \ L2} \tag{4.22}$$

These efficiencies are calculated as function of several kinematic variables: p_T, ϕ, η, z_0, CalIso($\Delta R = 0.4$), TrkIso($\Delta R = 0.1$), number of jets. The only dependence found are for η and z_0. Near $\eta \sim 0$ there is a significant inefficiency as a result of the COT space bars and also due to the charge collection inefficiency coming from the shorter particle path length. The efficiency has been fitted with the function

$$\epsilon = A - \frac{c}{2\pi\sigma} e^{-\frac{\eta^2}{2\sigma^2}} \tag{4.23}$$

to take into account for this inefficiency in MC simulation. The z_0 efficiency increases for $z_0 \sim 0$; this dependence for the tracking trigger efficiency comes from quite the same kinematical reasons of η inefficiency.

The L1 calorimeter efficiency is calculated from events with one electron that passed the L3 tracking trigger electron and is found to be 100 %. To obtain an unbiased measurement of L2 calorimeter trigger efficiency events that passed L1 selections with no other request are selected. Since the rate is pretty high, those events are selected with a prescaled trigger, L2_PS100_L1_CEM8_PT8, that randomly extract one event every hundred of events that passed L1. From those events the efficiency is then calculated counting the number of events with at least one identified electron (TCE) satisfying the L1 cuts except for the requirement of $E_T > 18$ GeV (instead of 20 GeV) to study the *turn-on* profile of the trigger as a function of the E_T and the isolation ratio[8] less than 0.1 to reduce background. The corresponding formula is

$$\epsilon(L2_{cal}) = \frac{N_{el} \ \& \ passed \ L1_{cal} \ \& \ passed \ L2_{PS} \ \& \ passed \ L2_{cal}}{N_{el} \ \& \ passed \ L1_{cal} \ \& \ passed \ L2_{PS}} \tag{4.24}$$

The L2 calorimeter trigger efficiency depends on E_T as a result of the tower clustering algorithm, tower energy calculation and corrections. The turn-on curve reaches 100% at about 30 GeV. The curve is fitted to obtain the efficiency as a function of E_T with the following relation:

$$\epsilon = A - Be^{-CE_t}. \tag{4.25}$$

To measure L3 calorimeter trigger efficiency is used a calibration trigger path, ELECTRON_CENTRAL_8_NO_L2, that is similar to the ELECTRON_CENTRAL_18 trigger but with a lower L1 cut on the jet transverse energy, $E_T > 8$ GeV and the same prescaled trigger used for L2

[8] Isolation ratio is defined as the ratio of calorimeter isolation ($CalIso$) in EM and Had calorimeter.

calorimeter trigger efficiency. The efficiency is then calculated counting the number of identified electrons that pass this trigger path and the L2 calorimeter trigger with the following formula

$$\epsilon(L3_{cal}) = \frac{N_{el}\ \&\ passed\ EL\_CENT\_8\_NO\_L2\ \&\ passed\ L2_{cal}\ \&\ passed\ L3_{cal}}{N_{el}\ \&\ passed\ EL\_CENT\_8\_NO\_L2\ \&\ passed\ L2_{cal}} \tag{4.26}$$

Since the offline cut on transverse energy is $E_T > 20$ GeV and L3 cut is $E_T > 18$ GeV, this efficiency is expected to be close to 100 % with possible small inefficiency due to energy determination (since L3 clustering algorithm is almost identical to the offline algorithm). The L3 calorimeter trigger efficiency is in fact found to be 100 % in the full E_T range.

The total calorimeter efficiency is then evaluated convoluting the electron E_T distribution of the sample of interest with the E_T dependence function. When we use this trigger efficiency to weight MC events a trigger scale factor is calculated event-per-event according to the triggered electron E_T.

4.7.5 Lepton ID efficiencies

All lepton identification efficiencies are measured using Drell-Yan events which have two electrons or two muons in the final state. This provides a high statistics sample of clean events in the data where the efficiencies are measured. The efficiencies are calculated in both Data and Drell-Yan Monte Carlo samples. The values are then compared and if needed a correction is applied to the Monte Carlo predictions to account for any differences in the measured efficiencies in Data and in Monte Carlo. The correction factors derived from the Drell-Yan samples are applied to all sample for the different simulated processes.
In order to isolate Drell-Yan events (in particular in the Data, but the same selections are performed on the MC sample) a first tight lepton (*tag)* is selected; then we look for a second lepton (*probe*) which satisfies the looser identification summarized in Table 4.13 for any different lepton category.

In order to evaluate the efficiency for each lepton type we classify events based on the *fiduciality* of the probe, as defined in Sec. 4.7.

If the tag and the probe lepton have an invariant mass in the Z-mass range (76 GeV/c^2 $< M_{ll} <$ 106 GeV/c^2) then it is considered as a Z event.Once a Z event has been identified the loose leg is tested to see if it pass the full lepton (*tight*) requirements. For TCE, CMUP and CMX leptons *tag* and *tight* selections are the same (i.e. we use a CMUP tag lepton to measure CMUP ID efficiency). The resulting efficiency is given by

$$\epsilon_{ID} = \frac{2\ N_{Tight-Tight}}{2\ N_{Tight-Tight}\ +\ N_{Tight-Fail}} \tag{4.27}$$

where $N_{Tight-Tight}$ is the number of events which have two leptons which pass the tight lepton selection and $N_{Tight-Fail}$ the number of the events where the loose leg fails to pass the tight identification cuts.
For the other lepton type we either use a TCE, CMUP or CMX as the tag lepton; in this case the efficiency is given by

$$\epsilon_{ID} = \frac{N_{Tag-Tight}}{N_{Tag-Tight}\ +\ N_{Tag-Fail}} \tag{4.28}$$

where $N_{Tag-Tight}$ is the number of events for which the probe passes the tight selection and $N_{Tag-Fail}$ is the number of the events where the probe failed to pass the tight identification cuts. The Z background evaluated from Z sidebands (M_{ll} $<$ 40 GeV/c^2 or M_{ll} $>$ 140 GeV/c^2) is

Loose TCE
E_T > 20 GeV
p_T > 5 GeV
$\|z_0\|$ < 60 cm

Loose PHX Track
E_{Had}/E_{EM} $\leq$ 0.05
1.2 < η^{2d}_{PES} < 2.0
PEM 3×3 Fit Tower = true
PEM 3×3 χ^2 $\leq$ 10
PES 5×9 U/V $\geq$ 0.65
Isolation/E_T $\leq$ 0.1
ΔR(PES,PEM) $\leq$ 3.0

Loose PHX PEM
E_T > 20 GeV
E_{Had}/E_{EM} $\leq$ 0.05
1.2 < η^{2d}_{PES} < 2.0
Has a PHX Track
N silicon hits $\geq$ 3
$\|z_0\|$ < 60 cm

Loose Central Muon (CMUP/CMP/CMX/CMIOCES/CrkTrk)
p_T > 20 GeV
Track not PES Fiducial
Axial SL $\geq$ 2 with $\geq$ 5 hits
Stereo SL $\geq$ 2 with $\geq$ 5 hits
$\|z_0\|$ < 60 cm

Loose Forward Muon (BMU/CMIOPES)
p_T > 20 GeV
Track PES Fiducial
COT Hit Fraction > 0.6 $\|z_0\|$ < 60 cm

Table 4.13: Loose (denominator) definitions used to measure the identification efficiencies for different lepton types.

subtracted from the signal.
The efficiency for PHX electrons is the product of two efficiencies, PHXTrk and PHXPEM. These refer to the tracking efficiency and calorimeter efficiencies which are measured independently.
An example of the efficiencies found in Data and in Monte Carlo is given in Table 4.14

The ratio of ID efficiencies (ϵ_{ID}) measured in Data and in Monte Carlo sample is the scale factor used later in this analysis and is defined as

$$SF_{lep} = \frac{\epsilon^{Data}_{ID}}{\epsilon^{MC}_{ID}} \tag{4.29}$$

These scale factors are calculated for different periods of data taking and are shown in Table 4.14. The full table list of the measured scale factor is in Appendix A.

4.8 Fake Lepton probabilities

Occasionally a jet can pass the lepton criteria for a given lepton type. The probability of a jet-like object to pass lepton selections and falsely be counted as a real lepton is estimated from Data samples dominated by QCD jets. Four different jet samples are used which correspond to different trigger requirements on the leading jet E_T which are 20, 50, 70 and 100 GeV.
The prescription to determine the fake probability is to look at each jet sample independently and count the number of jet objects that pass a very minimal subset of lepton ID cuts which are given in table 4.15 for $e^{\pm}$ and 4.16 for $\mu^{\pm}$.

The number of such objects is labelled N^{Denom}. The wanted probability is then the ratio of the number of objects that pass the lepton selections (N^{Pass}) to the number of these *denominator*

	data	MC	Scale Fac
TCE	0.876 ± 0.005	0.861 ± 0.002	1.017 ± 0.006
LCE	0.042 ± 0.003	0.045 ± 0.001	0.933 ± 0.078
PHXTrk	0.863 ± 0.004	0.865 ± 0.001	0.998 ± 0.005
PHXPEM	0.850 ± 0.005	0.894 ± 0.001	0.951 ± 0.006
PEM	0.808 ± 0.009	0.857 ± 0.001	0.943 ± 0.011
CrkTrk e	0.792 ± 0.013	0.834 ± 0.002	0.950 ± 0.016
PESTrk	0.369 ± 0.005	0.404 ± 0.001	0.913 ± 0.013
CMUP	0.879 ± 0.011	0.903 ± 0.001	0.973 ± 0.012
CMU	0.000 ± 1.000	0.000 ± 1.000	0.000 ± 1.000
CMP	0.000 ± 1.000	0.000 ± 1.000	0.000 ± 1.000
CMX	0.947 ± 0.014	0.922 ± 0.003	1.027 ± 0.016
CMXMsKs	0.000 ± 1.000	0.000 ± 1.000	0.000 ± 1.000
BMU	0.826 ± 0.023	0.733 ± 0.004	1.127 ± 0.032
CMIOCES	0.367 ± 0.006	0.350 ± 0.002	1.049 ± 0.019
CMIOPES	0.689 ± 0.012	0.689 ± 0.002	1.000 ± 0.018
CrkTrk μ	0.733 ± 0.011	0.765 ± 0.002	0.958 ± 0.015

Table 4.14: Lepton ID measured in Data and MC and the calculated scale factor for the different lepton categories (Period 0).

objects. Additionally, this probability is corrected for the presence of real leptons in the QCD sample, N_{EWK}. The electroweak contribution is estimated using inclusive W and Z Monte Carlo sample generated using `PYTHIA`[33].
The fake probability is then given by

$$P_{fake} = \frac{N^{Pass} - N_{EWK}}{N^{Denom} - N_{EWK}^{Denom}}. \tag{4.30}$$

In order to avoid any trigger bias, the leading jet is neither considered in N^{Denom} nor N^{Pass}.
The four jet samples give four independent measurement of the fake probability, which are parametrised as function of p_T for muons and E_T for electrons. The fake probabilities are then averaged over the four jet samples for each lepton denominator type to avoid bias due to event momentum. The uncertainty on fake probability is estimated by adding a parameter α to the statistical uncertainty ($\sqrt{stat. + \alpha}$) in each p_T bin until all jet samples agree at the 1σ level.
The probability with which a generic jet fakes a lepton is much lower than the fake probabilities quoted here. The probability with which a generic jet will fake an electron or muon is of the order of 10^{-3} and 10^{-4} respectively. One can vary the denominator definitions and obtain different fake probabilities, but as long as this variation is reasonable should give a similar fake yield prediction when the probabilities are applied to the denominator objects in "fakeable" sample of events.
In this analysis fake rates play a fundamental role in the background estimation with the *Data driven* method illustrated in Section 6.1.

Fakeable Electron
$E_T > 10GeV$
$E_{Had}/E_{EM} < 0.125 + 0.00045 \cdot E$
Isolation < 0.3
Has a good quality track
Is not a conversion
Fiduciality to central or plug

Table 4.15: Fakeable Electron denominator definitions. The objects are also required to satisfy the fiducial requirements of each lepton type for which it is a fakeable object.

Fakeable Muon
$p_T > 10GeV$
Axial SL ≥ 2 with ≥ 5 hits
Stereo SL ≥ 2 with ≥ 5 hits
Track $\lvert z_0 \rvert < 60$ cm
Track $\lvert d_0 \rvert < 0.2$ cm ($<$ 0.02 cm with silicon)
$E/P < 1$
$\chi^2/dof < 4.0$ ($<$ 3.0 if Run $>$ 186598)
Fiduciality to different muon chambers

Table 4.16: Fakeable Muon denominator definitions. The objects are also required to satisfy the fiducial requirements of each lepton type for which it is a fakeable object.

Chapter 5

Analysis

Contents

Since ZZ production cross section is low we define the analysis cuts to select the signal region to have the acceptance as large as possible without enhancing the background. The signal region selection has been optimised on a Monte Carlo sample of ZZ events. These events are used also to measure the selection efficiency and the expected number of signal events.

5.1 Data Sets

The $ZZ \to lll'l'$ analysis is based on the single lepton triggers already described in Sec.3.8. In this analysis have been used data collected during Periods[1] 0-23 (March 2002-March 2009) which constitutes about 4.8 fb^{-1} of integrated luminosity. The data collected are inserted into different *good run lists*, according to the settings of the detector in different run periods (e.g. with or without Silicon detector active). Each data event is required to have a run and section number in one of these lists depending on the lepton type reconstructed in the event. In Table 5.1 are listed the good run lists used in the analysis and the relative integrated luminosity.

The first good run list (EM_NOSI) has a minimal set of requirements on the proper operation of the calorimeter and the other fundamental parts of the detector (e.g. COT). The second and the third ones require the muon chambers to be working properly. The other three have a similar set of requirement but also asking for a correct operation of the Silicon detector.

[1] Run *Periods* are arbitrary chunks of $\sim 50 - 500\ \mathrm{pb}^{-1}$ integrated luminosity.

Good run list	$\mathcal{L}$ (pb^{-1})
EM_NOSI	4828.8
EM_CMUP_NOSI	4772.5
EM_MU_NOSI_CMXIGNORED	4661.5
EM_SI	4549.4
EM_CMUP_SI	4499.5
EM_MU_SI_CMXIGNORED	4394.8

Table 5.1: Luminosity for each good run list.

5.2 Monte Carlo datasets

To study the physics processes involved in this analysis we use different Monte Carlo samples. The simulations use PYTHIA[33] or BAUER[34] (for $Z\gamma$ sample) to generate the physical process, using CTEQ5L[35] for the Parton Distribution Functions (PDFs). PYTHIA generates processes at the Leading Order (LO) and incorporates initial and final state QCD and QED radiation via shower algorithms. In many cases MC sample are re-normalised to the theoretical cross section at Next to Leading Order as we will describe in Sec. 5.2.1. The samples are tuned so that the underlying event and p_T spectrum of Z bosons agree with the CDF Data ?ref?. The generated events are then processed with CDFSim, a GEANT based [36] software that reproduce the interaction of the several particles with the whole detector and the hits they leave in it. Finally, simulated data are processes with the same *off-line* software used for the Data and the information is stored in *standard* ntuples (Stntuple) used by the different analyses.
Table 5.4 summarises the physics processes generated along with the corresponding Stntuple dataset, the cross section and the branching ratio used and generator-level filter efficiencies, if applied. In this table the K-factor is defined as the ratio between the NLO theoretical cross section and the cross section used to generate the MC sample. The datasets are used weighted with the luminosity of the period they represent.

5.2.1 Signal Monte Carlo Samples

ZZ The samples are normalised to a Next-to-Leading Order (NLO) cross section of 1.511 pb and include the $\gamma*$ component. More details on the normalisation used are described in subsection 5.2.2. At generator level both Z's can decay inclusively and the events are filtered requiring the presence of two leptons (an electron or muon pair) with p_T greater than 1 GeV and M_{ll} >15 GeV/c^2. The resulting filter efficiency is 0.23 and has taken into account when normalising the Monte Carlo samples.

5.2.2 ZZ Sample Normalisation

To use MC ZZ sample, we calculate the ZZ cross section using MCFM [37](a NLO cross section integrator) and then use this to normalise our PYTHIA sample. Doing this correctly is not so trivial because we need to take into account the effect of the Z/γ^* interference. In fact, the γ^* couples to fermion in a very differently way respect to Z, which means that when the γ^* contribution to the process is relevant, the branching fraction is significantly effected from this. PYTHIA has a complete leading order model for all the four-fermion final states. MCFM, instead,

simulates at next to leading order only the final states that are likely to be measured ($llll$, $ll\nu\nu$, $llbb$, $\nu\nu bb$), so our PYTHIA sample contains final states for which MCFM does not even calculate a cross section.
Specifically, MCFM calculates only specific fermion processes (e.g. $ee\mu\mu$), and then, to obtain the total cross section, it divides by the Z branching fraction. This procedure only works if the Z-pole completely dominates the process, for example in the zero-width approximation.
The usage of these MCFM settings for the full mass range of the PYTHIA sample ($M_{ll} > 15$ GeV) will produce an incorrect result, because the $ee\mu\mu$ cross section for $M_{ll} > 15$ GeV would be scaled using the Z-pole only branching fraction, which is much smaller than the average branching fraction over the whole $M_{ll} > 15$ GeV mass range (see Table 5.2).

All numbers are expressed in %						
		76 $< M_{ll-1} <$ 106 GeV/c^2 and M_{ll-2} in				Z-pole
	$M_{ll} >$15 GeV	[15,40]	[40,76]	[76,106]	[106,140]	PDG[2]
$llll$	1.47 $\pm$ 0.04	4.83 $\pm$ 0.26	2.42 $\pm$ 0.26	1.02 $\pm$ 0.04	0.82 $\pm$ 0.15	1.0
$ll\nu\nu$	4.59 $\pm$ 0.07	8.87 $\pm$ 0.36	7.51 $\pm$ 0.47	4.07 $\pm$ 0.07	4.56 $\pm$ 0.35	4.0
$llqq$	16.45 $\pm$ 0.14	36.37 $\pm$ 0.82	23.26 $\pm$ 0.89	14.19 $\pm$ 0.14	14.75 $\pm$ 0.66	14.1
$\nu\nu\nu\nu$	3.64 $\pm$ 0.06	0.10 $\pm$ 0.04	3.71 $\pm$ 0.33	4.03 $\pm$ 0.07	3.10 $\pm$ 0.29	4.0
$\nu\nu qq$	26.20 $\pm$ 0.18	11.31 $\pm$ 0.41	21.97 $\pm$ 0.86	27.92 $\pm$ 0.21	27.57 $\pm$ 0.95	28.0
$qqqq$	47.64 $\pm$ 0.27	38.53 $\pm$ 0.85	41.13 $\pm$ 1.26	48.78 $\pm$ 0.30	49.21 $\pm$ 1.37	48.9

Table 5.2: Comparison of branching fractions for different mass ranges as implemented in PYTHIA. *Here* $l = e$, μ *or* τ.

We decide to use, instead, MCFM cross section for the individual processes in the mass range 76$< M_{ll} <$106 GeV/c^2 divided by the fraction of the PYTHIA sample which falls in this range. In this mass range the Z-pole dominates respect to γ^* and the PYTHIA branching fractions are consistent with the PDG branching fractions (see Table 5.2). With this calculation we obtain a cross section

$$\sigma(ZZ) = \frac{\sigma(ZZ \to lll'l')}{f^{ZZ\to lll'l'}_{76<M_{ll}<106} \times \epsilon_{filter}} = 1512 \pm 30 \text{ fb}. \tag{5.1}$$

Since these MC samples are used also to ZZ analysis in other decay channels, we use a normalisation obtained averaging the $\sigma(ZZ)$ obtained with the method described for the different decay channel, obtaining as final result $\sigma(ZZ) = 1511$ fb. In Table 5.3 are listed the fractions of the PYTHIA sample in different mass ranges with the cross section normalisation used finally in this analysis.

		Fraction (%) of Pythia sample in 76$< M_{ll-1} <$106 GeV/c^2			
	$M_{ll} >$15 GeV/c^2	$M_{ll-2} \in$[15,40]	$M_{ll-2} \in$[40,76]	$M_{ll-2} \in$[76,106]	$M_{ll-2} \in$[106,140]
$llll$	2.864 $\pm$ 0.042	0.685 $\pm$ 0.020	0.178 $\pm$ 0.010	1.632 $\pm$ 0.032	0.080 $\pm$ 0.007

Table 5.3: Fraction of the Pythia sample in each mass range. *Here* $l = e$ *or* μ.

5.2.3 Background Monte Carlo Samples

$t\bar{t}$ To evaluate the background we used a $t\bar{t}$ sample generated with Pythia with a top mass of 175 GeV/c^2 and normalised to a NLO cross section of 7.9 pb. The sample is filtered on the presence of a lepton pair with $p_T > 1$ GeV/c, with a Br of 0.1027.

$Z\gamma$ One of the main contributors to the background is $Z\gamma$ process and to study that we used Monte Carlo sample generated with Bauer (5events/nb) for $Z\gamma \to ll + X$ for $ll = ee, \mu\mu, \tau\tau$. The events generated are filtered for the presence of a γ with $p_T > 4$ GeV, a dilepton pair with $M_{ll} >$ 15 GeV/c^2 and a $\Delta R_{lepton-photon}$ >0.2

WZ A contribution to the background can come from WZ events. This has been studied with a Monte Carlo. Several samples of WZ have been generated with Pythia with a cross section of 3.46 pb at NLO. W is simulated to decay inclusively while Z decay is filtered for the presence of a lepton pair (ee or $\mu\mu$) with both $p_T > 1$ GeV. This gives a Br×filter efficiency of 0.101×0.754.

mode	Period	Stntuple	σ×Br (pb)	K-factor	Filter Eff
WZ	0-23	we0s6d,we0scd,we0shd we0sld,we0sod,we0sbf we0shf	3.46×0.101	1.0	0.754
ZZ	0-23	we0s7d,we0sdd,we0sid we0smd, we0spd,we0scf we0sif	1.511	1.0	0.233
$t\bar{t}$	0-11	te0s2z	7.9×0.1027	1.0	1.0
$Z\gamma \to ll\gamma$	0-11	re0s33(ee) re0s34($\mu\mu$) re0s37($\tau\tau$)	10.33	1.36	1.0

Table 5.4: Monte Carlo samples used in this analysis.(If cross section is NLO, then K-factor is one.)

To take into account for the different detector and triggers configuration in the first data taking periods, several physical processes (e.g. ZZ, WZ) were generated reading from the online database the detector conditions (*run-dependent* MC). After period 13 (May 2007) the detector became stable and it is not necessary to reproduce it in the MC. The data sets have been merged weighted with the integrated luminosity of the period they are representing. For $t\bar{t}$ and $Z\gamma$ samples we scaled the MC to the full luminosity of the data sample we are considering.

5.2.4 Corrections to the Monte Carlo

Monte Carlo samples are scaled on an event-basis in order to account for the luminosity of the data they represent. In this way we normalise the MC sample to the corresponding data set. We also account for the differences in trigger efficiencies, lepton reconstruction and identification. In Data we apply a requirement on the position of the primary vertex, [-60 cm,60 cm] along the z

axis, around the centre of the detector; same correction is applied to MC. These corrections are summarized in a scale factor:

$$K = \frac{\sigma \times \mathcal{B} \times \epsilon_{\text{filter}} \times \epsilon_i^{\text{trig}} \times s_i^{\text{lep}} \times \epsilon_{\text{vtx}} \times \mathcal{L}_i}{N_i^{\text{gen}}(|Z_0| < 60 \text{ cm})} \tag{5.2}$$

where

- σ cross-section for the Monte Carlo process,
- $\mathcal{B}$ branching fraction for the Monte Carlo process,
- ϵ_{filter} filter efficiency applied for any filter used in the generation process,
- ϵ_i^{tr} effective trigger efficiency for the event i,
- s_i^{lep} effective lepton id scale factor for the event i, calculated multiplying the corresponding scale factor for each reconstructed lepton in the event,
- ϵ_{vtx} run dependent efficiency of the z-vertex position requirement ($|z_0| <$ 60 cm), calculated separately and available for the collaboration,
- $\mathcal{L}_i$ luminosity of the dataset in the good run list in which the event i falls.

5.3 Signal Selection

The candidate selection start by requiring the presence of four leptons with a p_T (E_T) greater than 10 GeV. On data we require that one of the leptons triggered the event; instead, on Monte Carlo we require that one of the leptons is triggerable, with a p_T greather than 20 GeV. The minimum ΔR between all the leptons is required to be > 0.1 to avoid overlaps in leptons reconstruction. Then, to ensure that leptons come from the decay of the two Z's we combine the four leptons in two pairs of same flavour and opposite charge. The first lepton pair, the closest to the nominal Z mass, has to have 76 GeV/c^2 $\leq$ M_{ll-1} $\leq$ 106 GeV/c^2 while the second pair is allowed to have a larger invariant mass, 40 GeV/c^2 $\leq$ M_{ll-2} $\leq$ 140 GeV/c^2 in order to gain acceptance from Z off-shell.

Table 5.3 summarises the efficiency of each cut.

Summary of Efficiencies		
Triggered	one triggerable lepton scaled with trigger efficiency	0.67
4-Recons	4 leptons fully reconstructed in the detector	0.20
Pt min	min Pt request (20 GeV, 10 GeV, 10 GeV, 10 GeV)	0.93
dR min	min($dR_{all-leptons}$ >) 0.1	1.00
Mass cut	76 GeV $< M_{ll-1} <$ 106 GeV , 40 GeV $< M_{ll-2} <$ 140 GeV	0.80
Total		0.097

Table 5.5: Efficiencies of each requirement and the overall.

The main reduction in signal efficiency is due to the request of four leptons fully reconstructed in the detector. Figure 5.2 shows the scatter plot of the two dilepton invariant masses, the closest to the nominal Z mass (M_{ll-1}) on the x axis and the second (M_{ll-2}) on the y axis. It is easy to see that there are several events in the low M_{ll-2} region. This is because the calorimeter has a leakage in lepton energy reconstruction. If the mass window of the second lepton pair is widen the

background grows due to events with one real Z and accidental second lepton pair while the signal gain is smaller. This cut provide the best signal to noise ratio.

In Figure 5.1 is shown the p_T distribution of the four leptons, sorted high to low p_T, in a signal MC sample.

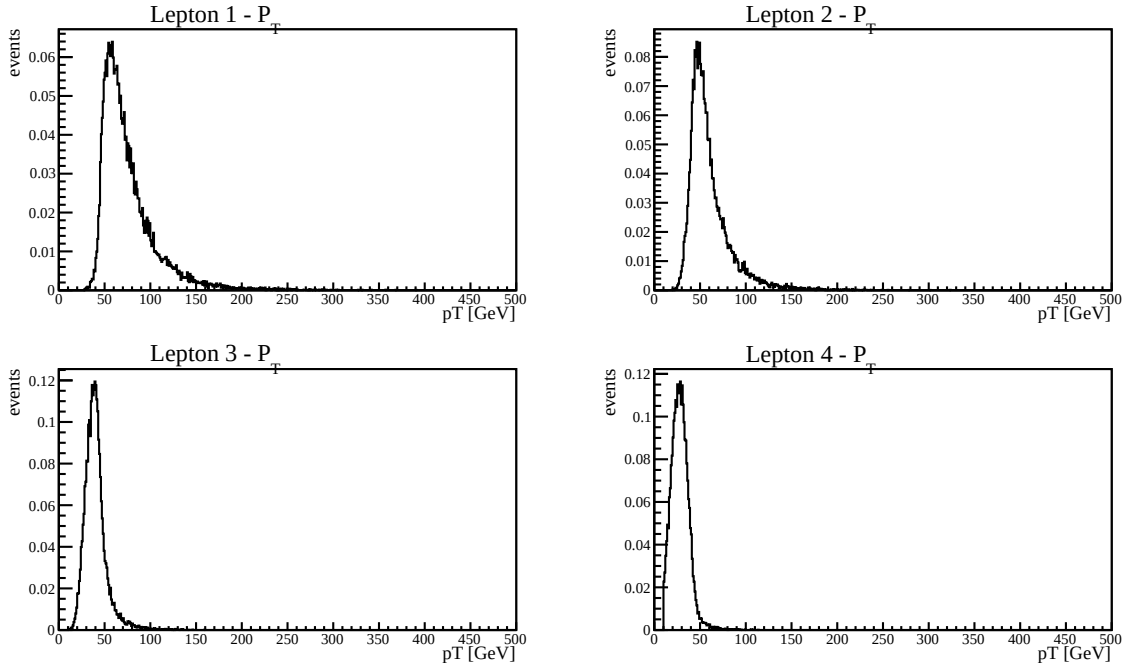

Figure 5.1: p_T distribution for signal events (MC ZZ sample). Leptons are sorted high to low p_T.

From the ZZ Monte Carlo samples we calculate the number of expected events, in the $\sim$4.8fb^{-1}data sample, of $ZZ \to lll'l'$ that pass all cuts:

$$N_{exp.} = 4.68 \pm 0.02(stat.) \pm 0.76(syst.)$$

where the statistical error is due to the statistic of the MC sample. The systematic error is evaluated taking into account different sources of uncertainties, described in section 7.1.

5.3.1 Contribution from $Z \to \tau^+\tau^-$

Only $Z \to e^+e^-$ or $Z \to \mu^+\mu^-$ have been considered in this analysis. As listed in Table 2.1 the Branching Ratio for the decay $Z \to \tau^+\tau^-$ is 3.37 %, a not negligible fraction of Zs decay into a τ pair. We are not interested in τ hadronic decay, which would require a completely different approach, but we might want to reconstruct τs in their leptonic decay ($\tau \to e + \nu$, $\tau \to \mu + \nu$). The requirement on lepton pair to have Same Flavour and Opposite Charge leptons cut away the major part of the $Z \to \tau^+\tau^-$ events, those that decay into different flavour leptons. It is interesting to check whether the removed events are a relevant contribution. The measured Branching Ratio

$$BR(\tau \to e\nu(\gamma)) \; = \; 19.6 \; \% \qquad BR(\tau \to \mu\nu) \; = \; 17.36 \; \% \tag{5.3}$$

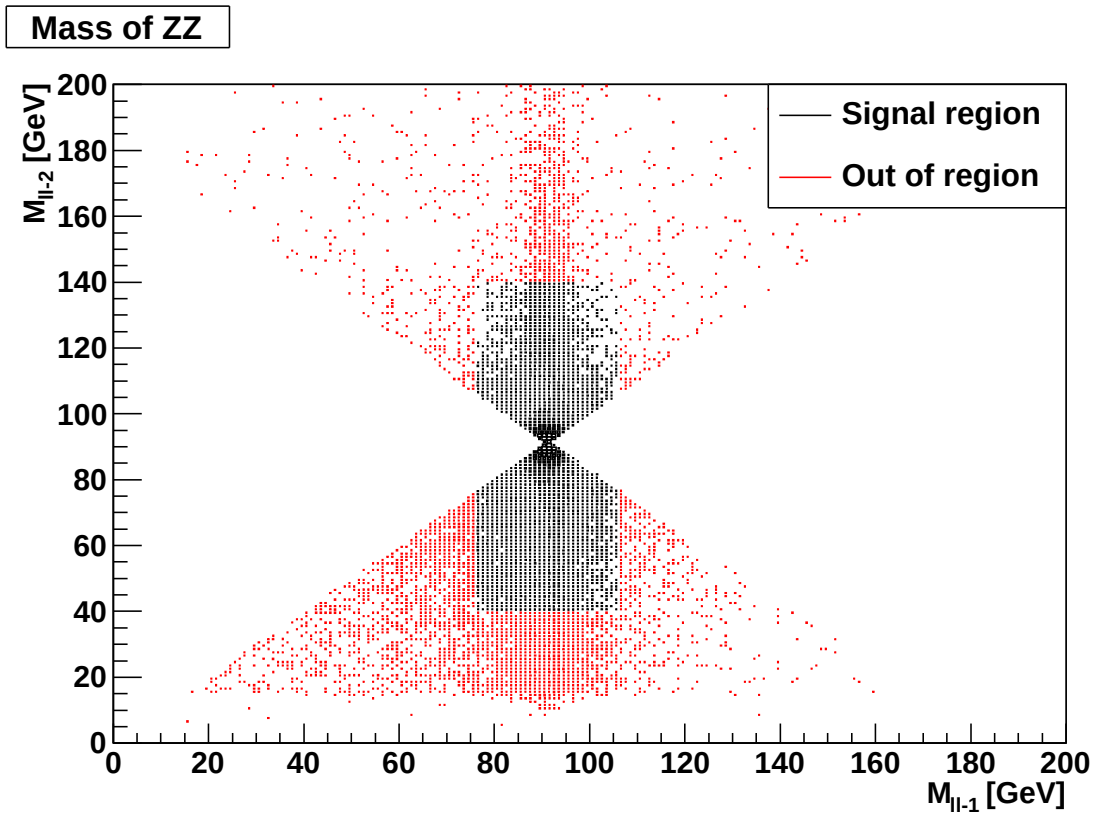

Figure 5.2: Scatter-plot of M_{ll-1} vs M_{ll-2} (sorting M_{ll} from the closest to nominal m_Z peak) for a MC ZZ sample. In black events that pass the mass cuts, in red those that don't pass.

are used to evaluate the total braching ratio of ZZ decaying into two Same Flavour and Opposite Charge pairs including τs decaying in same flavour leptons which is $\sim\ 0.52\ \%$. If we include also the events in which the two τs decay in different flavoured leptons releasing the requirement of same flavour we increase this branching ratio of $\sim\ 0.02\ \%$. This is the maximum increase that we can have. Since the two neutrinos are not reconstructed the dilepton invariant mass has a broader distribution and the requirements on the dilepton masses, 76-106 GeV/c^2 and 40-140 GeV/c^2 cut away a lot of the events from $Z \to \tau^+\tau^-$. To include these events the mass range should be widened for the second invariant mass, to 20-10 GeV/c^2 with a corresponding huge increase of the background in the low-mass region. This behaviour is shown in Fig 5.3. The top row plots show the lepton pairs invariant masses on the left and the second dilepton invariant mass on the right for ZZ simulated events with at least one $Z \to \tau^+\tau^-$. For comparison the bottom row plots show the same quantities requiring same flavour and opposite charge.

In 3.6 fb^{-1} there are 12.8 100^{ths} of event with $N_{\tau-gen}\ > 2$ and requiring Opposite Charge in lepton matching we found

$$8.4\ 100^{ths} \text{ of events in the range } 40 \text{ GeV/c}^2 - 140 \text{ GeV/c}^2 \tag{5.4}$$

$$12.2\ 100^{ths} \text{ of events in the range } 20 \text{ GeV/c}^2 - 140 \text{ GeV/c}^2 \tag{5.5}$$

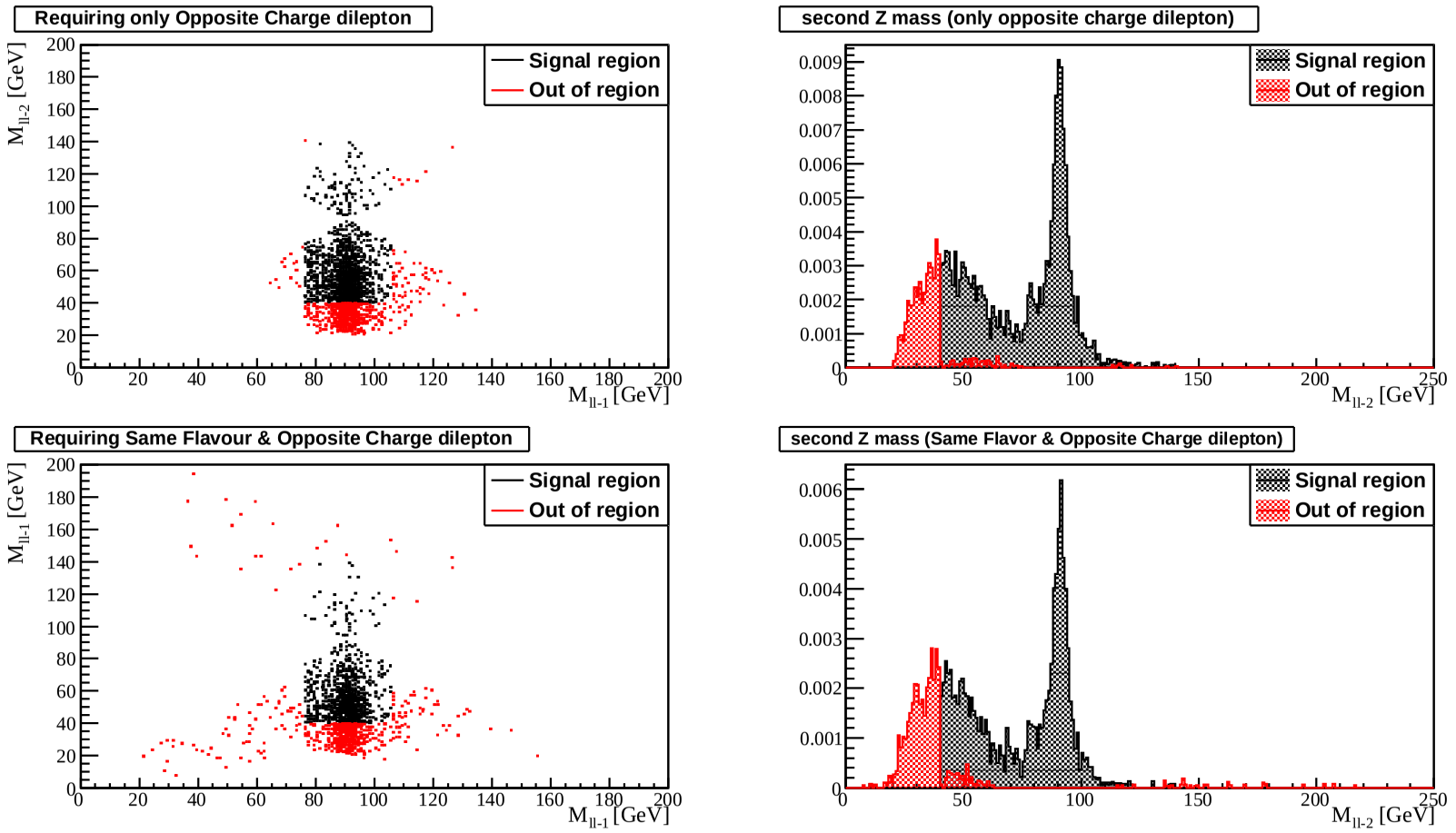

Figure 5.3: Distribution for events with $N_{\tau-gen} > 2$. Scatter plots of M_{ll-2} vs. M_{ll-1} on the left and distribution of M_{ll-2} on the right. The upper row has only the Opposite Charge requirement while the lower row is for Same Flavour and Opposite Charge events. In black events inside the actual signal region.

while in the actual signal region we have

$$5.2\ 100^{ths} \text{ of events in the range } 40\ \text{GeV/c}^2 - 140\ \text{GeV/c}^2 \tag{5.6}$$

$$8.2\ 100^{ths} \text{ of events in the range } 20\ \text{GeV/c}^2 - 140\ \text{GeV/c}^2\ . \tag{5.7}$$

This means that we actually are including in our analysis $\sim$ 40 % of τ events and we could increase this fraction only to $\sim$ 64 % extending the second mass range at the price of increasing the background. We retain therefore the flavour match requirement in Z reconstruction.

Chapter 6

Background determination

Contents

At the energies considered at Tevatron there are no processes with a significant cross section with a four lepton final state. The main background contribution comes therefore from misidentification of *non lepton* objects in the detector. Other contributions from physics processes like $t\bar{t}$ pair have been investigated but they result to be negligible respect to the dominant *fakes* background. The dominant contribution comes from Z+jets and $Z\gamma$+jets processes, where two jets or a jet and a photon are misrecontructed as leptons. To evaluate this background we used two different methods: the first is *Data Driven* and estimate background on real data while the second uses Monte Carlo simulation of several physical processes. In Sections 6.1 and 6.2 the two methods are described in details.

6.1 Data Driven Method

This method is based on the calculation of the probability of an object to be misidentified as a *fake* lepton (see Sec. 4.8). We use the object denominator and calculate its probability to become a lepton using a Data sample enriched in jets. The real lepton contamination of the jet sample is subtracted. Fake rates f_i are calculated with the formula

$$f_i = \frac{N_i(Identified\ Leptons)\ -\ \sum_{j\in EWK} N_{ij}(Identified\ Leptons)}{N_i(Denominator\ Objects)\ -\ \sum_{j\in EWK} N_{ij}(Denominator\ Objects)} \tag{6.1}$$

for each lepton category i as function of the p_T of the denominator object. In order to minimise the ZZ contribution to the fakes other two fake rates have been evaluated by changing the cut on the calorimeter isolation, CalIso. This variable is defined as the ratio between the calorimetric energy in a $\Delta R = 0.4$ cone around the object minus the energy of the object itself and the energy of the

candidate lepton:

$$\texttt{CalIso} = \frac{(\sum_{\Delta R0.4} E_T) - p_T^{lep}}{p_T^{lep}}. \quad (6.2)$$

`Standard` denominators require CalIso$<$0.3 , `NoIso` denominators have no calorimeter isolation requirement while `AntiIso` denominators have CalIso$>$0.2.
Figures 6.1-6.5 show the fake rates for different lepton categories and for the different denominator definitions. The fake rates have been measured using different jet samples, `JET20`, `JET50`, `JET70` and `JET100`, with different trigger requirement on the jet energy to avoid bias on fake rates due to the jet energy request. For the same reason the leading jet was not used. The final value of fake rates is obtained averaging the results obtained in each jet data set and taking as systematic uncertainty the maximum spread between the different measurements.

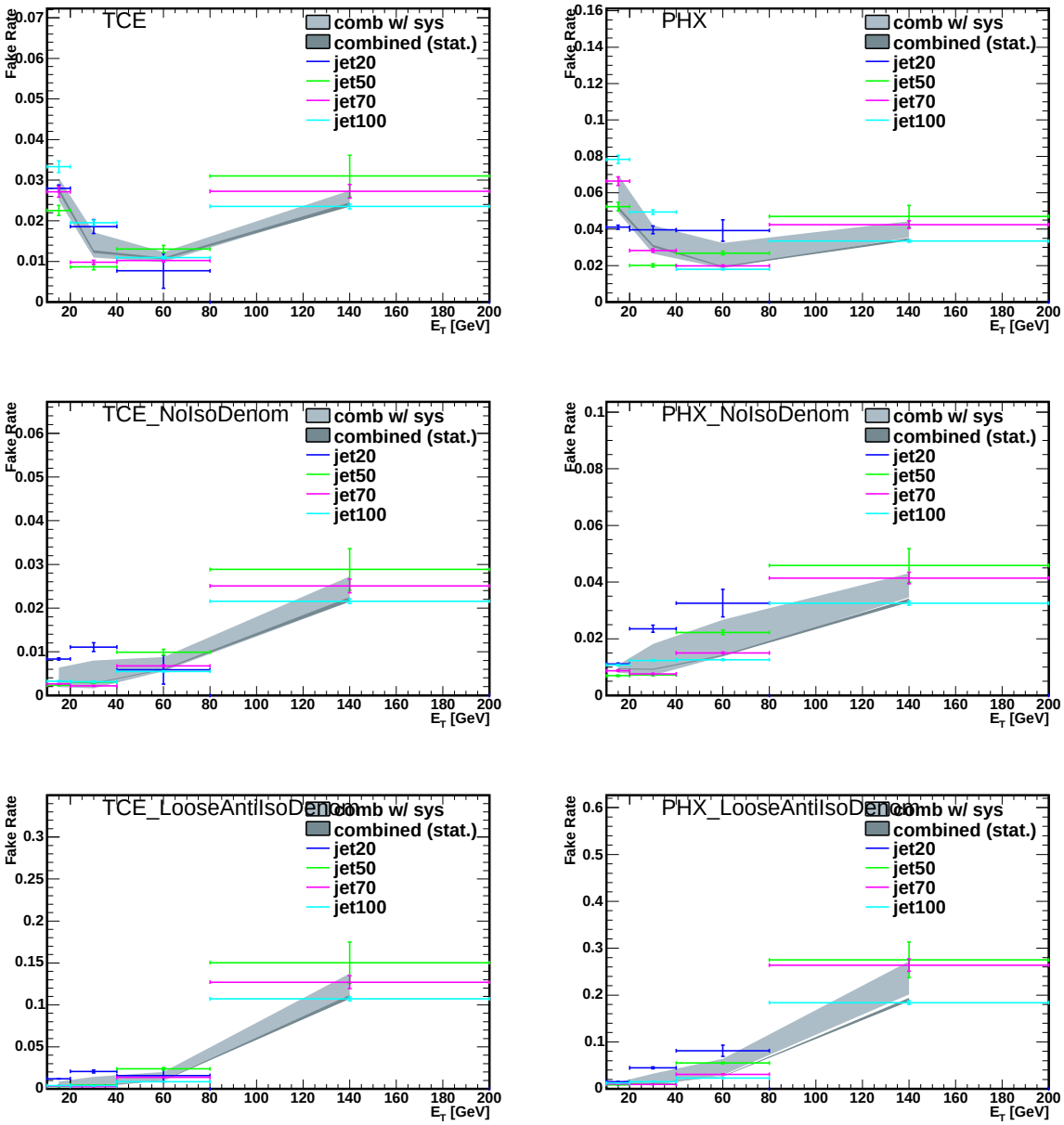

Figure 6.1: Fake rates for different lepton categories and different calorimeter isolation cuts.

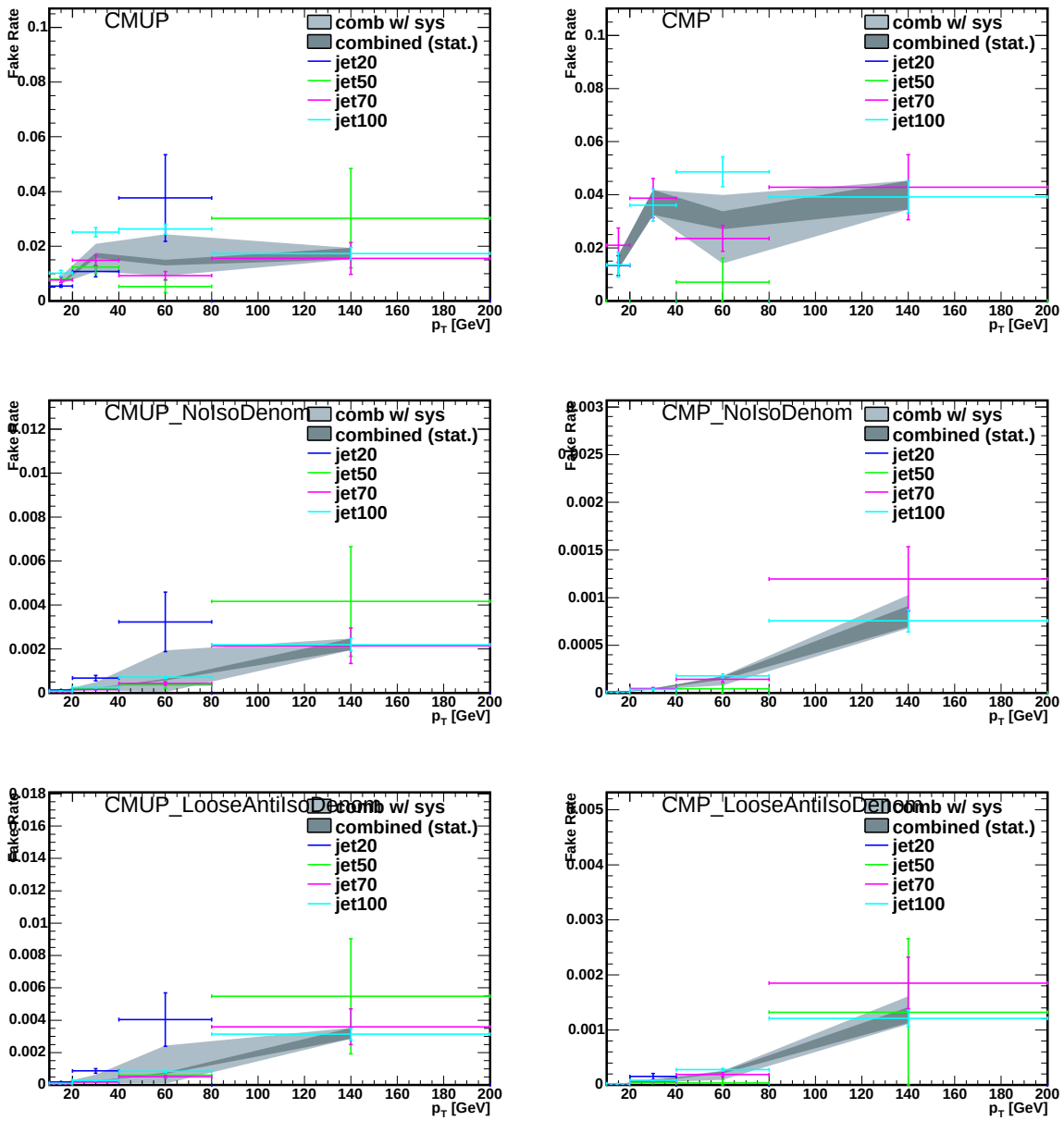

Figure 6.2: Fake rates for different lepton categories and different calorimeter isolation cuts.

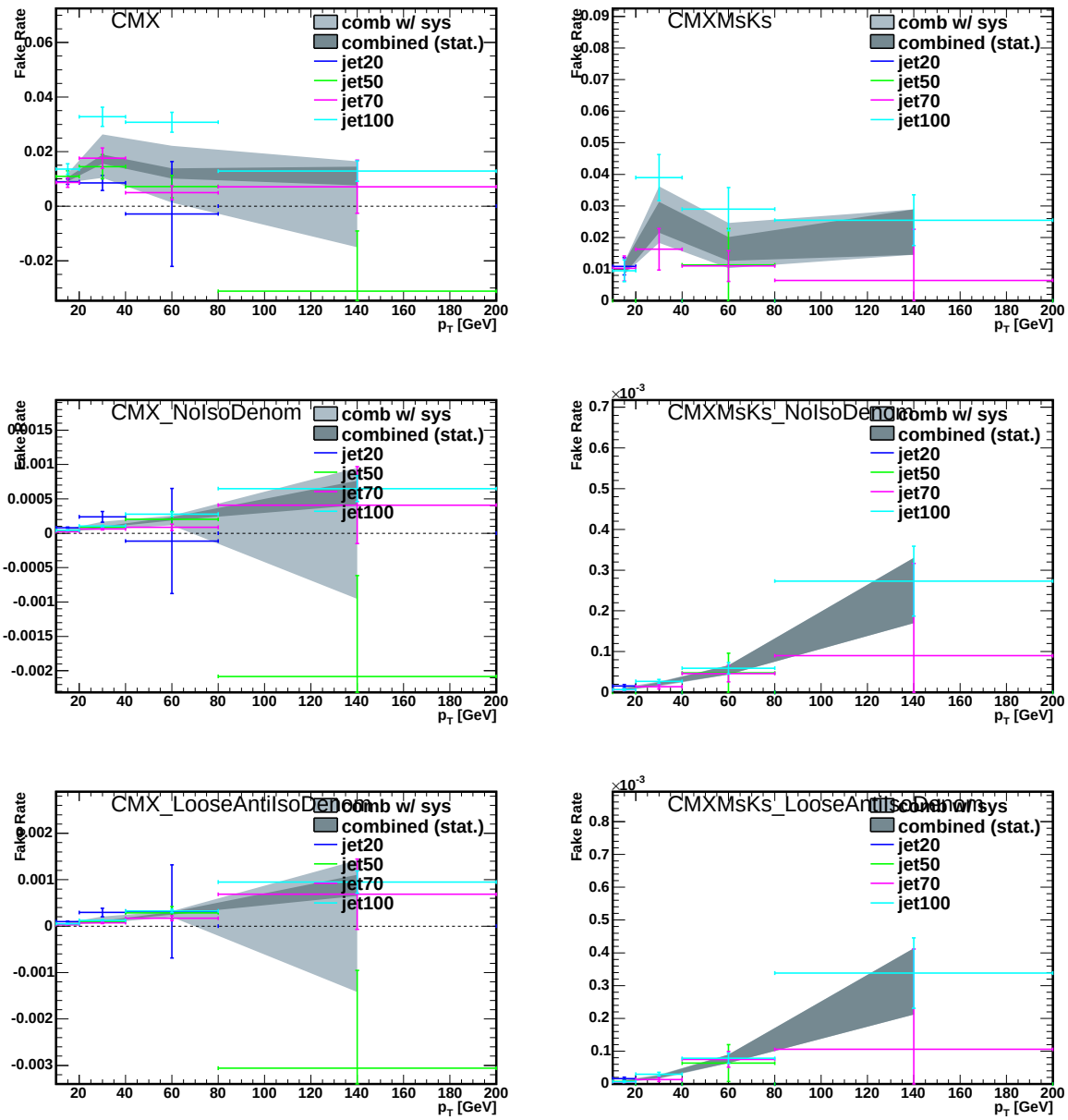

Figure 6.3: Fake rates for different lepton categories and different calorimeter isolation cuts.

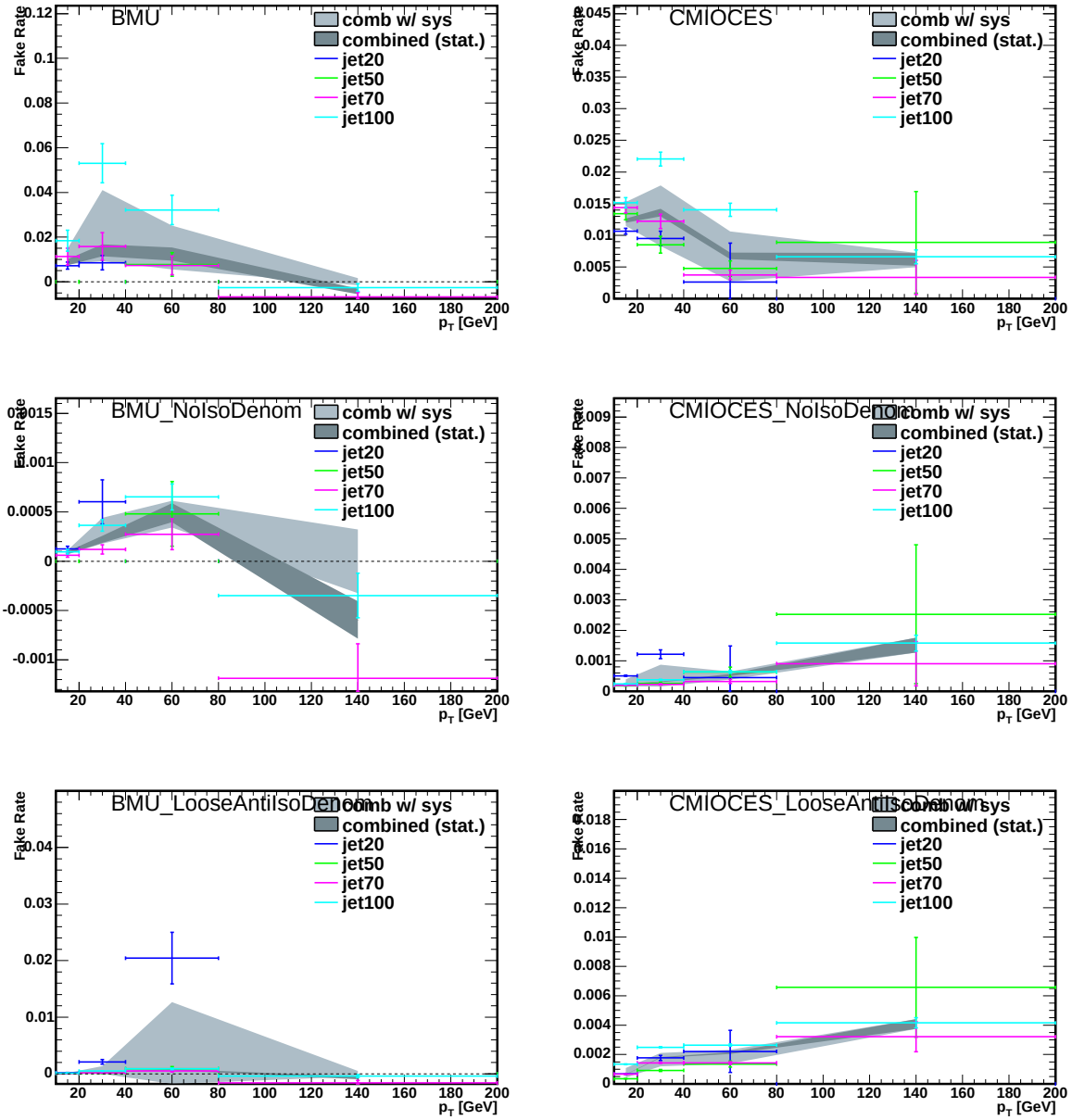

Figure 6.4: Fake rates for different lepton categories and different calorimeter isolation cuts.

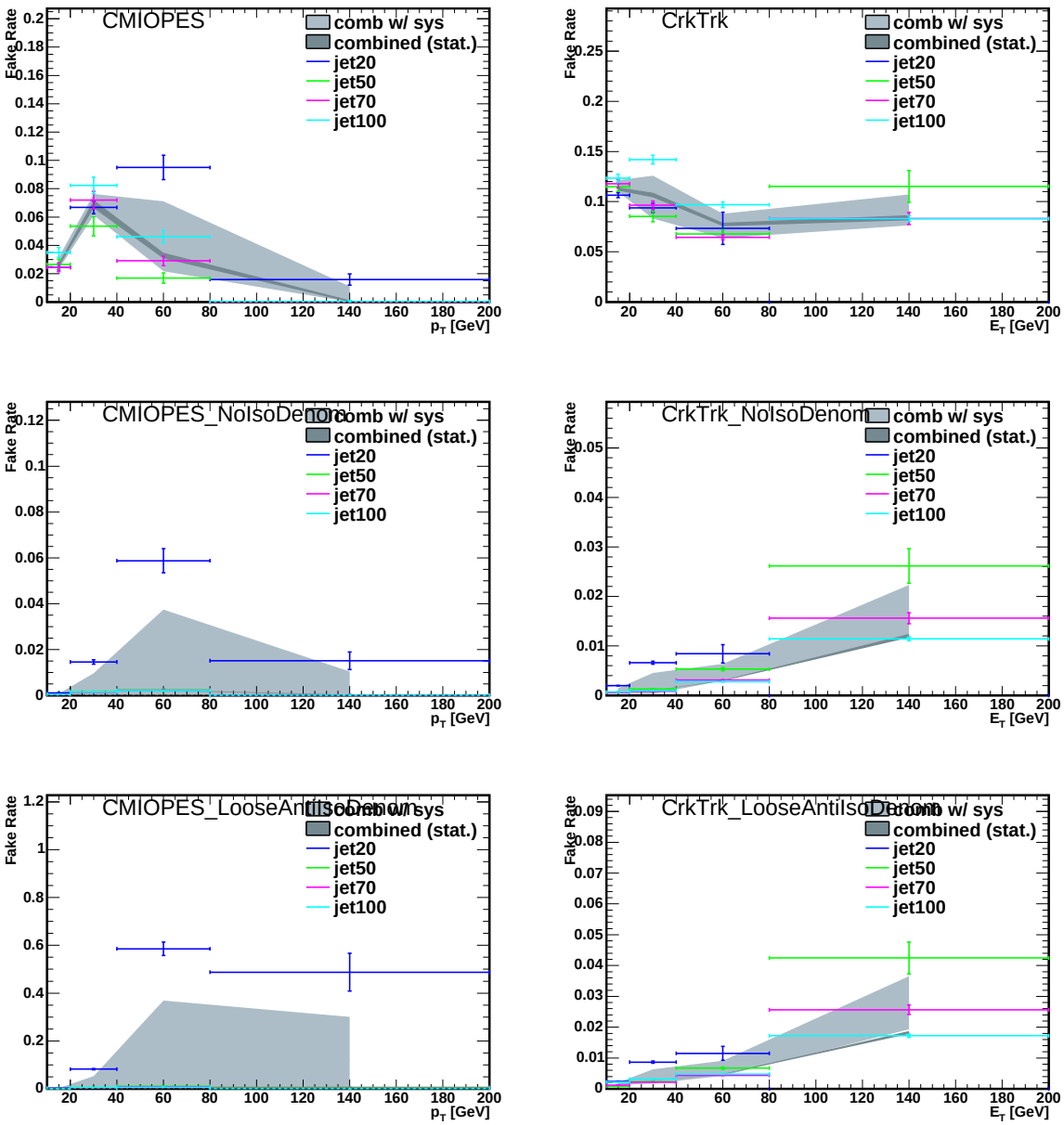

Figure 6.5: Fake rates for different lepton categories and different calorimeter isolation cuts.

To obtain an estimate of the background in the signal sample the denominators in this sample are weighted by the fake rates $f_i(p_T)$. If an event has more than 2(3) leptons or more than 2(1) denominators we create different candidate events for each possible combination of 3 leptons + 1 fake or 2 leptons + 2 fakes. Since the Z+jets and $Z\gamma$+jets events (where the γ is also misidentified as an electron) are the dominant contributions to the background the number of events with three real leptons and one fake lepton (N_{3l+1f}) and the number of events with two real leptons and two fake leptons (N_{2l+2f}) are evaluated. The last one, N_{2l+2f}, is calculated from the sample of events with two leptons and two denominators weighing the event with the fake rate probability of the two denominators:

$$N_{2l+2f} = \sum_{d1,d2} f_{d1}(p_T^{d1}) \cdot f_{d2}(p_t^{d2}) \equiv f^2 \cdot N_{2l+2d}. \tag{6.3}$$

where d_1 and d_2 are the two denominators in each event.
The number of events with three leptons and one fake is calculated starting from the following relation:

$$N_{3l+1d} = N_{Z\gamma+d} \ + \ N_{2l+1f+1d} \ = \ N_{Z\gamma+d} \ + \ 2 \cdot f \cdot N_{2l+2d} \tag{6.4}$$

and then weighting each denominator by the fake probability:

$$f \cdot N_{3l+1d} = f \cdot N_{Z\gamma+d} \ + \ f \cdot \ N_{2l+1f+1d} \ = f \cdot \ N_{Z\gamma+d} \ + \ 2 \cdot f^2 \cdot N_{2l+2d} \tag{6.5}$$

The total number of background events is obtained by summing of the two contributions:

$$\begin{aligned} N_{Z\gamma+1fake} \ + \ N_{Z+2fake} \ &= \ f \cdot N_{Z\gamma+d} + f^2 \cdot N_{Z+2d} && (6.6)\\ &= \ f \cdot N_{3l+d} - 2f^2 \cdot N_{2l+2d} + f^2 \cdot N_{2l+2d} && (6.7)\\ &= \ f \cdot N_{3l+1d} \ - \ f^2 \cdot N_{2l+2d} && (6.8) \end{aligned}$$

The method described above has two main problems. The first one is due to the very low statistics, there are few events with one or two denominator objects with the standard denominators definition. The second issue is created by the contamination of real ZZ events to lepton+denominator(s) sample.

The first problem can be solved releasing the request on calorimeter isolation in the denominator's definition. When the `NoIso` denominators are requested the statistics increases of about one order of magnitude leading to a smaller statistical errors on the background estimation.

The amount of real ZZ events with one (or more) lepton(s) failing the lepton selections is a consistent fraction of the background that can not be neglected. The ZZ contamination is evaluated using the Monte Carlo but we want to reduce it as much as possible, in order to avoid a complex iterative correction that would be needed to proper subtract it for the cross section measurement. The presence of ZZ events in the background is reduced by requiring CalIso > 0.2 (antiIso denominator) since real leptons that did not pass lepton selections have in general a smaller calorimeter isolation than real QCD jets.

In Table 6.1 are shown the results of the background determination calculated with the described method, the numbers are expressed in 100^{ths} of events. The second and fifth columns have the number of candidate events containing denominator objects for the *3l+d* and *2l+2d* components respectively, third and sixth columns have the corresponding fake rate weighted denominators and fourth and seventh columns report the Monte Carlo estimate of ZZ contamination. The total number of background events calculated using the Eq. 6.8 is summarized in column 8 with the statistical uncertainty and the systematic error added in quadrature. The statistical uncertainty is

obtained weighting with the average fake rate the statistical error on the number of denominator events while the systematic errors come from systematic uncertainty on fake rates for each event.

The background evaluation performed with the `AntiIso` denominator has higher statistics and the smallest ZZ contamination and it is used in the final analysis.

All numbers are expressed in 100^{ths} of event							
	3l+1d			2l+2d			Tot.Fake.Est.
$\mathcal{L} = 4.8$	N_{den}	weighted	ZZ	N_{den}	weighted	ZZ	
`Standard` (CalIso<0.3)	9	19.71 ± 8.17	12.5	2	0.40 ± 0.30	0.16	19.31 ± 8.18
`NoIso`	13	8.49 ± 4.30	2.68	106	0.08 ± 0.09	0.01	8.41 ± 4.31
`AntiIso` (CalIso>0.2)	7	4.28 ± 3.29	1.40	91	0.12 ± 0.19	0.44	4.15 ± 2.35

Table 6.1: Background determination using the Data Driven method with the different denominator definitions. All numbers are expressed in 100^{ths} of events.

6.1.1 Multi denominator approximation

When we use equations 6.3-6.8 the background evaluated is overestimated, due to the requirement of exactly four leptons per event. For example, in an event with three real leptons and two denominators two different candidates are created, each one with four leptons (three real and one fake). The two candidates are then weighted with f_1 and f_2 respectively while $f_1(1-f_2)$ and $f_2(1-f_1)$ should have been used, since if both denominators fake a lepton the candidate is rejected by the four lepton requirement. Similar corrections should have done for the different combinations of leptons and denominators. The neglected corrections are, in this case, of the order of $f_1 \cdot f_2$ that are negligible if the fake rates are low (∼1 %), which is the case. If an event contains more than 2 denominators the corrections are more relevant but we neglect them to be conservative.

6.1.2 Heavy flavour contribution

The Data Driven method can be affected by a serious problem due to differences between the sample used to calculate the fake rates and the one used for background determination. Fake rates are averaged on a different sample of jets, with different jet energy and consequently different sample composition. One important difference can be due to a different contribution of *heavy flavour* in jet sample respect to the lepton data, in particular when anti-isolation is required. In the jet sample where we calculate fake rates the contribution from heavy flavour can be estimated comparing the cross section of the processes $p\bar{p} \to q\bar{q}$ and $p\bar{p} \to b\bar{b}$. A rough estimation, for jets with $p_T \sim 50$ GeV/c gives

$$\frac{\sigma(p\bar{p} \to b\bar{b})}{\sigma(p\bar{p} \to q\bar{q})} \sim 10^{-2}. \tag{6.9}$$

In the signal sample we can assume that one Z is real and the contribution of heavy flavour is:

$$\frac{\sigma(Z + b - jet(s))}{\sigma(Z + jet(s))} \sim 5 \cdot 10^{-3} \tag{6.10}$$

and the main contribution of $Z + b$ has come from the process $ZZ \rightarrow l^+l^-b\bar{b}$. In the ZZ Monte Carlo the fraction of events in the signal region that have at least one Z decaying to $b\bar{b}$ respect to the total ZZ contamination is ∼3%. The maximum ZZ contamination to the background is 17.4 % giving the fraction of the background from heavy flavour

$$0.174_{ZZ-cont} \times 0.03_{b\bar{b}} \sim 5 \cdot 10^{-3}, \tag{6.11}$$

Over 104 candidate denominator events less than one event is from $Z \rightarrow b\bar{b}$ demonstrating that is not an issue.
It is interesting to notice in Fig. 6.6 that, in $2l + 2d$ events, the $CalIso$ distribution for the two denominators (lower plots) has the same profile for $q - jets$ and $b - jets$ denominators. This imply that the $CalIso$ variable is not sensitive to the heavy flavour. Instead, from the different profile of the black distribution (total), it is clear that using the `AntiIso` denominators we can reduce a lot the ZZ contamination to the background estimation.

6.2 Monte Carlo-based Method

Since the data driven background determination has shown several issues we decided to cross check the results by using Monte Carlo simulation. We evaluated the contribution to the signal sample of different physics processes applying the measured fake rates to the denominator objects found in WZ,$t\bar{t}$ and $Z\gamma$ Monte Carlo data scaled according to Eq. 5.2 to the nominal integrated luminosity.

We found:

WZ 3.3·10^{-3} events

$t\bar{t}$ 2.3·10^{-4} events

$Z\gamma$ 2.7±0.5·10^{-3} events, 1.7±0.1·10^{-3} events with `NoIso` denominators.

The total number of expected background events is 5.7±0.5·10^{-3}. This number is lower than that found on data but in agreement within the errors considering that in data we have a ZZ contamination that is absent in MC. Since we do not expect to be able to reproduce correctly the jet mis-reconstruction in the MC we decided to use the data driven method to determine the number of background event and keep the MC as validation.

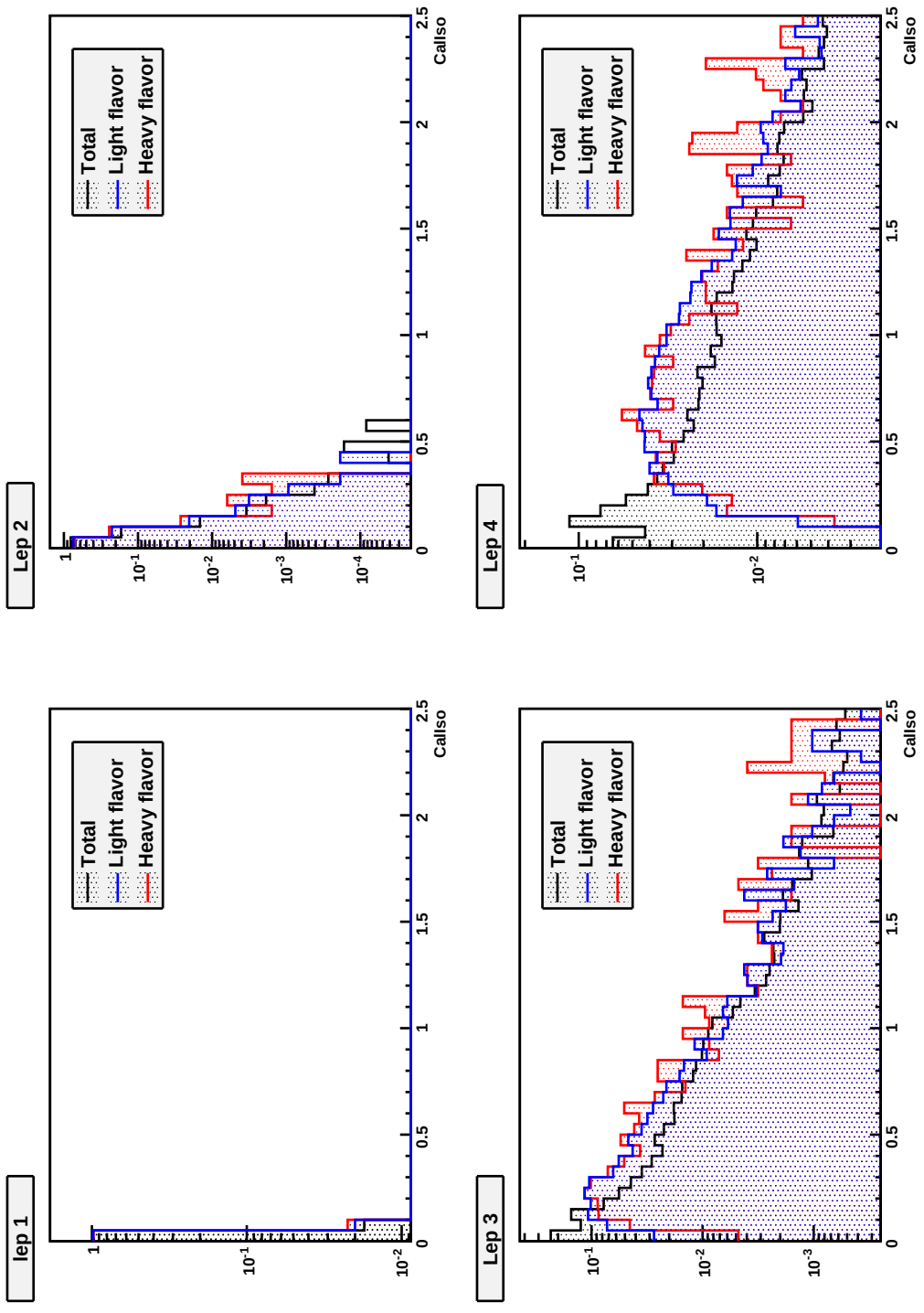

Figure 6.6: Calorimeter isolation distribution of two leptons (top) and the two denominators (bottom) sorted in increasing $CalIso$ from top left to bottom right. The black curve the total contamination of ZZ events to the 2l+2d sample, the blue one is from events with one Z decaying to $q\overline{q}$(light quarks) and the red one with one Z decaying to $b\overline{b}$.

Chapter 7

Results

Contents

7.1 Systematic Errors Determination

Before looking at the Data the actual experiment sensitivity has to be evaluated and to do that what is missing are the systematic uncertainties. In the following the systematic error determination will be described. These uncertainties will be then used also to calculate the systematics uncertainty on the measured cross section and are summarized in Table 7.2.

7.1.1 Fake rate uncertainty

As described in Sec. 6.1 we measured fake rates in different jet samples and took the maximum spread as uncertainty on them. We then apply this uncertainty in the background calculation with the Data driven method, using weights (f_i) shifted for the uncertainty. The uncertainty obtained respect to the background estimation is of 42 % for the sample of $3l + 1d$ and 113 % for the

$2l + 2d$ sample. Those are the most significant systematics and the only considered in the sensitivity calculation.

7.1.2 Lepton ID efficiency

Systematic uncertainties due to the lepton ID efficiencies are calculated varying coherently the lepton ID scale factors by 1σ for each lepton type and counting the number of expected events. From the ZZ MC sample we found a variation of $\pm 3.6\%$ in the number of events expected and we take this as systematic error.

7.1.3 Trigger Efficiency

Uncertainties due to trigger efficiencies are calculated by varying the trigger scale factor for the triggerable leptons of their statistical uncertainties. We then apply the shifted scale factors in MC weight and found a variation of $\pm 2.1\%$ in the number of the expected events. The contribution to the systematic of the variation of the E_T threshold in the electron trigger is calculated by lowering the energy to 16 GeV instead of the nominal 20 GeV in the *triggerable* definition. We found anyway this correction to be negligible in the total trigger efficiency systematics ($<$0.1 %) and it has not been included.

7.1.4 Integrated Luminosity

A systematic of $\pm 6\%$ on the integrated luminosity is used on the total luminosity, as determined by the CDF luminosity group.

7.1.5 ZZ Cross Section

We assigned an uncertainty of $\pm 10\%$ to the theoretical ZZ production cross section used in the MC sample normalisation following the theoretical calculations[37].

7.1.6 NLO Effects on the Acceptance

The Pythia Monte Carlo used for acceptances and efficiencies determination is at LO but the actual theoretical cross section is known at NLO. The systematic error on the total acceptance due to NLO is calculated. To evaluate it two WW Monte Carlo sample have been compared, one generated at LO with PYTHIA and the other generated with MC@NLO, which instead simulate the process with a NLO theoretical cross section. The difference in the total acceptance for the $WW \to ll'\nu\nu'$ between the two MC simulations has been found to be $\sim\ 10\%$ and, since the effect should be comparable for the ZZ process, we assigned the same systematic error on the number of expected events.

7.1.7 PDF Systematics

The uncertainties on the Particle Distribution Functions (PDFs) are propagated to this measurement. The used MC samples have been generated with CTEQ5L PDF[35]. The uncertainty on PDF has been calculated fluctuating the eigenvalues that parametrise the CTEQ6M PDF, the most

recent PDF, obtaining the total positive (negative) fluctuation A^+ (A^-) according to the following formula

$$\Delta A^+ = \sqrt{\sum_{i=1}^{i=20} max(A_i^+ - A_0, A_i^- - A_0, 0)^2}$$
$$\Delta A^- = \sqrt{\sum_{i=1}^{i=20} max(A_0 - A_i^+, A_0 - A_i^-, 0)^2} \ . \quad (7.1)$$

$A^\pm$ is given by the sum in quadrature of the fluctuation of each observable ($A_i^\pm$) respect to the theoretical mean value A^0 and i is the index of the CTEQ6M eigen value pair. Since the MC samples used in this analysis are generated using CTEQ5L it is added as systematic the difference between CTEQ5L and CTEQ6M PDF. The effect of the PDF uncertainty is taken into account separately in both the cross-section and theoretical uncertainty.

For our signal sample we can summarise the effect of PDF uncertainties in Table 7.1.

Sample	ΔA^+	ΔA^-	$\Delta(CTEQ5L - CTEQ6M)$	Total
ZZ	0.1	2.7	-0.0	2.7

Table 7.1: Effect of the PDF variation on the acceptance (numbers are expressed in percent).

The systematic errors on the number of events are summarized in Table 7.2 and it appears that the dominant systematic is due to fake rates determination.

Fractional Uncertainty (%)	
NLO Acceptance	10.0 %
Cross -section	10.0 %
PDF uncertainty	2.7 %
Luminosity	6.0 %
LeptonID $\pm 1\ \sigma$	3.6 %
Trigger Efficiency	2.1 %
Fake rates: 3l+1d	67 %
Fake rates: 2l+2d	158 %

Table 7.2: Summary of the systematic errors.

7.2 Statistical Significance

If we want to measure a rare process it is necessary to evaluate how large is the probability to observe a physical signal just by chance. It means that we want to be able to declare with a certain confidence that the signal we observe is not just a fluctuation (statistical and systematic) of the background. The probability to observe a certain signal as background fluctuation is quantified with the *so called* significance, that can be measured using Monte Carlo prediction (*expected significance*) and the observed Data.

7.2.1 Discovery significance

In searching for new particles is frequent the possibility that the result can be seen as an excess of observed events over the expected background in the selected sample. The standard in the scientific community is to quote a significance for the excess in terms of the number of Gaussian sigma the result deviates by only null hypothesis. For Poisson processes with small numbers of events, the case of this analysis, this is almost always based on the probability that the background alone can account for the observed number of events. Given n_0 observed events, with $B \pm \sigma_B$ expected background, one typically wishes to calculate the probability of observing n_0 or more events, taking into account the uncertainties present. Then one relates this probability to the number of Gaussian standard deviations to quote a significance.
If the uncertainty in the expected number of background events is zero or negligible, then the calculation of the probability $\mathcal{P}_{null}$ of the null hypothesis (only background present) is a straightforward sum over Poisson probabilities:

$$\mathcal{P}_{null} = \sum_{n=n_0}^{\infty} \frac{B^n e^{-B}}{n!} \tag{7.2}$$

To relate this probability to a Gaussian deviation in units of sigma, one simply finds that value of x for which

$$\mathcal{P}_{null} = \sqrt{\frac{2}{\pi}} \int_x^{\infty} e^{-x'^2/2}\, dx'. \tag{7.3}$$

$\mathcal{P}_{null}$ is the same probability calculated from the the Poissonian distribution. If there is uncertainty in the background and if there is more than one channel considered, calculating $\mathcal{P}_{null}$ is more complicate. To calculate that toy simulations are typically used, so called *pseudo-experiments*. With these pseudo-experiments it is possible to simulate several times the experimental results (number of background events) taking into account the uncertainty on that, obtaining finally the $\mathcal{P}_{null}$ probability.

7.2.2 Significance calculation

In order to evaluate the statistical significance of the measurement, the probability to have a number of events equal or greater than those expected due to a background fluctuations has been calculated. Since we obtained the background estimation (described in Sec. 6.1) from the number of candidate events containing one or two denominator objects, we build the probability distribution of the background using a Poissonian distribution of N_{3l+1d} and N_{2l+2d}. Those two distributions are weighted with the *average* fake rate to obtain the probability distribution in terms of expected background events, starting from the Poisson probability

$$P(n,t) = \frac{t^n \cdot e^{-t}}{n!} \tag{7.4}$$

where n is the number of denominator events (*variable*) and t is the mean value for that observed in Data ($t = N_{3l+1d}$ or N_{2l+2d}). From this distribution we can obtain, using an average weight, the statistical distribution of the background

$$P(n,t) = P(b,k) = \frac{(k/w)^{b/w} \cdot e^{-k/w}}{\Gamma(b/w+1)}. \tag{7.5}$$

Here w is the average weight calculated as the ratio of the background estimated and the number of candidate events. $b = n \cdot w$ is the variable value of the background, with the corresponding statistical mean value $k = t \cdot w$. In this way it is possible to obtain a *pseudo*-Poissonian distribution of our background sample ($P(b,k)_{3l+1f}$ and $P(b,k)_{2l+2f}$) from the Poissonian distribution of the number of candidate events ($P(n,t)_{3l+1d}$ and $P(n,t)_{2l+2d}$).
We then combine the probability distribution for the two background contributions and calculate the overall probability by using pseudo-experiments. The systematic error on the background estimation is added to the probability as Gaussian smearing of the number of background events. In the pseudo-experiments generation b is substituted in 7.5 with

$$b \rightarrow b \cdot (1 \ + \ x \cdot s) \tag{7.6}$$

where x is a random number taken from a normal distribution and s is the systematic uncertainty. We finally calculate the probability that the background fluctuate to a number of events equal or greater than the number of expected signal events, previously determined with MC, 4.68 $\pm$ 0.78. This probability is called *p-value* and has to be compared with the Gaussian probability of a signal to fall at a distance of n σ from the mean. This represents the expected significance of the measurement, in units of σ. Figure 7.1 shows the probability to observe 0,1,2,$\cdots$,n events in the null hypothesis, obtained with 10^9 pseudo-experiments. The background probability distribution allows to determine the minimum number of events to be observed, m, necessary to have a signal significance greater than n σ; Figure 7.2 shows the probability to have x events observed in the signal + background hypothesis. Once calculated the minimum m to obtain a n σ significance it is possible summing the probability distribution shown in Fig. 7.2 for $x > m$ to obtain the discovery probability, summarized in Table 7.3 for the most relevant n σ. The same technique is used in Section 7.3 to evaluate the observed significance, for which we evaluate the probability for the background to fluctuate giving a number of events equal or greater than the observed one.

Probability of Observing a Signal	
Significance	Probability
2σ	0.99
3σ	0.95
5σ	0.70

Table 7.3: Probability to have a signal of n σ significance.

7.3 Results

Until now we never looked at the Data to be sure not to introduce any bias on our analysis tuning the cuts for the signal region. At this point we are ready to look at the Data to verify the expectations.
As shown in Sec. 5.3, in $\mathcal{L} = 4.8\ fb^{-1}$ we expect 4.68 $\pm$ 0.78 events, we observe 5 events with 4.15 $\pm$ 1.62(stat) $\pm$ 2.87(syst)$\cdot 10^{-2}$ expected background events. With 10^9 pseudo experiments we obtain a p-value = 1.2 $\pm$ 0.3 $\cdot 10^{-8}$ that corresponds to a significance of 5.7 σ. This increases the previous CDF significance of 4.2 σ in the four leptons channel. The events are listed in Table 7.4:

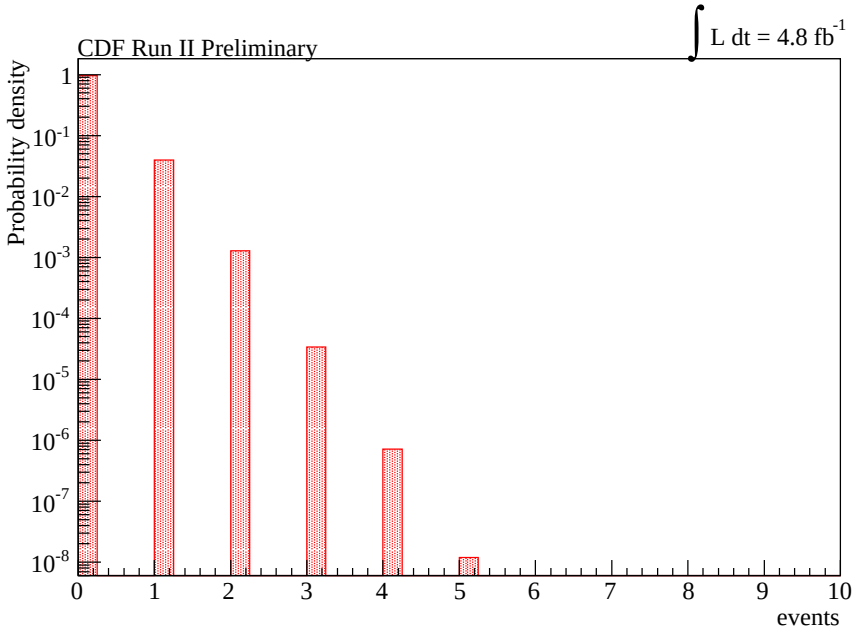

Figure 7.1: Probability distribution to have n events in the null hypothesis from 1000M pseudo experiments.

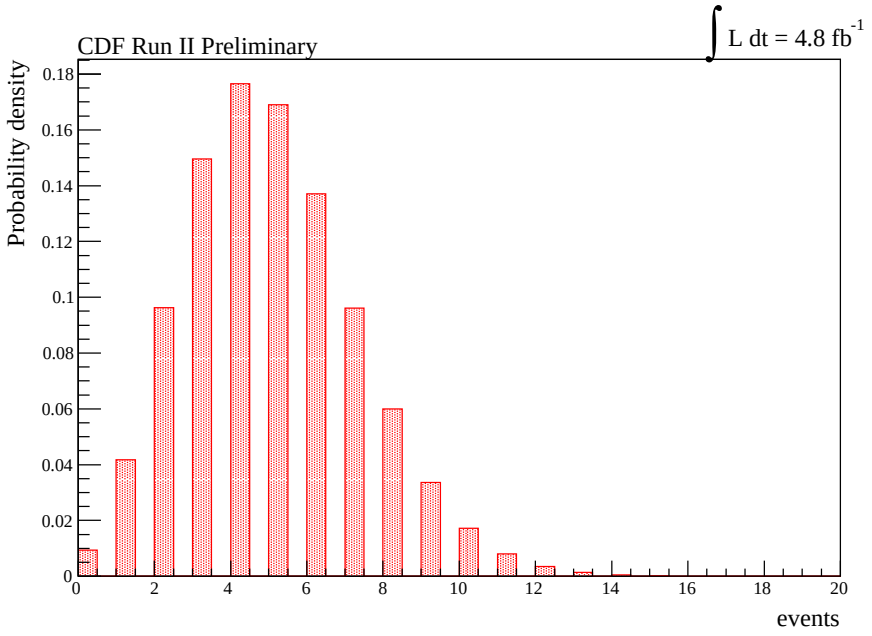

Figure 7.2: Probability distribution for x events in the signal + background hypothesis from 1000M pseudo experiments.

The first two are the same found by the previous CDF analysis. In Appendix B we show the event display of each event. Figure 7.3 shows the invariant mass of the subleading p_T dilepton mass

Run Number	Event number
211311	233113
229084	1785583
268560	5088
270465	996975
270624	9796697

Table 7.4: List of the events that passed the selection criteria.

versus the leading p_T dilepton mass for data (stars), the expected signal from MC (black) and the expected background (red). We can notice that the events found in the Data are well inside the signal region, with most of Zs on-shell and two events out of the region but very close to the.
In Figure 7.4 the p_T of Zs is shown as expected in the MC (left) and measured on data (right). This kinematic check shows that, even if the statistics is very low, events found in Data have no pathological behaviour and bear out the results of this analysis.

7.3.1 Four lepton invariant mass

It is interesting also to consider the distribution of the four lepton invariant mass for the events found in the data because in the future it will be used to verify new physics theories. In Table 7.5 are summarized the dilepton and four lepton invariant mass for the five events found and in Figure 7.5 is shown the distribution of the four lepton invariant mass in Data, Monte Carlo expected signal and background. From Table 7.5 and Fig. 7.5 is possible to see that two out of the five events found are stacked, with a four lepton invariant mass of $\sim$ 325 GeV/c^2. With the low statistics we have is not possible to reach any conclusion about this result but surely it would be interesting to add new data to this analysis and go deeper in it.

Candidate	leptons	$\mathbf{M_{ll-1}}$	$\mathbf{M_{ll-2}}$	4 lepton invariant mass
1	$trk\mu/\mu\mu$	90.5 GeV/c^2	88.5 GeV/c^2	324.8 GeV/c^2
2	$trk\mu/\mu\mu$	91.6 GeV/c^2	94.2 GeV/c^2	169.4 GeV/c^2
3	$ee/\mu\mu$	93.0 GeV/c^2	86.4 GeV/c^2	191.9 GeV/c^2
4	$ee/\mu\mu$	93.3 GeV/c^2	79.7 GeV/c^2	229.2 GeV/c^2
5	$\mu\mu/\mu\mu$	91.7 GeV/c^2	55.1 GeV/c^2	325.0 GeV/c^2

Table 7.5: Lepton type, dilepton invariant masses and four lepton invariant masses for the events found in Data.

7.3.2 Cross section calculation

Using these 5 ZZ events we can calculate the production cross section:

$$\sigma = \frac{N_{Obs} - N_{Bck}}{\mathcal{L} \cdot \epsilon} \tag{7.7}$$

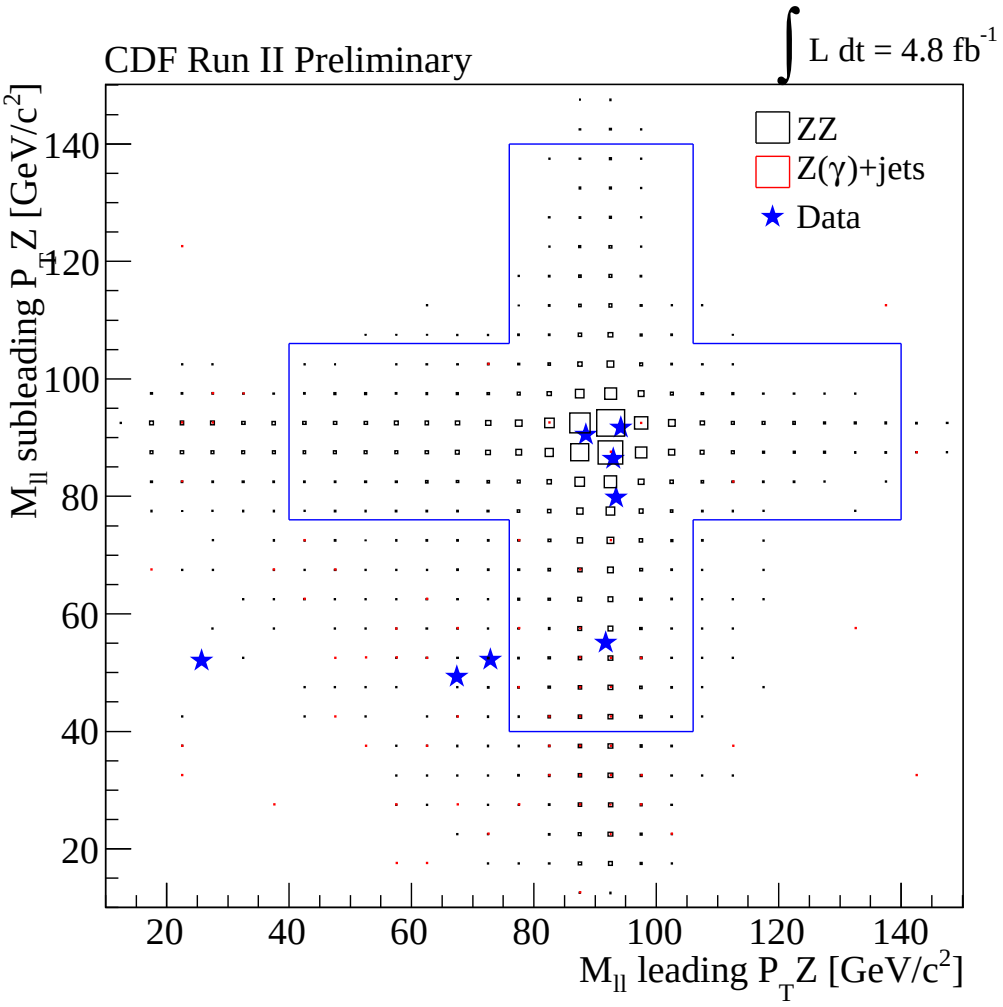

Figure 7.3: Scatter-plot of the Zs masses for the events found in $\mathcal{L}$=4.8 fb^{-1}. In black events in mass cut region; in red events outside mass region cut. The stars indicate the events found in the data.

where ϵ is the total efficiency, N_{obs} the observed events, N_{bck} the expected number of background events and $\mathcal{L}$ the total integrated luminosity:

$$\sigma_{ZZ} = 1.56^{+0.80}_{-0.63}(stat.) \pm 0.25(syst) \tag{7.8}$$

in agreement with the previous CDF measurement [15]. This result has be compared to the MCFM cross section $\sigma_{ZZ} = 1.4 \pm 0.1$ pb (as shown in Figure 8.1).
Though the good significance reached by the measurement, the errors on the cross section are larger than previous measurements, that have been done combining the $ZZ \to lll'l'$ and the $ZZ \to ll\nu\nu$ decay channels. This analysis reached a good sensitivity considering only the four lepton decay channel but a combination with an analysis on the $ZZ \to ll\nu\nu$ would reduce also the errors on the final ZZ cross section. Since the previous ZZ analysis made with CDF data many improvements have been done on lepton reconstruction, and on background modelling so it would

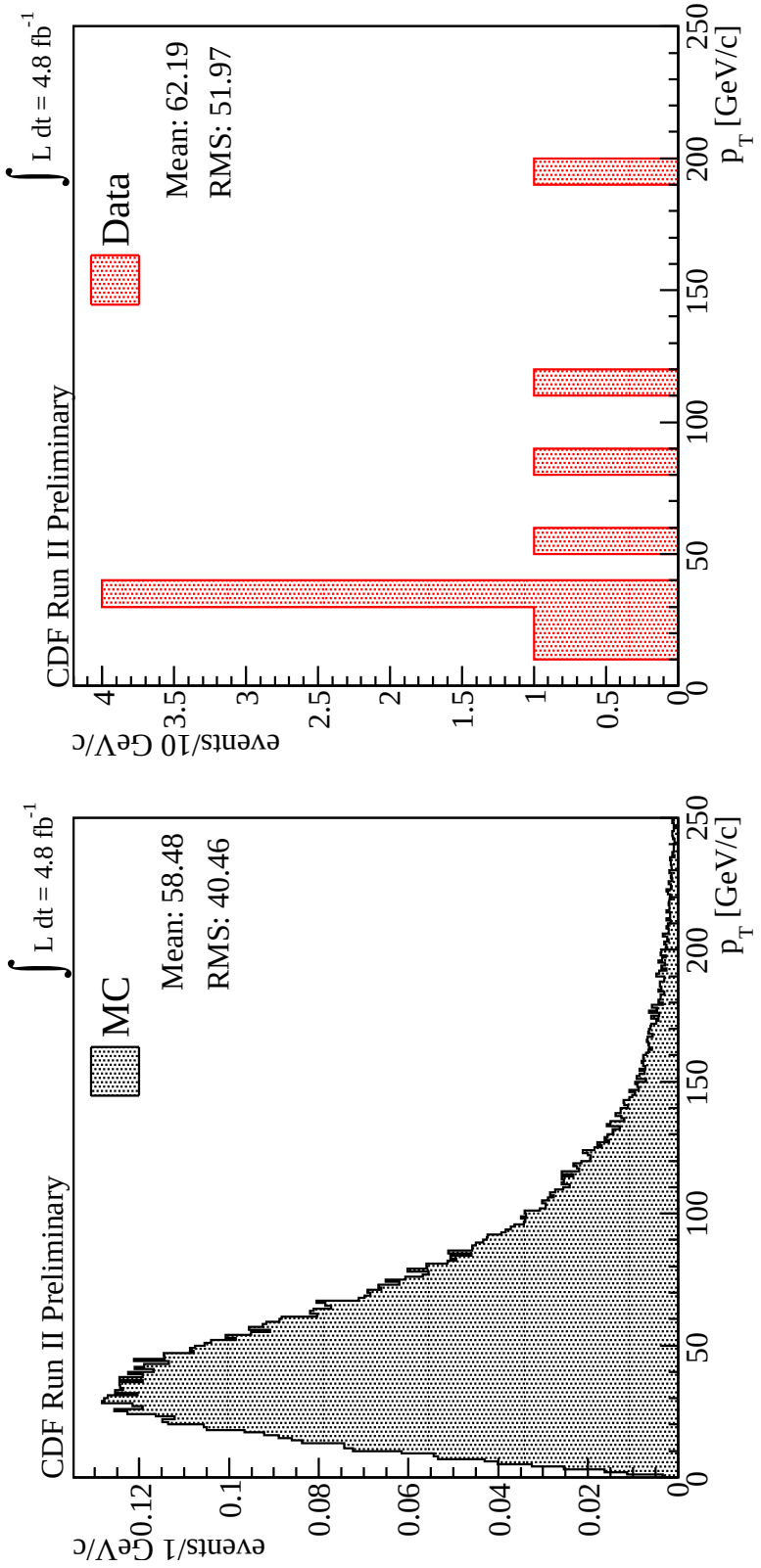

Figure 7.4: p_T distribution of the two Z for each events, on the left MC, on the right found in the data.

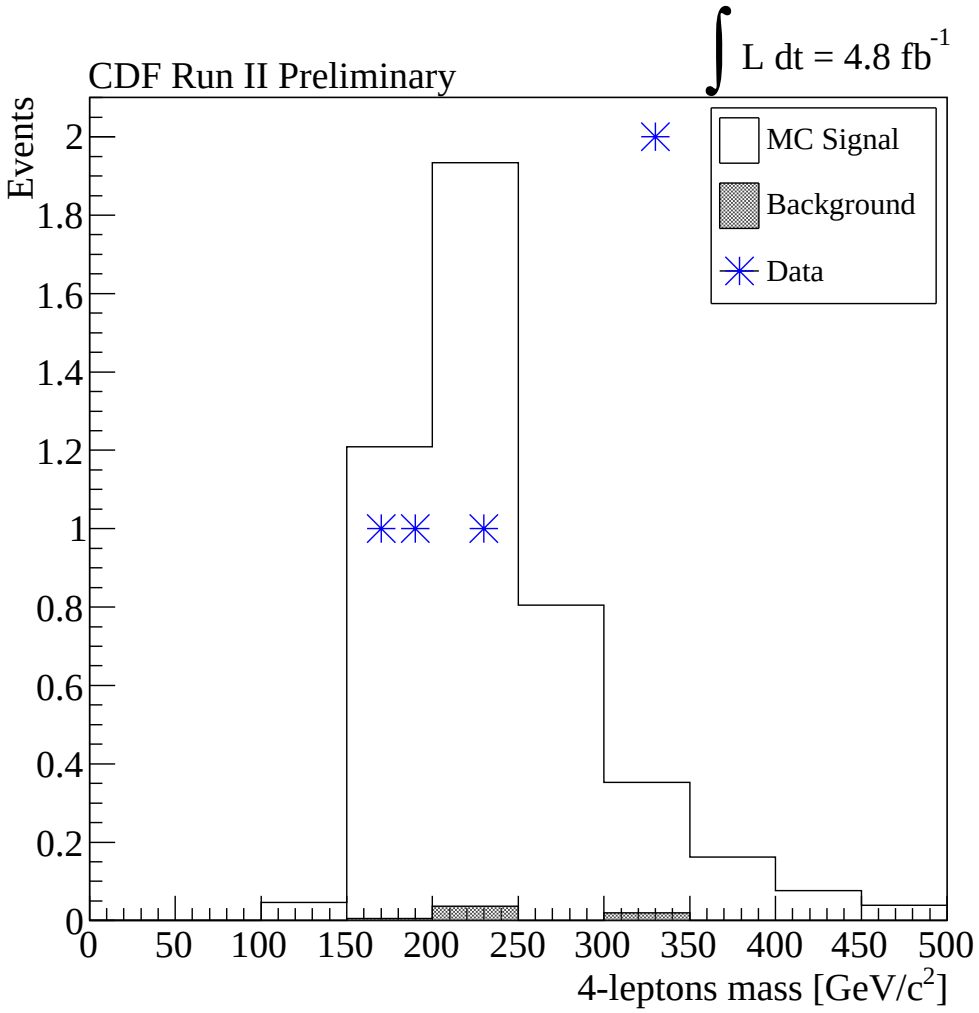

Figure 7.5: The invariant mass distribution of the 4 leptons for the predicted signal from MC, the background and the events found in the data.

be really interesting to update and extend the previous $ZZ \to ll\nu\nu$ analysis to 4.8 fb^{-1} as a natural completion to a precise ZZ cross section measurement.

Chapter 8

Conclusions

We measured the ZZ production cross section in the four lepton decay channel using about 4.8 fb^{-1} of CDF Run II data. We expect 4.68$\pm$ 0.02 (stat.)$\pm$ 0.76(syst.) signal events with a contribution from background of 0.041 $\pm$ 0.016(stat.)$\pm$ 0.029(syst.) events and we observed 5 events, as summarized in Table 8.1.

Events in $\mathcal{L} = 4.8\ \mathbf{fb^{-1}}$	
Signal	4.68 $\pm$ 0.02(stat.) $\pm$ 0.76(syst.)
Z(γ)+jets	0.041 $\pm$ 0.016(stat.) $\pm$ 0.029(syst.)
Total expected	4.72 $\pm$ 0.03(stat.) $\pm$ 0.76(syst.)
Observed	5

Table 8.1: Events expected and observed for the different contribution.

This leads to a measurement for the cross section of

$$\sigma(p\overline{p} \rightarrow ZZ) = 1.56^{+0.80}_{-0.63}(stat.) \pm 0.25(syst.) \text{ pb.} \tag{8.1}$$

The cross section has been determined with a significance of 5.7 σ, never reached by ZZ previous analyses. The one presented in this thesis is then the first CDF observation of ZZ production. The result has been approved by the CDF collaboration and is now public[1].This result is in agreement with previous measurements performed by CDF and $D\emptyset$ collaborations and with the theoretical prediction at NLO

$$\sigma^{NLO}_{SM}(p\overline{p} \rightarrow ZZ) = 1.4 \pm 0.1 \text{ pb} \tag{8.2}$$

as shown in Figure 8.1.

This measurement is a strong test of the predicted Trilinear Gauge Couplings of the Standard Model; contribution from new physics processes would possibly modify these couplings and consequently the measured cross section.

Moreover the presence of resonances decaying to a Z boson pair would be a striking evidence of physics beyond the Standard Model. With more data collected by CDF experiment in the next years the measured invariant mass of the two reconstructed Z can be used to set new limits on the production and masses of such resonances.

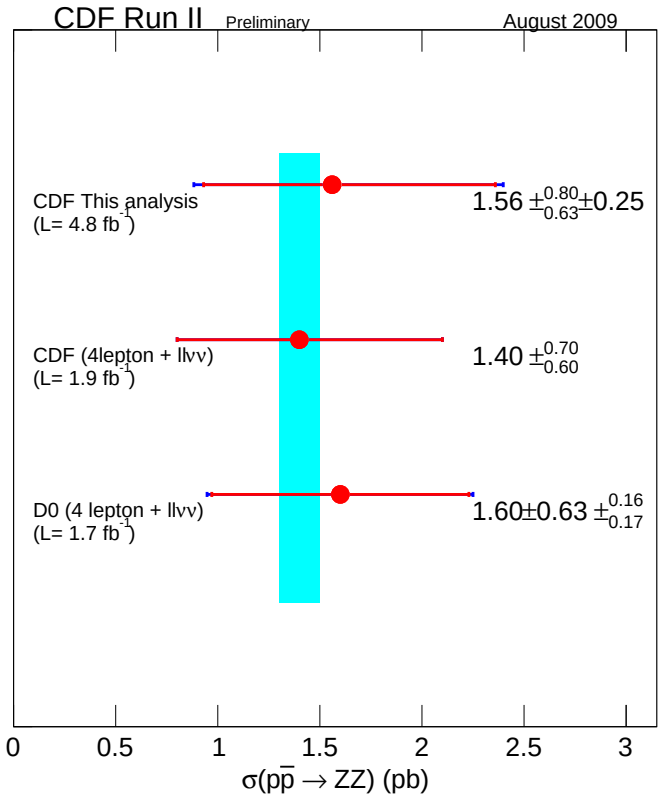

Figure 8.1: ZZ cross section measured by CDF and $D\emptyset$ previous analyses and the theoretical prediction at NLO.

Another really challenging analysis would be the search of the Higgs boson in the high mass region in the $H \rightarrow ZZ$ decay channel. The actual sensitivity of CDF analyses on the search of a Standard Model Higgs boson in the mass range $m_H \in$[170,200] GeV/c^2 is from two to five times the SM prediction. The cross section for the $H \rightarrow ZZ$ process is about 0.05 pb for an Higgs mass of 190 GeV/c^2 [38] so the ratio to the cross section of ZZ production is

$$\frac{\sigma(H \rightarrow ZZ)}{\sigma(ZZ)} \sim \frac{1}{30} \tag{8.3}$$

in $p\bar{p}$ collisions at $\sqrt{s} = 1.96$ TeV.
Therefore this measurement open also the road for the $H \rightarrow ZZ$ channel which would be important to improve the CDF sensitivity in Higgs searches as well as an important benchmark for future collider physics.

Acknowledgements

[1] I need to thank first of all the two persons that grow me up, gave me all I need and support me in almost everything I've done. I would like to thank them also because they told me they want me to study something else and not physics just when it was too late and I was almost done with that.

After that I would like to thank those who allowed the production of this thesis. I would like to thank the guy that may be one day will exclude the existence of the Higgs boson (don't take this sentence too seriously ☺). Since I knew him I learnt a lot of things about how to do physics (and more) with dedication to achieve great results. Thanks for all the days (and nights) spent explaining me things I'm almost ashamed to say that I didn't know. A special thanks goes also to the person that let these months of work to be less frightening than expected. It was a pleasure to work with a person that has such enthusiasm and try always to inject it into the people she works with, included me, reminding that we are so lucky to *play this funny game* they call it physics.

I would like to thank the guy and the lady I shared house and office with during my stay in Chicago because they helped me in many less important (but not negligible) things. They make my working days in America funnier than expected, together with other two (and many more) Italian guys that I met at Fermilab and I shared amusing days with. I want to thank all the crew that tried to stole my (i)phone: good job guys, you cheated me!

I must thank the CDF collaboration and Fermilab, for the great opportunity they gave me and in particular the first physicist I dealt with when I went for the first time at Fermilab. He explained me physics in such an easy way that convinced me that I could have done it.

I would like to thank all my classmates which I shared these years of intense study with. First of all, a double thanks (since I didn't mentioned it last time, when instead he did) to the best team-mate I had during all the physics laboratory done in the past years. I would like to thank him because one day he told me that *we're not living just for physics*, and each day from that one I tried to learn from this life-lesson. A great *thank you* must go to the next most famous *plasma-physicist* (I hope for him). I share with him a lot of amazing moments, from funny videogame matches to deep *steam-bath-winter* conversations. Maybe one day he will teach me also how to play football otherwise I will try with some other sports.

Then I would like to thank some other friends: the südtiroler *biophysicist*, the wise *theorist*, the curly *statistical-physicist*, the Danish *charlatan*, the nerdy *coder*, the tiny *astrophysicist*, the young *engineer* and all the others I've surely forgotten.

A special thanks goes also to THE girl that support me every day, that even if she thinks that physicists are *losers* ☺, let me the possibility to convince her that we are not. It's easy to demonstrate that what you are doing is a *great* thing to people that like it, but it's really harder to convince a person that dislikes it.

[1] Sorry for the rough English but this part has been written in a hurry and almost never checked.

Another thanks goes to the other two ladies of my life, the one that will be always one step beyond me and the other, that gave me the opportunity to enter one of the most posh shop in Chicago, just to buy her a *present*.

Finally I would like to thank one of my best friends, the one that, even if I met no more that two or three times a year, I know I can always rely on (and I hope the same could be for him). I spent with him most of my teen years, those during which you start to think really about *world* and you future life: quite a lot of what I learnt in that period was definitely his credit.

I'm sorry for all the other persons I forgot to mention, it was not my intention, just a matter of time, as most of my life is. Thank you all.

Appendix A

Lepton ID Scale Factors

Run Range: 0d

	data	MC	Scale Fac
CMUP	0.879 ± 0.011	0.903 ± 0.001	0.973 ± 0.012
CMU	0.000 ± 1.000	0.000 ± 1.000	0.000 ± 1.000
CMP	0.000 ± 1.000	0.000 ± 1.000	0.000 ± 1.000
CMX	0.947 ± 0.014	0.922 ± 0.003	1.027 ± 0.016
CMXMsKs	0.000 ± 1.000	0.000 ± 1.000	0.000 ± 1.000
BMU	0.826 ± 0.023	0.733 ± 0.004	1.127 ± 0.032
CMIOCES	0.367 ± 0.006	0.350 ± 0.002	1.049 ± 0.019
CMIOPES	0.689 ± 0.012	0.689 ± 0.002	1.000 ± 0.018
CrkTrk μ	0.733 ± 0.011	0.765 ± 0.002	0.958 ± 0.015
CMUP Trk Iso	0.869 ± 0.011	0.896 ± 0.001	0.970 ± 0.012
CMU Trk Iso	0.000 ± 1.000	0.000 ± 1.000	0.000 ± 1.000
CMP Trk Iso	0.000 ± 1.000	0.000 ± 1.000	0.000 ± 1.000
CMX Trk Iso	0.927 ± 0.014	0.912 ± 0.003	1.016 ± 0.016
CMXMsKs Trk Iso	0.000 ± 1.000	0.000 ± 1.000	0.000 ± 1.000
BMU Trk Iso	0.816 ± 0.024	0.725 ± 0.004	1.126 ± 0.034
CMIOCES Trk Iso	0.364 ± 0.006	0.347 ± 0.002	1.049 ± 0.019
CMIOPES Trk Iso	0.667 ± 0.012	0.683 ± 0.002	0.977 ± 0.018
CrkTrk μ Trk Iso	0.719 ± 0.011	0.756 ± 0.002	0.951 ± 0.015

Table A.1: Muon efficiencies for dataset 0d (period 0) with and without track isolation cut.

Run Range: 0h

	data	MC	Scale Fac
CMUP	0.847 ± 0.008	0.903 ± 0.001	0.938 ± 0.009
CMU	0.000 ± 0.500	0.000 ± 0.500	0.000 ± 0.500
CMP	0.000 ± 0.500	0.000 ± 0.500	0.000 ± 0.500
CMX	0.937 ± 0.015	0.920 ± 0.002	1.020 ± 0.017
CMXMsKs	0.000 ± 0.500	0.000 ± 0.500	0.000 ± 0.500
BMU	0.797 ± 0.018	0.720 ± 0.003	1.107 ± 0.025
CMIOCES	0.364 ± 0.005	0.343 ± 0.001	1.060 ± 0.015
CMIOPES	0.609 ± 0.012	0.606 ± 0.002	1.005 ± 0.020
CrkTrk μ	0.777 ± 0.009	0.795 ± 0.002	0.978 ± 0.012
CMUP Trk Iso	0.834 ± 0.008	0.895 ± 0.001	0.933 ± 0.009
CMU Trk Iso	0.000 ± 0.500	0.000 ± 0.500	0.000 ± 0.500
CMP Trk Iso	0.000 ± 0.500	0.000 ± 0.500	0.000 ± 0.500
CMX Trk Iso	0.906 ± 0.016	0.908 ± 0.002	0.998 ± 0.018
CMXMsKs Trk Iso	0.000 ± 0.500	0.000 ± 0.500	0.000 ± 0.500
BMU Trk Iso	0.767 ± 0.018	0.714 ± 0.003	1.074 ± 0.026
CMIOCES Trk Iso	0.354 ± 0.005	0.340 ± 0.001	1.043 ± 0.015
CMIOPES Trk Iso	0.588 ± 0.012	0.601 ± 0.002	0.979 ± 0.020
CrkTrk μ Trk Iso	0.760 ± 0.009	0.786 ± 0.002	0.967 ± 0.012

Table A.2: Muon efficiencies for dataset 0h (periods 1-4) with and without track isolation cut.

Run Range: 0i1

	data	MC	Scale Fac
CMUP	0.840 ± 0.011	0.902 ± 0.001	0.932 ± 0.013
CMU	0.000 ± 0.577	0.000 ± 0.577	0.000 ± 0.577
CMP	0.000 ± 0.577	0.000 ± 0.577	0.000 ± 0.577
CMX	0.943 ± 0.018	0.919 ± 0.003	1.026 ± 0.019
CMXMsKs	0.000 ± 0.577	0.000 ± 0.577	0.000 ± 0.577
BMU	0.776 ± 0.023	0.721 ± 0.004	1.076 ± 0.032
CMIOCES	0.370 ± 0.006	0.341 ± 0.002	1.085 ± 0.018
CMIOPES	0.617 ± 0.015	0.599 ± 0.003	1.029 ± 0.025
CrkTrk μ	0.774 ± 0.012	0.793 ± 0.002	0.976 ± 0.015
CMUP Trk Iso	0.830 ± 0.011	0.892 ± 0.001	0.931 ± 0.013
CMU Trk Iso	0.000 ± 0.577	0.000 ± 0.577	0.000 ± 0.577
CMP Trk Iso	0.000 ± 0.577	0.000 ± 0.577	0.000 ± 0.577
CMX Trk Iso	0.903 ± 0.018	0.905 ± 0.003	0.998 ± 0.020
CMXMsKs Trk Iso	0.000 ± 0.577	0.000 ± 0.577	0.000 ± 0.577
BMU Trk Iso	0.752 ± 0.023	0.715 ± 0.004	1.051 ± 0.033
CMIOCES Trk Iso	0.363 ± 0.006	0.336 ± 0.002	1.082 ± 0.017
CMIOPES Trk Iso	0.600 ± 0.015	0.594 ± 0.003	1.009 ± 0.025
CrkTrk μ Trk Iso	0.758 ± 0.012	0.783 ± 0.002	0.969 ± 0.015

Table A.3: Muon efficiencies for dataset 0i1 (periods 5-7) with and without track isolation cut.

Run Range: 0i2

	data	MC	Scale Fac
CMUP	0.857 ± 0.008	0.897 ± 0.001	0.955 ± 0.009
CMU	0.000 ± 0.577	0.000 ± 0.577	0.000 ± 0.577
CMP	0.888 ± 0.029	0.919 ± 0.003	0.965 ± 0.032
CMX	0.920 ± 0.013	0.914 ± 0.002	1.007 ± 0.014
CMXMsKs	0.843 ± 0.033	0.907 ± 0.004	0.930 ± 0.036
BMU	0.799 ± 0.015	0.725 ± 0.003	1.099 ± 0.021
CMIOCES	0.332 ± 0.004	0.305 ± 0.001	1.086 ± 0.014
CMIOPES	0.586 ± 0.011	0.598 ± 0.002	0.980 ± 0.018
CrkTrk μ	0.708 ± 0.009	0.722 ± 0.001	0.973 ± 0.012
CMUP Trk Iso	0.837 ± 0.008	0.887 ± 0.001	0.944 ± 0.009
CMU Trk Iso	0.000 ± 0.577	0.000 ± 0.577	0.000 ± 0.577
CMP Trk Iso	0.852 ± 0.029	0.907 ± 0.003	0.939 ± 0.032
CMX Trk Iso	0.906 ± 0.013	0.900 ± 0.002	1.007 ± 0.014
CMXMsKs Trk Iso	0.792 ± 0.032	0.895 ± 0.004	0.885 ± 0.036
BMU Trk Iso	0.759 ± 0.015	0.719 ± 0.003	1.054 ± 0.022
CMIOCES Trk Iso	0.323 ± 0.004	0.301 ± 0.001	1.069 ± 0.014
CMIOPES Trk Iso	0.559 ± 0.011	0.592 ± 0.002	0.946 ± 0.018
CrkTrk μ Trk Iso	0.681 ± 0.008	0.711 ± 0.001	0.947 ± 0.012

Table A.4: Muon efficiencies for dataset 0d (periods 8-10) with and without track isolation cut.

Run Range: 0j

	data	MC	Scale Fac
CMUP	0.825 ± 0.010	0.893 ± 0.001	0.924 ± 0.011
CMU	0.000 ± 0.707	0.000 ± 0.707	0.000 ± 0.707
CMP	0.817 ± 0.020	0.916 ± 0.002	0.893 ± 0.022
CMX	0.898 ± 0.016	0.915 ± 0.002	0.981 ± 0.018
CMXMsKs	0.852 ± 0.029	0.911 ± 0.003	0.935 ± 0.032
BMU	0.773 ± 0.020	0.727 ± 0.003	1.064 ± 0.028
CMIOCES	0.303 ± 0.004	0.252 ± 0.002	1.204 ± 0.019
CMIOPES	0.560 ± 0.013	0.586 ± 0.002	0.955 ± 0.023
CrkTrk μ	0.577 ± 0.012	0.583 ± 0.002	0.990 ± 0.020
CMUP Trk Iso	0.796 ± 0.010	0.882 ± 0.001	0.903 ± 0.011
CMU Trk Iso	0.000 ± 0.707	0.000 ± 0.707	0.000 ± 0.707
CMP Trk Iso	0.796 ± 0.020	0.903 ± 0.002	0.881 ± 0.022
CMX Trk Iso	0.867 ± 0.016	0.895 ± 0.002	0.968 ± 0.018
CMXMsKs Trk Iso	0.839 ± 0.028	0.896 ± 0.003	0.937 ± 0.031
BMU Trk Iso	0.748 ± 0.021	0.720 ± 0.004	1.039 ± 0.029
CMIOCES Trk Iso	0.286 ± 0.005	0.248 ± 0.002	1.152 ± 0.021
CMIOPES Trk Iso	0.532 ± 0.013	0.579 ± 0.002	0.919 ± 0.024
CrkTrk μ Trk Iso	0.549 ± 0.011	0.572 ± 0.002	0.961 ± 0.020

Table A.5: Muon efficiencies for dataset 0j (period 11-12) with and without track isolation cut.

Run Range: 0j13

	data	MC	Scale Fac
CMUP	0.839 ± 0.010	0.895 ± 0.001	0.937 ± 0.011
CMU	0.000 ± 1.000	0.000 ± 1.000	0.000 ± 1.000
CMP	0.819 ± 0.020	0.913 ± 0.003	0.897 ± 0.022
CMX	0.900 ± 0.018	0.913 ± 0.003	0.986 ± 0.020
CMXMsKs	0.815 ± 0.030	0.916 ± 0.003	0.890 ± 0.033
BMU	0.795 ± 0.025	0.696 ± 0.004	1.142 ± 0.037
CMIOCES	0.300 ± 0.005	0.253 ± 0.002	1.186 ± 0.022
CMIOPES	0.520 ± 0.019	0.521 ± 0.003	0.998 ± 0.037
CrkTrk μ	0.560 ± 0.012	0.588 ± 0.002	0.952 ± 0.021
CMUP Trk Iso	0.815 ± 0.010	0.884 ± 0.001	0.922 ± 0.011
CMU Trk Iso	0.000 ± 1.000	0.000 ± 1.000	0.000 ± 1.000
CMP Trk Iso	0.804 ± 0.020	0.901 ± 0.003	0.892 ± 0.022
CMX Trk Iso	0.886 ± 0.018	0.898 ± 0.003	0.987 ± 0.020
CMXMsKs Trk Iso	0.794 ± 0.029	0.904 ± 0.003	0.878 ± 0.032
BMU Trk Iso	0.773 ± 0.025	0.692 ± 0.004	1.117 ± 0.037
CMIOCES Trk Iso	0.290 ± 0.005	0.249 ± 0.002	1.165 ± 0.022
CMIOPES Trk Iso	0.496 ± 0.018	0.517 ± 0.003	0.959 ± 0.035
CrkTrk μ Trk Iso	0.542 ± 0.012	0.578 ± 0.002	0.938 ± 0.021

Table A.6: Muon efficiencies for dataset 0j13 (period 13) with and without track isolation cut.

Run Range: 0k

	data	MC	Scale Fac
CMUP	0.789 ± 0.004	0.889 ± 0.001	0.888 ± 0.005
CMU	0.000 ± 1.000	0.000 ± 1.000	0.000 ± 1.000
CMP	0.804 ± 0.009	0.911 ± 0.002	0.883 ± 0.010
CMX	0.893 ± 0.007	0.906 ± 0.002	0.985 ± 0.008
CMXMsKs	0.827 ± 0.011	0.907 ± 0.002	0.912 ± 0.012
BMU	0.780 ± 0.010	0.705 ± 0.003	1.107 ± 0.014
CMIOCES	0.298 ± 0.003	0.252 ± 0.001	1.184 ± 0.013
CMIOPES	0.567 ± 0.006	0.582 ± 0.002	0.975 ± 0.011
CrkTrk μ	0.564 ± 0.004	0.589 ± 0.001	0.958 ± 0.008
CMUP Trk Iso	0.767 ± 0.004	0.875 ± 0.001	0.877 ± 0.005
CMU Trk Iso	0.000 ± 1.000	0.000 ± 1.000	0.000 ± 1.000
CMP Trk Iso	0.778 ± 0.009	0.897 ± 0.002	0.868 ± 0.010
CMX Trk Iso	0.862 ± 0.007	0.887 ± 0.002	0.972 ± 0.008
CMXMsKs Trk Iso	0.796 ± 0.011	0.891 ± 0.002	0.893 ± 0.012
BMU Trk Iso	0.764 ± 0.010	0.696 ± 0.003	1.097 ± 0.015
CMIOCES Trk Iso	0.288 ± 0.003	0.248 ± 0.001	1.162 ± 0.013
CMIOPES Trk Iso	0.560 ± 0.006	0.574 ± 0.002	0.975 ± 0.011
CrkTrk μ Trk Iso	0.546 ± 0.004	0.577 ± 0.001	0.947 ± 0.008

Table A.7: Muon efficiencies for dataset 0k (periods 14-23) with and without track isolation cut.

Run Range: 0d

	data	MC	Scale Fac
TCE	0.876 ± 0.005	0.861 ± 0.002	1.017 ± 0.006
LCE	0.042 ± 0.003	0.045 ± 0.001	0.933 ± 0.078
PHXTrk	0.863 ± 0.004	0.865 ± 0.001	0.998 ± 0.005
PHXPEM	0.850 ± 0.005	0.894 ± 0.001	0.951 ± 0.006
PEM	0.808 ± 0.009	0.857 ± 0.001	0.943 ± 0.011
CrkTrk e	0.792 ± 0.013	0.834 ± 0.002	0.950 ± 0.016
PESTrk	0.369 ± 0.005	0.404 ± 0.001	0.913 ± 0.013
TCE Trk Iso	0.820 ± 0.005	0.813 ± 0.002	1.009 ± 0.006
LCE Trk Iso	0.032 ± 0.002	0.036 ± 0.001	0.889 ± 0.064
CrkTrk e Trk Iso	0.766 ± 0.012	0.821 ± 0.002	0.933 ± 0.015
PESTrk Trk Iso	0.369 ± 0.005	0.404 ± 0.001	0.913 ± 0.013
PHXTrk Trk Iso	0.863 ± 0.004	0.865 ± 0.001	0.998 ± 0.005
PHXPEM Trk Iso	0.850 ± 0.005	0.894 ± 0.001	0.951 ± 0.006
PEM Trk Iso	0.808 ± 0.009	0.857 ± 0.001	0.943 ± 0.011

Table A.8: Electron efficiencies for dataset 0d (period 0) with and without track isolation cut. No track isolation cut is applied to the PHX category.

Run Range: 0h

	data	MC	Scale Fac
TCE	0.869 ± 0.004	0.862 ± 0.001	1.008 ± 0.004
LCE	0.039 ± 0.002	0.042 ± 0.001	0.944 ± 0.041
PHXTrk	0.880 ± 0.004	0.874 ± 0.001	1.007 ± 0.004
PHXPEM	0.839 ± 0.004	0.882 ± 0.001	0.953 ± 0.005
PEM	0.762 ± 0.008	0.832 ± 0.001	0.916 ± 0.010
CrkTrk e	0.855 ± 0.013	0.864 ± 0.002	0.989 ± 0.016
PESTrk	0.360 ± 0.005	0.379 ± 0.001	0.949 ± 0.013
TCE Trk Iso	0.806 ± 0.004	0.811 ± 0.001	0.994 ± 0.005
LCE Trk Iso	0.029 ± 0.002	0.033 ± 0.001	0.862 ± 0.049
CrkTrk e Trk Iso	0.816 ± 0.011	0.847 ± 0.002	0.963 ± 0.014
PESTrk Trk Iso	0.360 ± 0.005	0.379 ± 0.001	0.949 ± 0.013
PHXTrk Trk Iso	0.880 ± 0.004	0.874 ± 0.001	1.007 ± 0.004
PHXPEM Trk Iso	0.839 ± 0.004	0.882 ± 0.001	0.953 ± 0.005
PEM Trk Iso	0.762 ± 0.008	0.832 ± 0.001	0.916 ± 0.010

Table A.9: Electron efficiencies for dataset 0h (periods 1-4) with and without track isolation cut. No track isolation cut is applied to the PHX category.

Run Range: 0i1

	data	MC	Scale Fac
TCE	0.861 ± 0.005	0.856 ± 0.001	1.006 ± 0.006
LCE	0.042 ± 0.002	0.043 ± 0.001	0.971 ± 0.052
PHXTrk	0.885 ± 0.004	0.869 ± 0.001	1.018 ± 0.005
PHXPEM	0.826 ± 0.005	0.876 ± 0.001	0.944 ± 0.006
PEM	0.742 ± 0.012	0.813 ± 0.002	0.911 ± 0.015
CrkTrk e	0.821 ± 0.016	0.858 ± 0.002	0.957 ± 0.019
PESTrk	0.364 ± 0.006	0.374 ± 0.001	0.974 ± 0.017
TCE Trk Iso	0.794 ± 0.005	0.804 ± 0.001	0.987 ± 0.007
LCE Trk Iso	0.027 ± 0.002	0.033 ± 0.001	0.840 ± 0.080
CrkTrk e Trk Iso	0.788 ± 0.014	0.840 ± 0.003	0.936 ± 0.017
PESTrk Trk Iso	0.364 ± 0.006	0.374 ± 0.001	0.974 ± 0.017
PHXTrk Trk Iso	0.885 ± 0.004	0.869 ± 0.001	1.018 ± 0.005
PHXPEM Trk Iso	0.826 ± 0.005	0.876 ± 0.001	0.944 ± 0.006
PEM Trk Iso	0.742 ± 0.012	0.813 ± 0.002	0.911 ± 0.015

Table A.10: Electron efficiencies for dataset 0i1 (periods 5-7) with and without track isolation cut. No track isolation cut is applied to the PHX category.

Run Range: 0i2

	data	MC	Scale Fac
TCE	0.858 ± 0.003	0.857 ± 0.001	1.001 ± 0.004
LCE	0.041 ± 0.002	0.043 ± 0.001	0.961 ± 0.044
PHXTrk	0.878 ± 0.003	0.878 ± 0.001	1.001 ± 0.004
PHXPEM	0.812 ± 0.004	0.873 ± 0.001	0.931 ± 0.004
PEM	0.698 ± 0.008	0.799 ± 0.001	0.875 ± 0.010
CrkTrk e	0.809 ± 0.012	0.851 ± 0.001	0.948 ± 0.014
PESTrk	0.352 ± 0.004	0.370 ± 0.001	0.947 ± 0.012
TCE Trk Iso	0.782 ± 0.004	0.803 ± 0.001	0.974 ± 0.005
LCE Trk Iso	0.027 ± 0.001	0.033 ± 0.001	0.836 ± 0.046
CrkTrk e Trk Iso	0.762 ± 0.010	0.836 ± 0.002	0.911 ± 0.013
PESTrk Trk Iso	0.352 ± 0.004	0.370 ± 0.001	0.947 ± 0.012
PHXTrk Trk Iso	0.878 ± 0.003	0.878 ± 0.001	1.001 ± 0.004
PHXPEM Trk Iso	0.812 ± 0.004	0.873 ± 0.001	0.931 ± 0.004
PEM Trk Iso	0.698 ± 0.008	0.799 ± 0.001	0.875 ± 0.010

Table A.11: Electron efficiencies for dataset 0i2 (periods 8-10) with and without track isolation cut. No track isolation cut is applied to the PHX category.

Run Range: 0j

	data	MC	Scale Fac
TCE	0.848 ± 0.004	0.851 ± 0.001	0.997 ± 0.005
LCE	0.045 ± 0.002	0.044 ± 0.001	1.028 ± 0.050
PHXTrk	0.878 ± 0.004	0.879 ± 0.001	0.999 ± 0.004
PHXPEM	0.804 ± 0.005	0.858 ± 0.001	0.939 ± 0.005
PEM	0.660 ± 0.010	0.759 ± 0.001	0.870 ± 0.013
CrkTrk e	0.848 ± 0.018	0.847 ± 0.002	1.002 ± 0.021
PESTrk	0.351 ± 0.005	0.362 ± 0.001	0.966 ± 0.015
TCE Trk Iso	0.763 ± 0.005	0.792 ± 0.001	0.965 ± 0.006
LCE Trk Iso	0.029 ± 0.003	0.031 ± 0.001	0.919 ± 0.099
CrkTrk e Trk Iso	0.788 ± 0.014	0.827 ± 0.002	0.953 ± 0.017
PESTrk Trk Iso	0.351 ± 0.005	0.362 ± 0.001	0.966 ± 0.015
PHXTrk Trk Iso	0.878 ± 0.004	0.879 ± 0.001	0.999 ± 0.004
PHXPEM Trk Iso	0.804 ± 0.005	0.858 ± 0.001	0.939 ± 0.005
PEM Trk Iso	0.660 ± 0.010	0.759 ± 0.001	0.870 ± 0.013

Table A.12: Electron efficiencies for dataset 0j (period 11-12) with and without track isolation cut. No track isolation cut is applied to the PHX category.

Run Range: 0j13

	data	MC	Scale Fac
TCE	0.851 ± 0.005	0.855 ± 0.002	0.995 ± 0.006
LCE	0.047 ± 0.002	0.042 ± 0.001	1.119 ± 0.057
PHXTrk	0.860 ± 0.005	0.857 ± 0.001	1.004 ± 0.006
PHXPEM	0.808 ± 0.006	0.863 ± 0.001	0.936 ± 0.007
PEM	0.688 ± 0.010	0.790 ± 0.002	0.871 ± 0.013
CrkTrk e	0.817 ± 0.018	0.846 ± 0.002	0.966 ± 0.021
PESTrk	0.261 ± 0.006	0.283 ± 0.001	0.922 ± 0.021
TCE Trk Iso	0.776 ± 0.005	0.799 ± 0.002	0.971 ± 0.007
LCE Trk Iso	0.034 ± 0.002	0.031 ± 0.001	1.097 ± 0.084
CrkTrk e Trk Iso	0.771 ± 0.015	0.830 ± 0.002	0.929 ± 0.018
PESTrk Trk Iso	0.261 ± 0.006	0.283 ± 0.001	0.922 ± 0.021
PHXTrk Trk Iso	0.860 ± 0.005	0.857 ± 0.001	1.004 ± 0.006
PHXPEM Trk Iso	0.808 ± 0.006	0.863 ± 0.001	0.936 ± 0.007
PEM Trk Iso	0.688 ± 0.010	0.790 ± 0.002	0.871 ± 0.013

Table A.13: Electron efficiencies for dataset 0j13 (period 13) with and without track isolation cut. No track isolation cut is applied to the PHX category.

Run Range: 0k

	data	MC	Scale Fac
TCE	0.847 ± 0.002	0.847 ± 0.002	1.000 ± 0.003
LCE	0.045 ± 0.001	0.043 ± 0.001	1.041 ± 0.047
PHXTrk	0.889 ± 0.002	0.866 ± 0.001	1.027 ± 0.002
PHXPEM	0.773 ± 0.002	0.847 ± 0.001	0.912 ± 0.002
PEM	0.614 ± 0.004	0.733 ± 0.001	0.838 ± 0.006
CrkTrk e	0.806 ± 0.006	0.834 ± 0.001	0.967 ± 0.008
PESTrk	0.323 ± 0.003	0.352 ± 0.001	0.918 ± 0.008
TCE Trk Iso	0.762 ± 0.002	0.786 ± 0.002	0.970 ± 0.003
LCE Trk Iso	0.028 ± 0.001	0.031 ± 0.001	0.897 ± 0.056
CrkTrk e Trk Iso	0.764 ± 0.006	0.814 ± 0.002	0.938 ± 0.008
PESTrk Trk Iso	0.323 ± 0.003	0.352 ± 0.001	0.918 ± 0.008
PHXTrk Trk Iso	0.889 ± 0.002	0.866 ± 0.001	1.027 ± 0.002
PHXPEM Trk Iso	0.773 ± 0.002	0.847 ± 0.001	0.912 ± 0.002
PEM Trk Iso	0.614 ± 0.004	0.733 ± 0.001	0.838 ± 0.006

Table A.14: Electron efficiencies for dataset 0k (periods 14-23) with and without track isolation cut. No track isolation cut is applied to the PHX category.

Appendix B

Event display

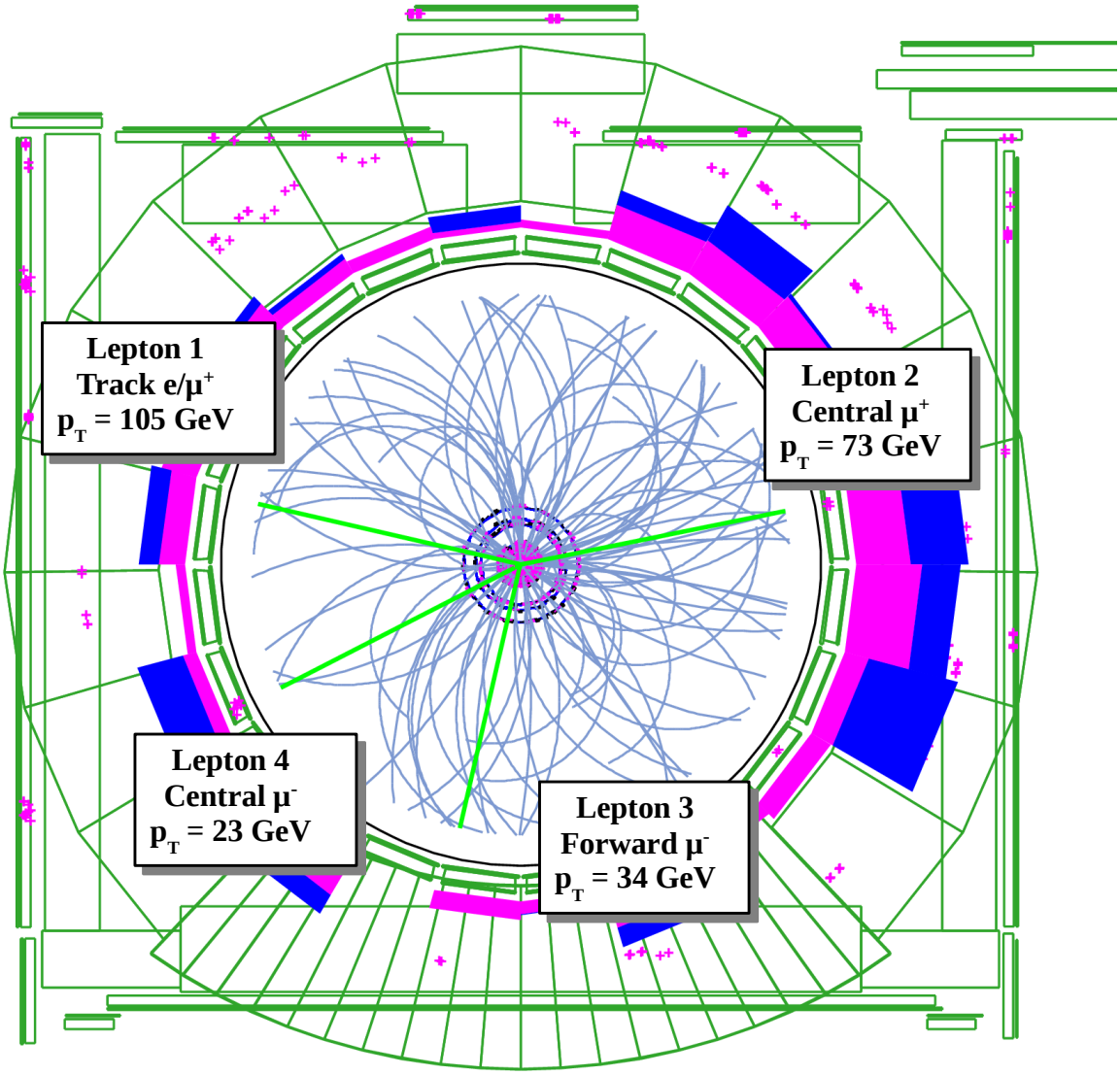

Figure B.1: COT view. Run number: 211311, Event number: 233113.

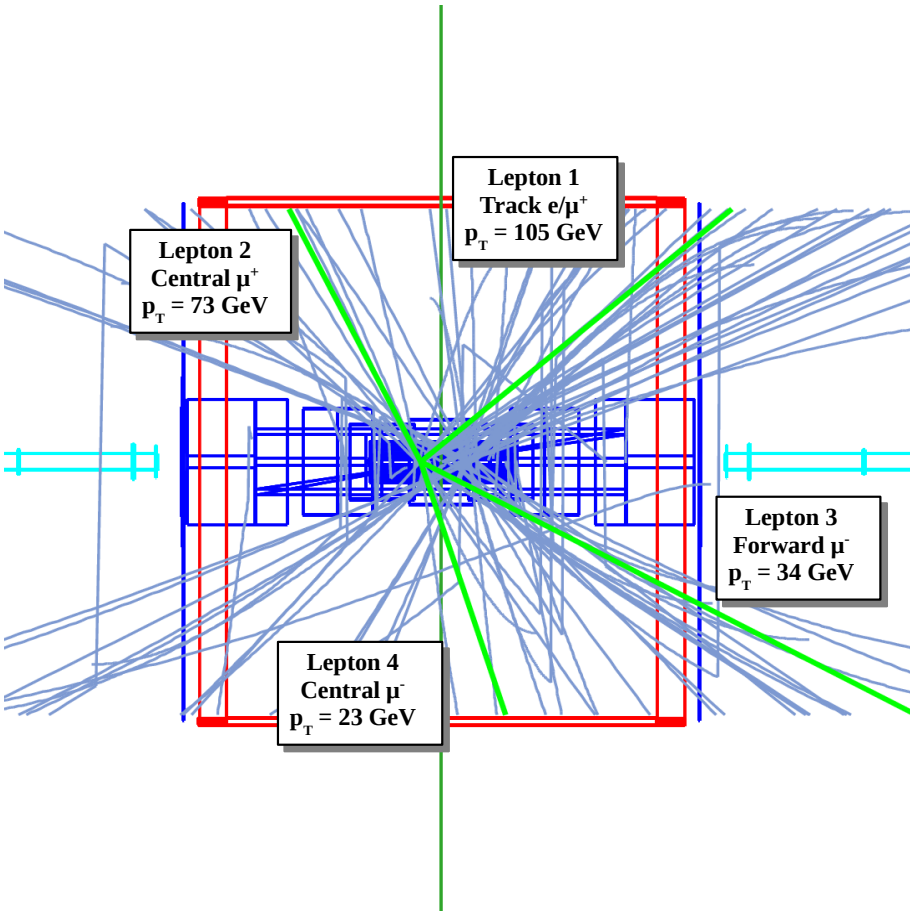

Figure B.2: Side view. Run number: 211311, Event number: 233113.

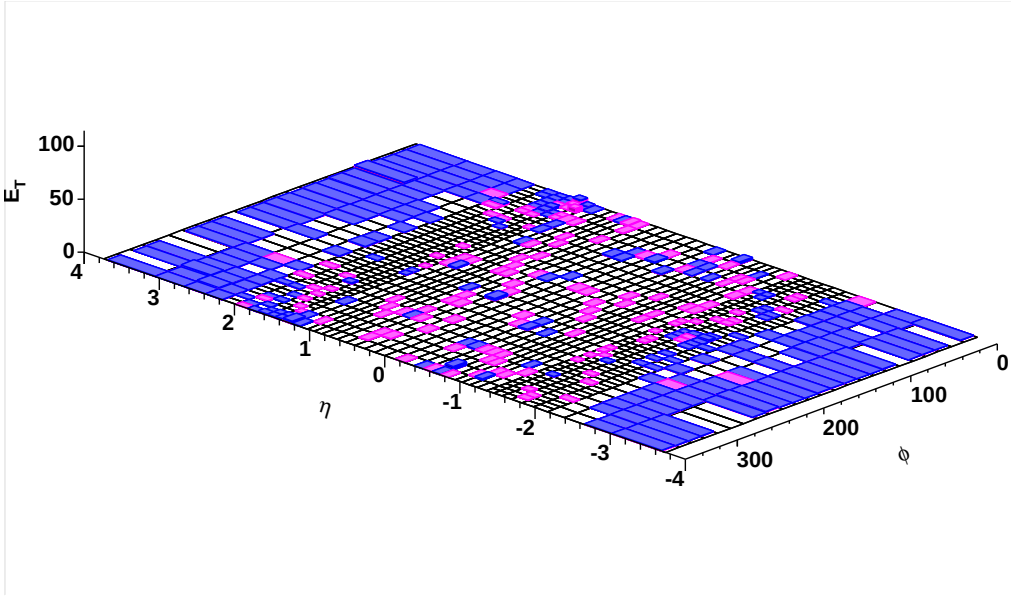

Figure B.3: Lego view. Run number: 211311, Event number: 233113.

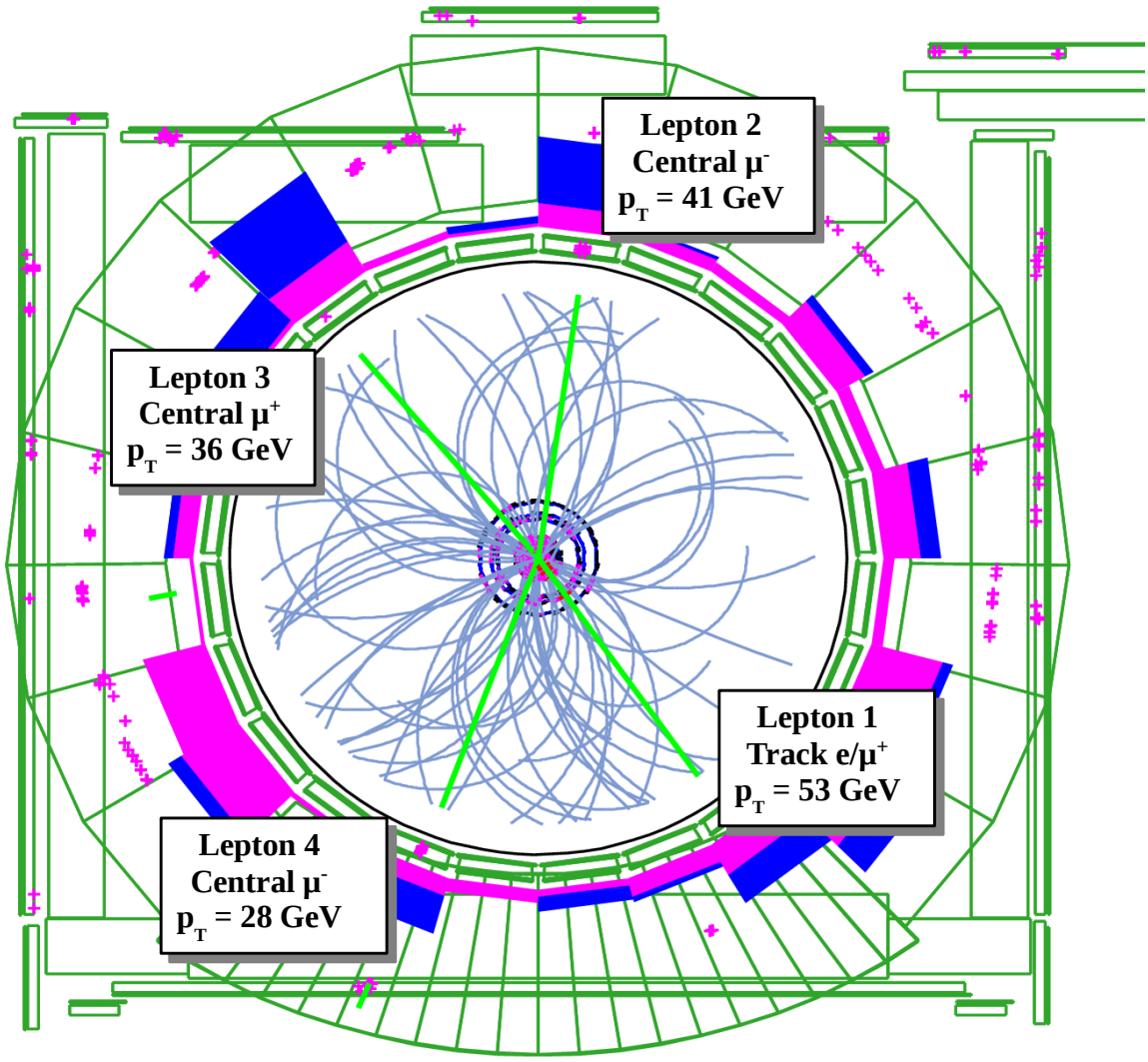

Figure B.4: COT view. Run number: 229084, Event number: 1785583.

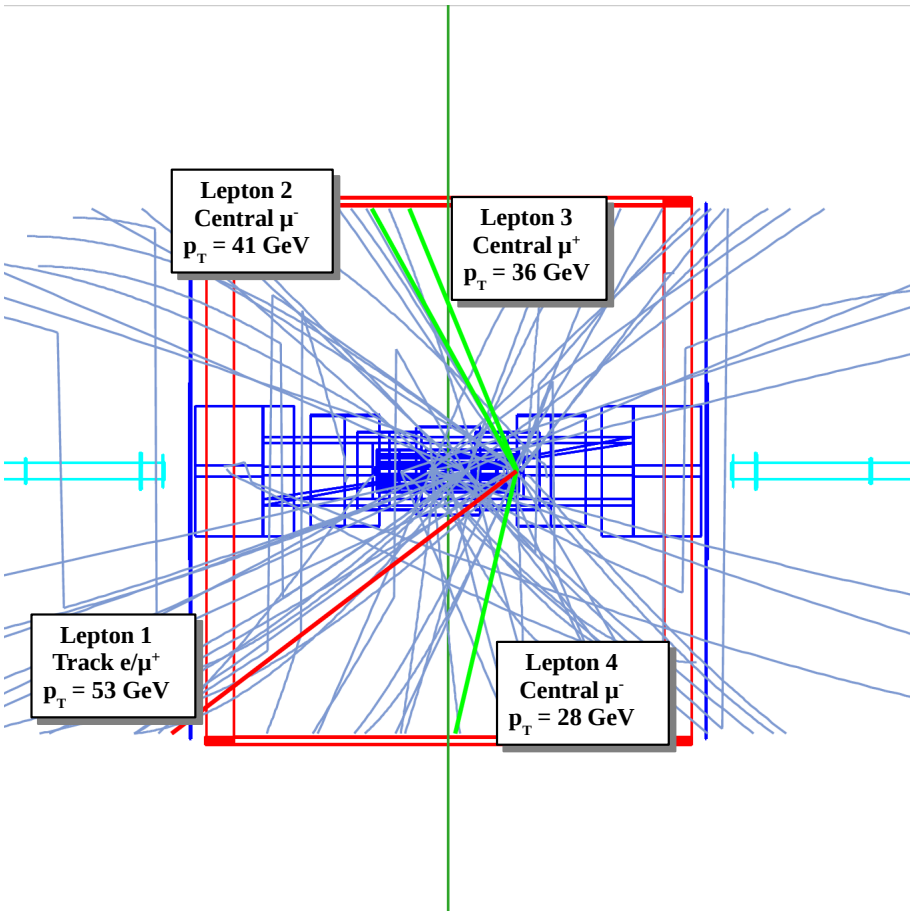

Figure B.5: Side view. Run number: 229084, Event number: 1785583.

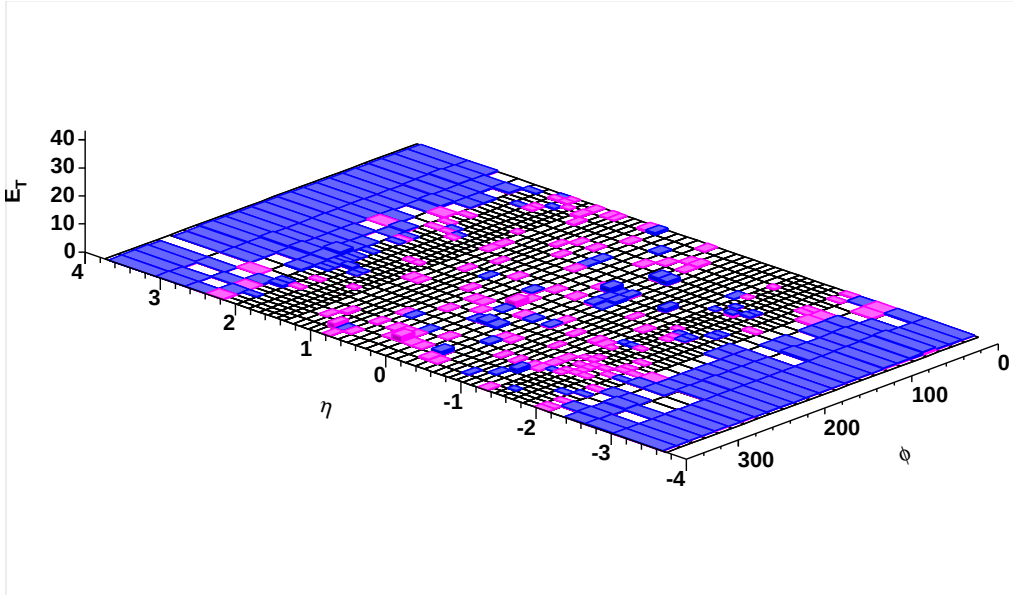

Figure B.6: Lego view. Run number: 229084, Event number: 1785583.

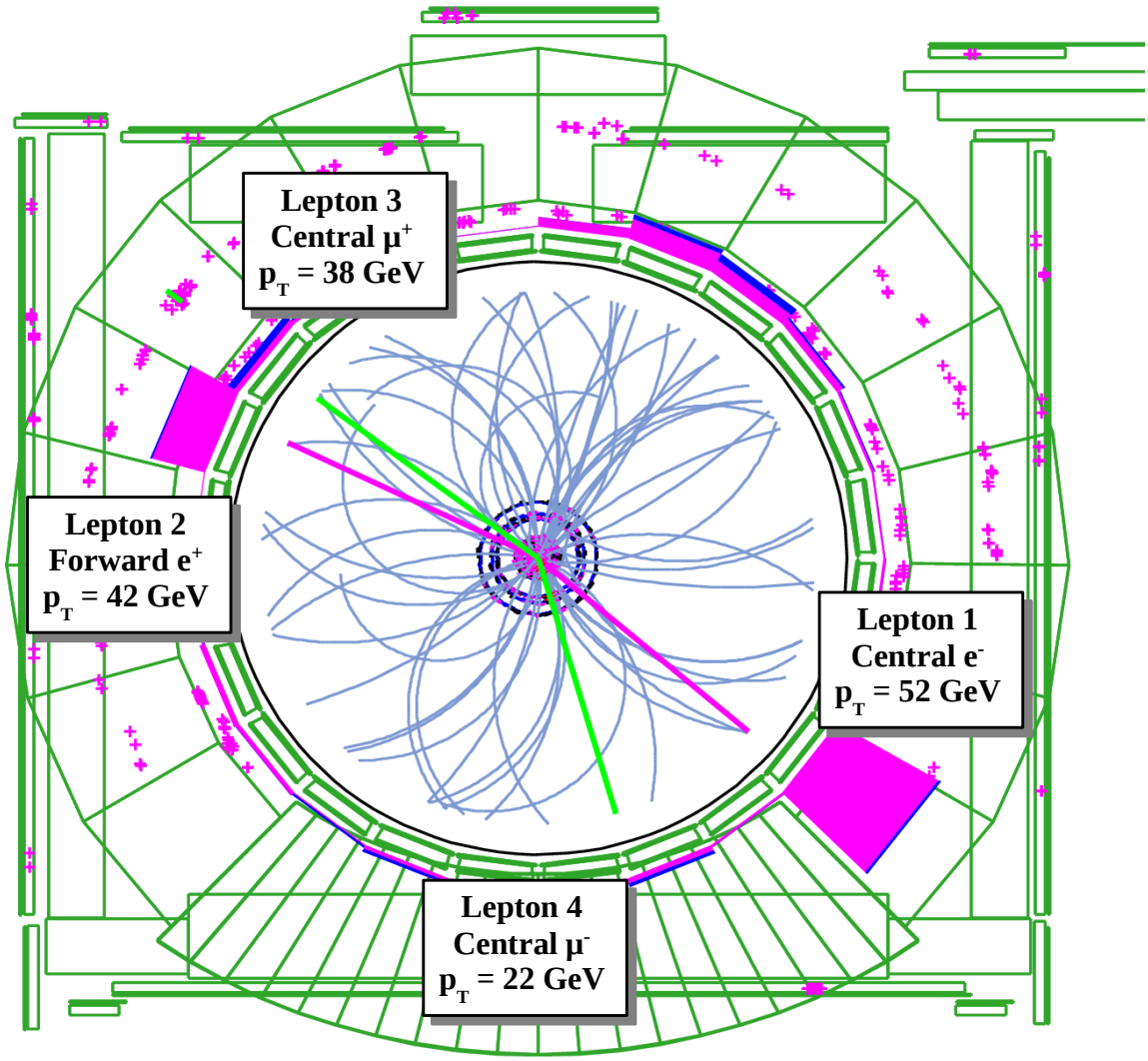

Figure B.7: COT view. Run number: 268560, Event number: 5088.

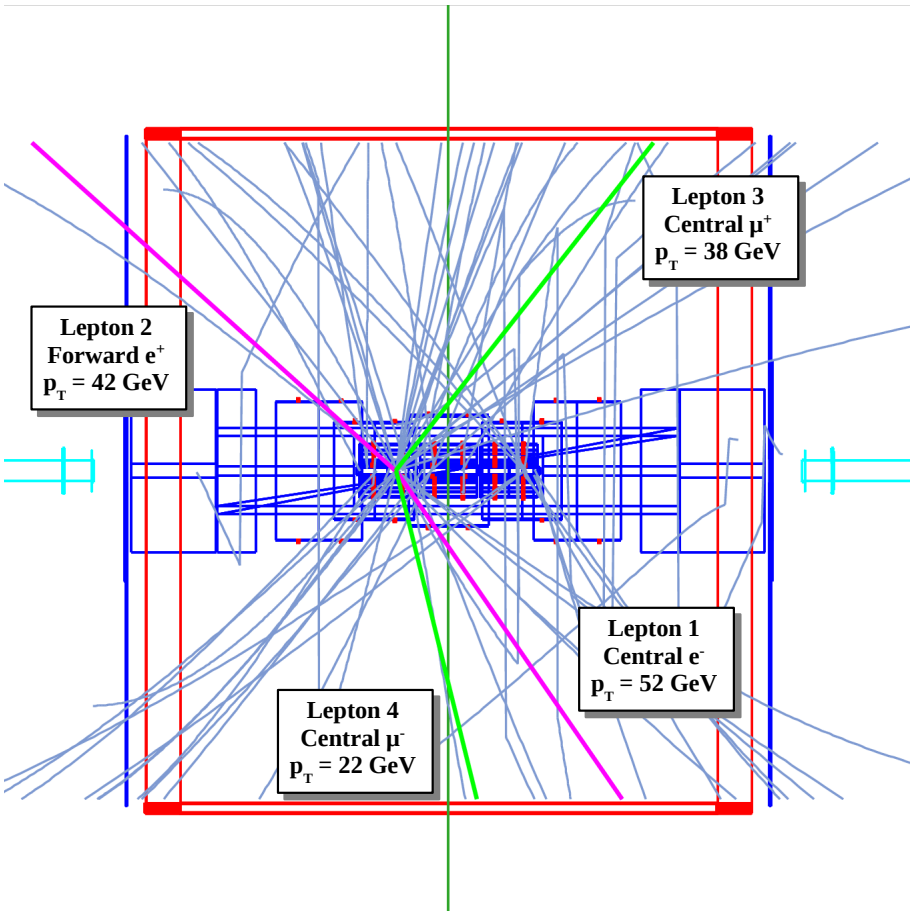

Figure B.8: Side view. Run number: 268560, Event number: 5088.

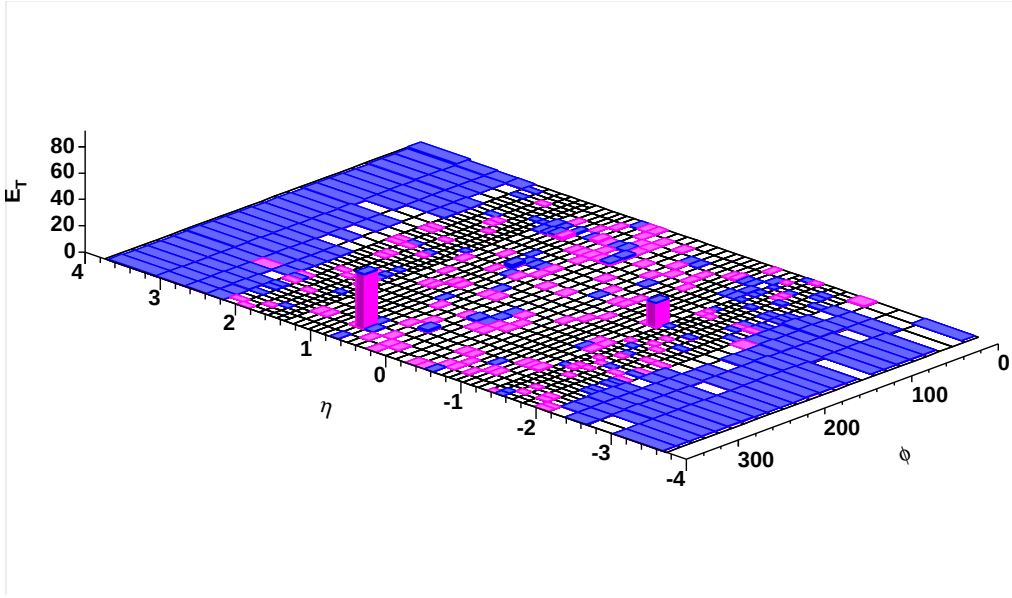

Figure B.9: Lego view. Run number: 268560, Event number: 5088.

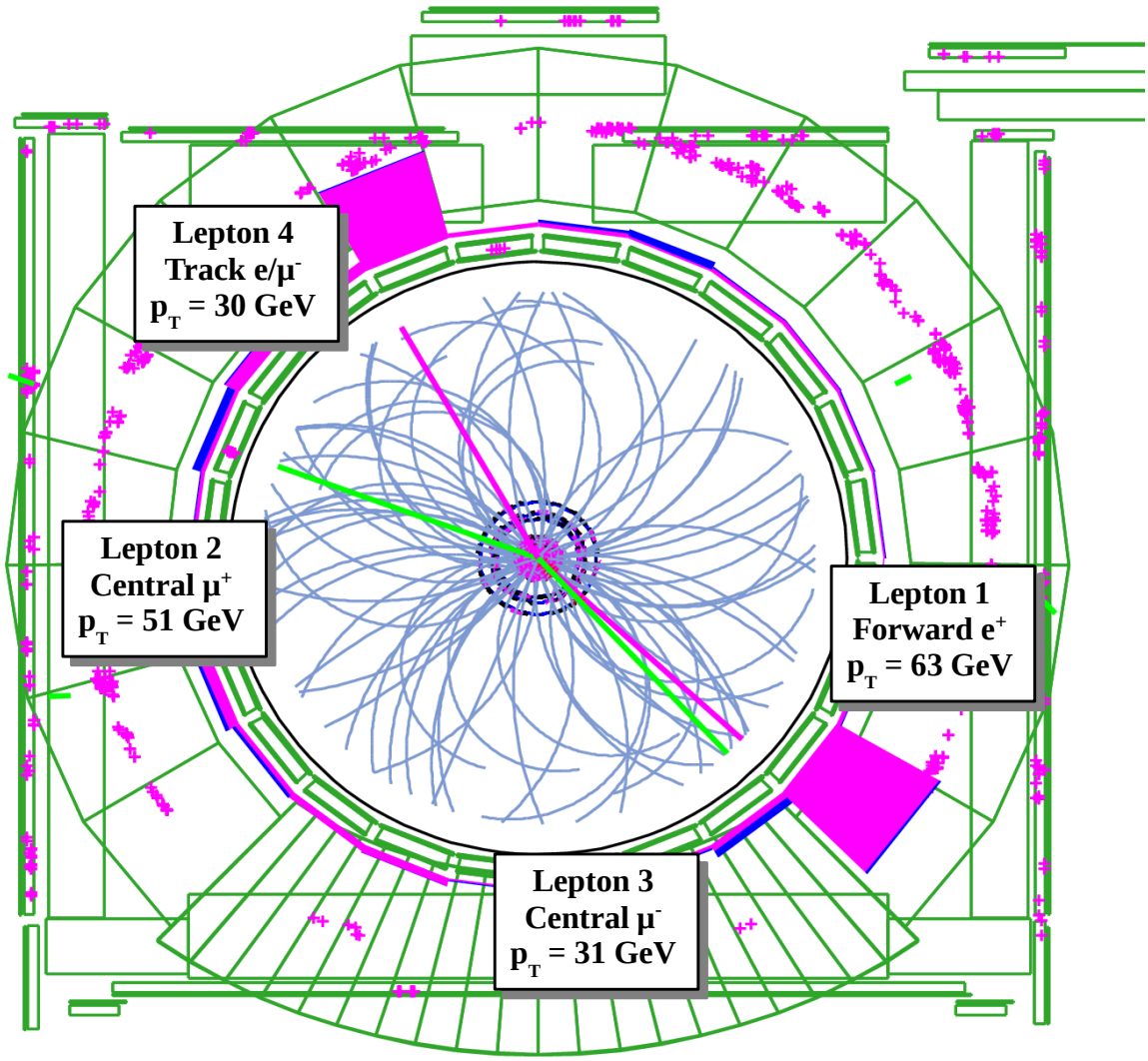

Figure B.10: COT view. Run number: 270465, Event number: 996975.

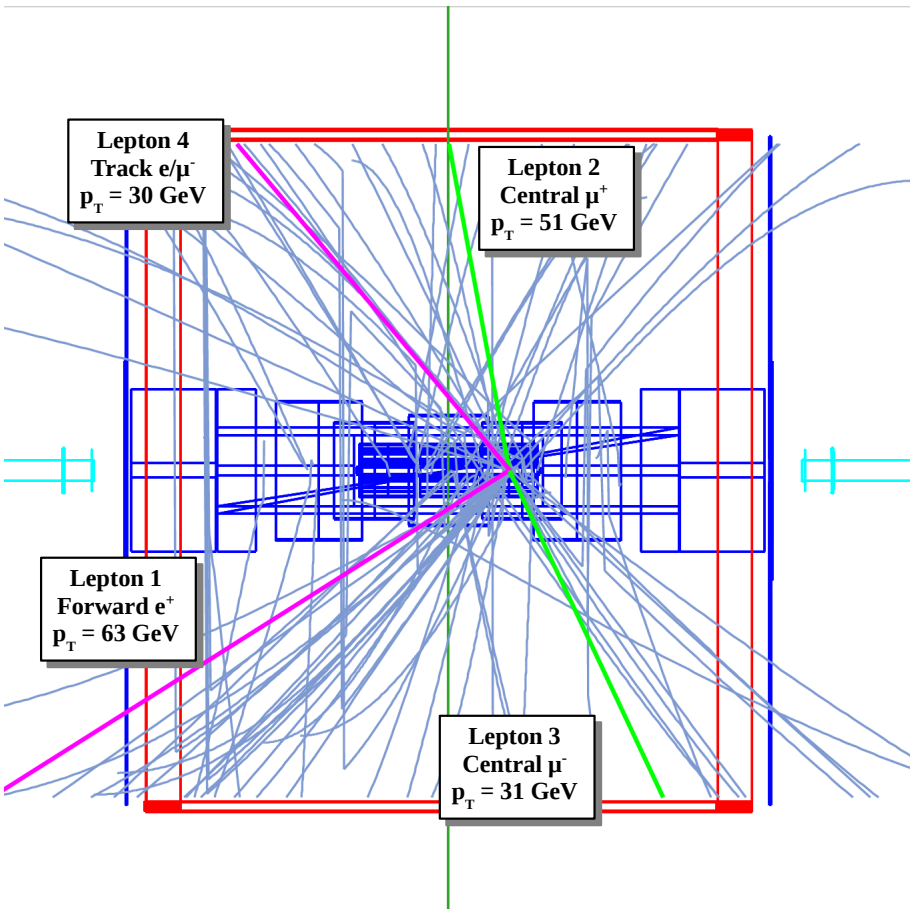

Figure B.11: Side view. Run number: 270465, Event number: 996975.

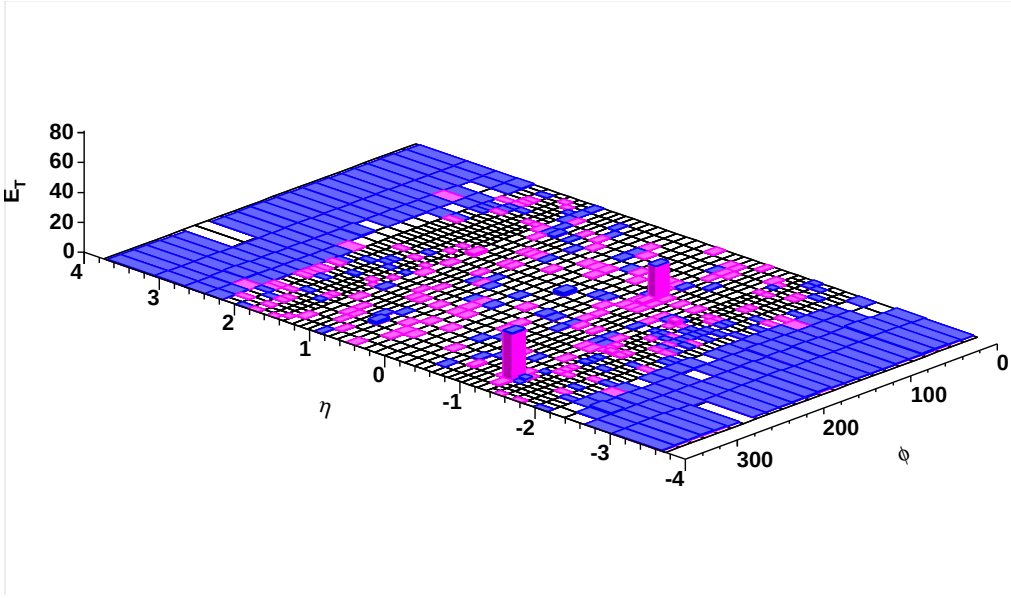

Figure B.12: Lego view. Run number: 270465, Event number: 996975.

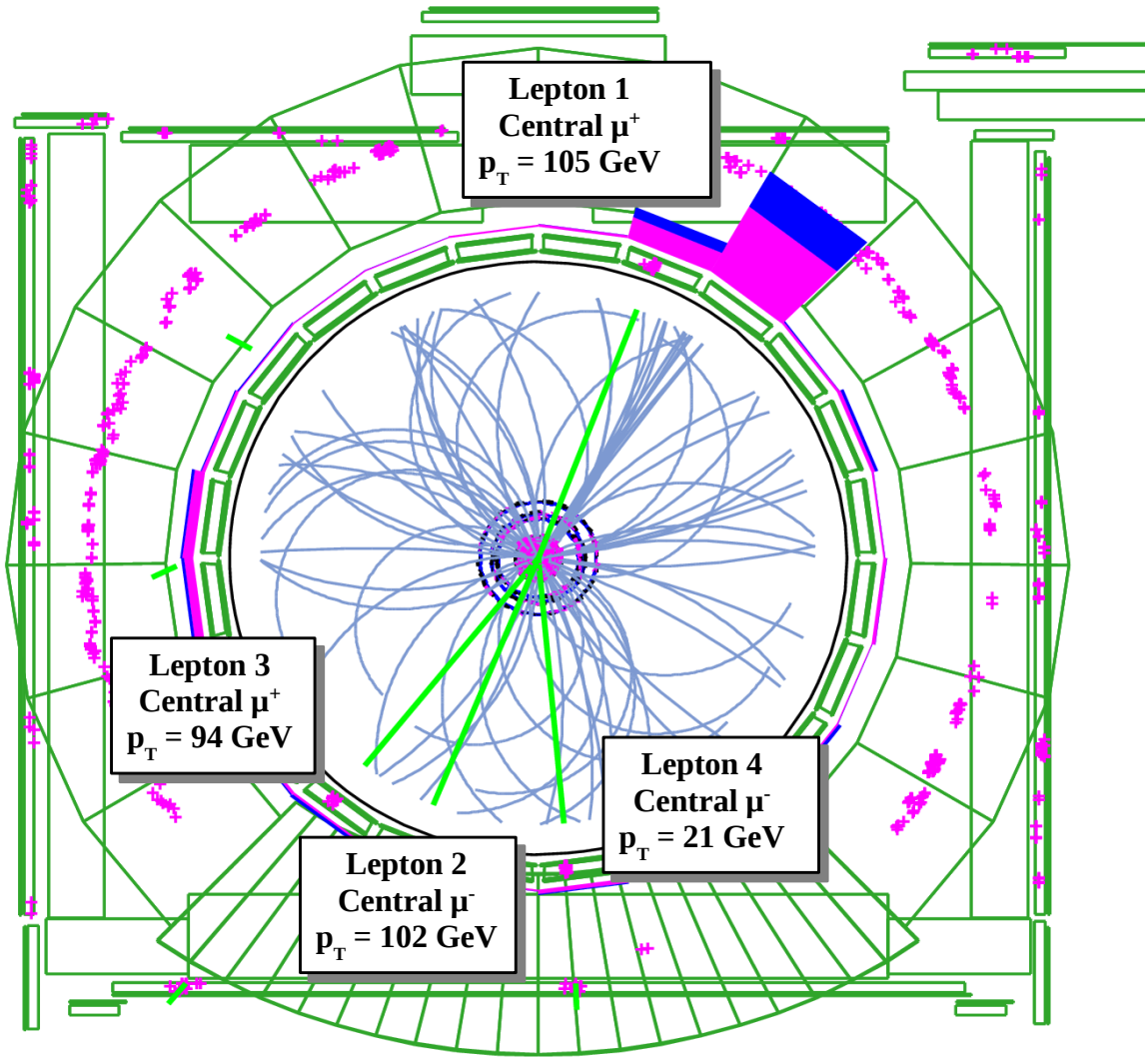

Figure B.13: COT view. Run number: 270624, Event number: 9796697.

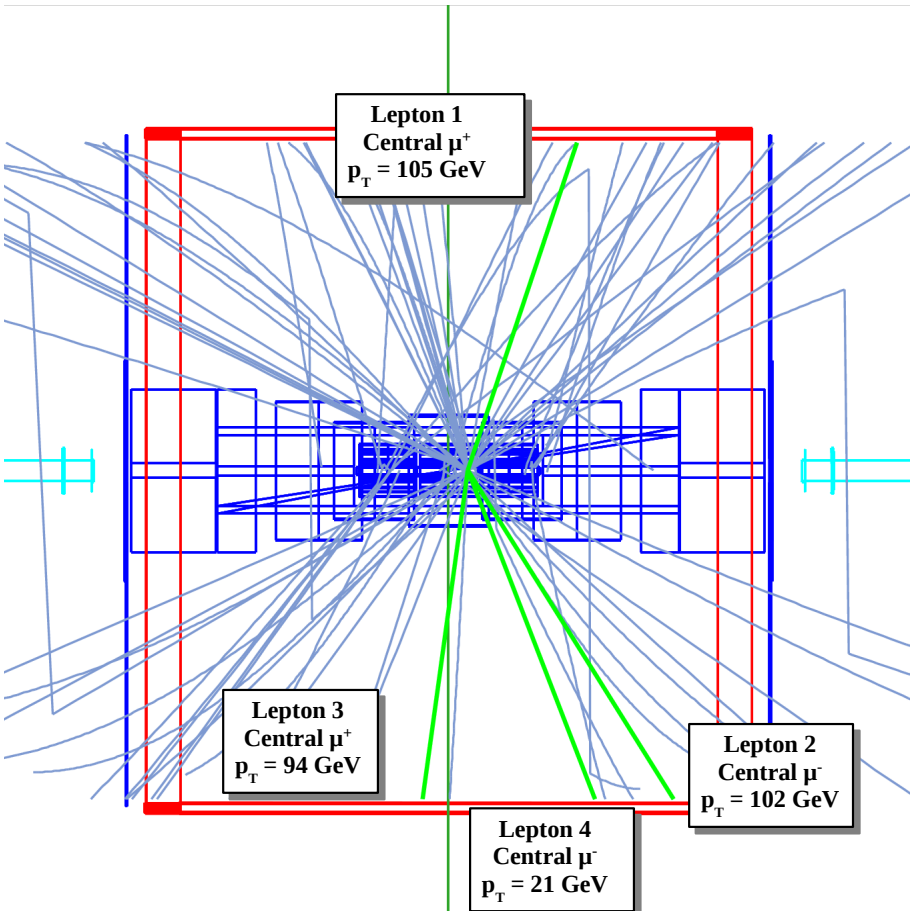

Figure B.14: Side view. Run number: 270624, Event number: 9796697.

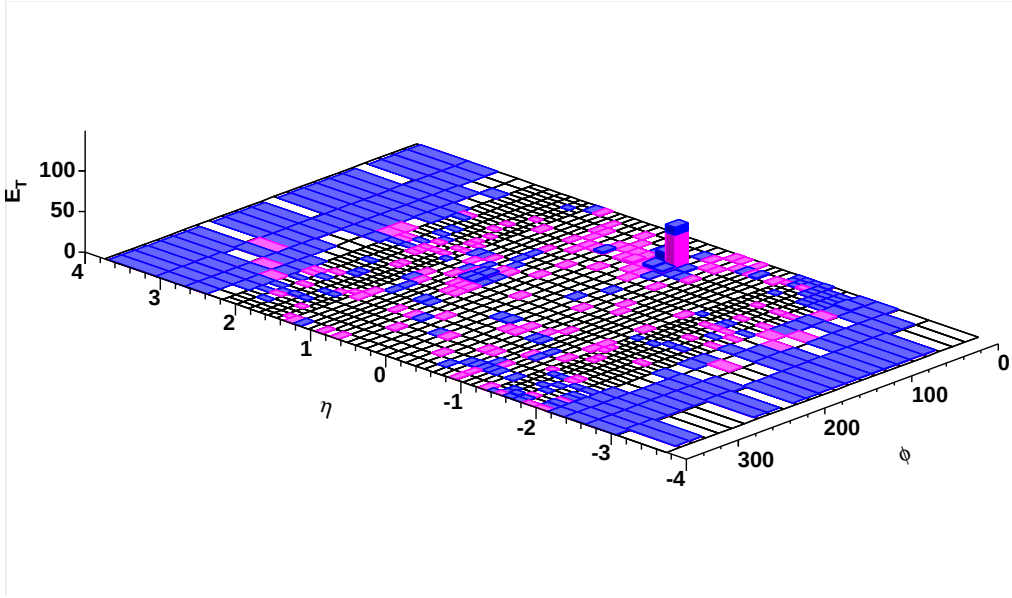

Figure B.15: Lego view. Run number: 270624, Event number: 9796697.

Bibliography

[1] M. Bauce, S. Pagan Griso, D. Lucchesi, D. Benjamin, D.A. Hidas, M. Kruse, E. James, S. Jindariani, B. Rutherford, R. Lysak, A. Robson, R. St. Denis, P. Bussey, M. Herndon, and J. Pursley. Observation of ZZ to four leptons at CDF using 4.8 fb-1 of data, 2009. URL `http://www-cdf.fnal.gov/physics/ewk/2009/ZZllll/ZZWeb/index.html`. CDF/PUB/ELECTROWEAK/PUBLIC/9910.

[2] C. Amsler et al. Review of Particle Physics. *Physics Letters*, B 667:1, 2008.

[3] Y. Fukuda et al. Evidence for oscillation of atmospheric neutrinos. *Physical Review Letters*, 81:1562 – 1567, 1998.

[4] I. J. R. Aitchison and A. J. G. Hey. *Gauge Theories in Particle Physics, 2 Volume Set*. Taylor & Francis, 3 edition, January 2004.

[5] R. Ellis, W.J. Stirling, and B.R. Webber. *QCD and Collider Physics*. Cambridge University Press, 2003.

[6] S. Narison. *QCD as a Theory of Hadrons*. Cambridge University Press, 2007.

[7] Peter W. Higgs. Broken symmetries and the masses of gauge bosons. *Physical Review Letters*, 13(16):508+, October 1964. URL `http://dx.doi.org/10.1103/PhysRevLett.13.508`.

[8] Donald H. Perkins. *Introduction to High Energy Physics*. Cambridge University Press, 2000.

[9] K. Hagiwara, R. D. Peccei, D. Zeppenfeld, and K. Hikasa. Probing the weak boson sector in e+e$\rightarrow W^+W^-$. *Nuclear Physics B*, 282:253 – 307, 1987.

[10] J. Abdallah et al. ZZ production in e^+e^- interactions at $\sqrt{s} = 183$ GeV to 209 GeV. *Eur. Phys. J.*, C30:447–466, 2003.

[11] V. M. Abazov et al. Measurement of the WW Production Cross Section in $p\bar{p}$ Collisions at $\sqrt{s}$=1.96 TeV. *Phys. Rev. Lett.*, 94:151801, 2005.

[12] CDF Collaboration. Measurement of the WW Production Cross Section in $p\bar{p}$ collisions at $\sqrt{s} = 1.96$ TeV using 3.6 fb^{-1} of CDF Run II Data, 2009. CDF/PUB/ELECTROWEAK/PUBLIC/9753.

[13] T. Aaltonen et al. Observation of WZ production. *Phys. Rev. Lett.*, 98:161801, 2007.

[14] V. M. Abazov et al. Measurement of the $p\bar{p} \rightarrow WZ + X$ Cross Section at $\sqrt{s} = 1.96$ TeV and Limits on WWZ Trilinear Gauge Couplings. *Phys. Rev.*, D76:111104, 2007.

[15] T. Aaltonen et al. First Measurement of ZZ Production in $p\overline{p}$ Collisions at $\sqrt{s} = 1.96$-TeV. *Phys. Rev. Lett.*, 100:201801, 2008.

[16] V. M. Abazov et al. $ZZ \to \ell^+\ell^-\nu\bar{\nu}$ production in $p\bar{p}$ collisions at $\sqrt{s} = 1.96$-TeV. *Phys. Rev.*, D78:072002, 2008.

[17] V. M. Abazov et al. Observation of ZZ production in $p\bar{p}$ collisions at $\sqrt{s} = 1.96$-TeV. *Phys. Rev. Lett.*, 101:171803, 2008.

[18] C.-M. Kuo. Diboson Production at the LHC. *Jour. of Phys.*, Conf. Ser. 110:042010, 2008.

[19] V. Brigljević. Measurement of Diboson production with CMS. *ACTA PHYSICA POLONICA B*, 38, 2007.

[20] Ilektra A. Christidi. $ZZ \to 4\ell$ Expected Sensitivity With the First ATLAS Data. Prepared for 28th Physics in Collision (PIC 2008), Perugia, Italy, 25-28 Jun 2008.

[21] R. Blair et al. The CDF-II detector: Technical design report. FERMILAB-PUB-96-390-E.

[22] G. Apollinari, Konstantin Goulianos, P. Melese, and M. Lindgren. Shower maximum detector for the CDF plug upgrade calorimeter. *Nucl. Instrum. Meth.*, A412:515–526, 1998.

[23] J. Marriner. Secondary vertex fit with mass and pointing constrains, 1993. CDF/DOC/SEC_VTX/PUBLIC/1996.

[24] P. Gatti. Performance of the new tracking system at CDF II. FERMILAB-THESIS-2001-23.

[25] C. Hays et al. Inside-Out Tracking at CDF. *Nucl. Instrum. Meth.*, A538:249, 2005.

[26] J. Goldstein, S. Harper, B. Heinemann, G. Manca, and P. Renton. Reconstructing the Plug Electron Energy in 5.3.3, 2005. CDF/DOC/ELECTRON/CDFR/7687.

[27] CDF Collaboration. Measurement of the inclusive W and Z cross section in $p\overline{p}$ collisions at $\sqrt{s} = 1.96$ TeV. *Jour. of Phys.*, G34:2457, 2007.

[28] G.C. Blazey, J.R. Dittmann, S.D. Ellis, V.D. Elvira, K. Frame, S. Grinsten, R. Hirosky, R. Piegaia, H. Shellman, R. Snihur, V. Sorin, and D. Zeppenfeld. Run II Jet Physics, 2000. CDF/PUB/JET/PUBLIC/5293.

[29] F. et al. Abe. Topology of three-jet events in $p\overline{p}$ collision at $\sqrt{s} = 1.8$ TeV. *Phys. Rev.*, D45: 1448, 1992.

[30] J. et al. Adelman. Determination of the Jet Energy Scale at the Collider Detector at Fermilab. *Nucl. Instr. Meth.*, A566:375, 2006.

[31] A. Bhatti et al. Determination of the jet energy energy scale at the Collider Detector at Fermilab. *Nucl. Instrum. Methods Phys. Res.*, A566:375, 2006.

[32] D. Cox. CDF L2 Track Trigger Upgrade, 2008. in *Proc. 19th Hadron Collider Physics Symposium*.

[33] T. Sjostrand, S. Mrenna, and P. Skands. Pythia 6.4 Physics and Manual. *J. High En. Phys.*, 05:026, 2006.

[34] U. Baur and E. L. Berger. Probing the weak-boson sector in $Z\gamma$ production at hadron colliders. *Phys. Rev.*, D47:4889, 1993.

[35] P. Nadolsky et al. Implications of CTEQ global analysis for collider observables. *Phys. Rev.*, D78:013004, 2008.

[36] R. Brun, R. Hagelberg, M. Hansroul, and J. Lassalle. . *CERN-DD-78-2*.

[37] J.M. Campbell and R.K. Ellis. Vector boson pair production at the Tevatron, including all spin correlations of the boson decay products. *Phys. Rev.*, D60:113006, 1999.

[38] D. de Florian and M. Grazzini. Higgs production through gluon fusion: updated cross sections at the Tevatron and the LHC. *Phys. Lett.*, B674:291–294, 2009.